



Delft University of Technology

Document Version

Final published version

Citation (APA)

Araya Day, I. M. (2026). *Revealing topology with flux: Manifestations of broken reciprocity*. [Dissertation (TU Delft), Delft University of Technology]. <https://doi.org/10.4233/uuid:27d65bf2-673b-47af-ba83-b1d96645e775>

Important note

To cite this publication, please use the final published version (if applicable). Please check the document version above.

Copyright

In case the licence states "Dutch Copyright Act (Article 25fa)", this publication was made available Green Open Access via the TU Delft Institutional Repository pursuant to Dutch Copyright Act (Article 25fa, the Taverne amendment). This provision does not affect copyright ownership. Unless copyright is transferred by contract or statute, it remains with the copyright holder.

Sharing and reuse

Other than for strictly personal use, it is not permitted to download, forward or distribute the text or part of it, without the consent of the author(s) and/or copyright holder(s), unless the work is under an open content license such as Creative Commons.

Takedown policy

Please contact us and provide details if you believe this document breaches copyrights. We will remove access to the work immediately and investigate your claim.

This work is downloaded from Delft University of Technology.

> Revealing topology with flux:
Manifestations of broken reciprocity

> Isidora Araya Day

REVEALING TOPOLOGY WITH FLUX
MANIFESTATIONS OF BROKEN RECIPROCITY

REVEALING TOPOLOGY WITH FLUX
MANIFESTATIONS OF BROKEN RECIPROCITY

Dissertation

for the purpose of obtaining the degree of doctor
at Delft University of Technology
by the authority of the Rector Magnificus Prof. dr. ir. H. Bijl,
chair of the Board for Doctorates,
to be defended publicly on Friday 27 February 2026 at 12:30.

by

Isidora Melania ARAYA DAY

This dissertation has been approved by the promotor.

Composition of the doctoral committee:

Rector Magnificus,	Chairperson
Dr. A. R. Akhmerov	Delft University of Technology, promotor
Prof. dr. M. T. Wimmer	Delft University of Technology, promotor

Independent members:

Prof. dr. G.A. Steele	Delft University of Technology
Prof. dr. D.P. DiVincenzo	Delft University of Technology
Prof. dr. S.H. Simon	Oxford University, United Kingdom
Dr. A. Chatterjee	Delft University of Technology
Dr. R. Riwar	Forschungszentrum Jülich, Germany

AI disclosure:

I used AI-based tools ChatGPT and Github Copilot to brainstorm ideas, review the text, write code, and autocomplete.

This work was supported by the Netherlands Organization for Scientific Research (NWO/OCW) as part of the Frontiers of Nanoscience program.



Copyright © 2026 I. Araya Day

Casimir PhD Series, Delft-Leiden 2026-02

CONTENTS

Summary	vii
Samenvatting	ix
1 Introduction	1
1.1 Preface	1
1.2 The scattering formalism	3
1.3 Flux as an analogue of momentum	5
1.4 Flux in superconducting systems	6
1.5 This thesis	8
2 Topological defects in a double-mirror quadrupole insulator displace diverging charge	17
2.1 Introduction	18
2.2 Topological defects in the quadrupole insulator	19
2.3 Divergence of the defect charge.	21
2.4 Conclusion	23
3 Pfaffian invariant identifies magnetic obstructed atomic insulators	27
3.1 Introduction	28
3.2 Pfaffian topological invariant	28
3.3 Model Hamiltonian construction	31
3.4 Confirmation of the invariant	31
3.5 Conclusions.	33
4 Scattering theory of higher order topological phases	37
4.1 Introduction	38
4.2 Why the extrinsic scattering invariant is insufficient	39
4.3 Intrinsic scattering invariant construction	41
4.4 Applications of the intrinsic scattering invariant	46
4.4.1 Intrinsic scattering invariant of BBH model	46
4.4.2 Systems with magnetic rotation symmetry.	48
4.4.3 Axion insulator: 3D inversion	51
4.5 Conclusion and discussion	52
4.6 Scattering equation	54
4.7 Symmetry constraints on scattering matrices	55
4.7.1 Unitary symmetry	56
4.7.2 Antiunitary antisymmetry	56
4.7.3 Unitary antisymmetry	57
4.7.4 Antiunitary symmetry	58

4.8	Factoring out commuting symmetries	59
4.9	Implementation of a smooth gauge choice for V and Q	59
5	Identifying biases of the Majorana scattering invariant	65
5.1	Introduction	66
5.2	Scattering invariant in the strongly coupled limit	66
5.3	Scattering invariant in the tunneling limit	69
5.3.1	Strong Majorana overlap	69
5.3.2	Quasi-Majorana strong overlap	70
5.3.3	Quasiparticle sinks.	71
5.4	Discussion	72
5.5	Details of the tight-binding model	73
6	Chiral adiabatic transmission protected by Fermi surface topology	77
6.1	Introduction	78
6.2	Perturbative analysis in a Josephson junction	78
6.3	Chiral adiabatic transmission in a trijunction	82
6.4	Discussion and conclusions.	85
6.5	Appendix	86
7	Pymablock: an algorithm and a package for quasi-degenerate perturbation theory	91
7.1	Introduction	92
7.2	Constructing an effective model	93
7.2.1	k - p model of bilayer graphene	94
7.2.2	Dispersive shift of a transmon qubit coupled to a resonator	96
7.2.3	Induced gap in a double quantum dot	97
7.2.4	Selective diagonalization.	99
7.3	Perturbative block-diagonalization algorithm.	100
7.3.1	Problem statement.	100
7.3.2	Existing solutions	102
7.3.3	Pymablock's algorithm.	104
7.3.4	Equivalence to Schrieffer–Wolff transformation	107
7.3.5	Extra optimization: common subexpression elimination	107
7.4	Implementation	108
7.4.1	The data structure for block operator series	108
7.4.2	The implicit method for large sparse Hamiltonians	109
7.4.3	Code generation	110
7.5	Benchmark	111
7.6	Conclusion	113
8	Conclusion	121
	Acknowledgements	123
	Curriculum Vitae	125
	List of Publications	127

SUMMARY

A magnetic field forces electrons to twist as they transport around it, revealing properties of the medium. This observation—the Aharonov-Bohm effect—applies to any quantum system where charged particles remain coherent, like an electron in a sufficiently clean solid state device. This thesis is about using this effect to probe and design topologically protected electronic phenomena.

The first part of this thesis focuses on crystalline topological insulators, phases protected by spatial symmetries of a crystal. Chapters 2 and 3 concern the bulk and boundary response of obstructed atomic insulators, phases that lack a bulk-boundary correspondence and that we characterize using a topological defect and momentum-space invariants respectively. Chapter 4 is about intrinsic higher-order topological insulators, phases that do have a bulk-boundary correspondence and therefore are detectable in transport experiments. We develop a theory based on electronic transport and the insertion of fluxes to capture topology, and show that it may be used to understand how disorder affects these phases. In Chapter 5, we apply this theory to an experimentally-relevant proposal of topological superconductivity and identify its biases.

Differently from the first part, the rest contains two projects that originated from numerical adventures. Chapter 6 proposes a superconducting chiral waveguide that relies on magnetic flux to achieve unidirectional transport of electron-hole pairs. The final chapter, while unrelated to flux, topology, or transport, introduces an algorithm that may be used in the study of these phenomena. Chapter 7 is about Pymablock, an open-source Python package to efficiently perform quasi-degenerate perturbation theory. The cover highlights the relevance of computational approaches in modern condensed matter physics, and also in this work.

SAMENVATTING

Een magnetisch veld dwingt elektronen te draaien terwijl ze eromheen bewegen, waardoor eigenschappen van het medium aan het licht komen. Deze waarneming—het Aharonov-Bohm-effect—is van toepassing op elk kwantumsysteem waarin geladen deeltjes coherent blijven, zoals een elektron in een voldoende zuiver halfgeleiderapparaat. Deze dissertatie gaat over het gebruik van dit effect om topologisch beschermde elektronische fenomenen te onderzoeken en te ontwerpen.

Het eerste deel van deze dissertatie richt zich op kristallijne topologische isolatoren, fasen die beschermd worden door de *spatial symmetries* van een kristal. De hoofdstukken 2 en 3 behandelen de bulk en boundary van *obstructed atomic insulators*, fasen die geen *bulk-boundary correspondence* hebben en die we karakteriseren met respectievelijk een topologisch defect en impulsruimte-invarianten. Hoofdstuk 4 gaat over *intrinsic higher-order topological insulators*, fasen die wel een *bulk-boundary correspondence* hebben en daarom detecteerbaar zijn in transportexperimenten. We ontwikkelen een theorie gebaseerd op elektronisch transport en de invoeging van fluxen om topologie te beschrijven, en laten zien dat deze gebruikt kan worden om te begrijpen hoe ruis deze fasen beïnvloedt. In hoofdstuk 5 passen we deze theorie toe op een experimenteel relevant voorstel voor topologische supergeleiding en identificeren we de vertekeningen ervan.

In tegenstelling tot het eerste deel bevat de rest twee projecten die voortkomen uit numerieke avonturen. Hoofdstuk 6 beschrijft een supergeleidende chirale golfgeleider die gebruikmaakt van magnetische flux om unidirectioneel transport van elektron-gatparen te realiseren. Het laatste hoofdstuk, hoewel niet gerelateerd aan flux, topologie of transport, introduceert een algoritme dat gebruikt kan worden bij de studie van deze fenomenen. Hoofdstuk 7 gaat over Pymablock, een open-source Python code voor het efficiënt uitvoeren van quasi-gedegenereerde perturbatietheorie. De omslag benadrukt het belang van computationele methodes in de moderne vastestoffysica, en ook in dit werk.

1

INTRODUCTION

We shall show that, contrary to the conclusions of classical mechanics, there exist effects of potentials on charged particles, even in the region where all the fields vanish.

Y. Aharonov and D. Bohm, 1959

1.1. PREFACE

In classical physics, charged particles respond only to electric and magnetic fields that directly cross their path. Scalar and vector potentials serve as mathematical tools for calculating the fields; potentials only appear in Maxwell equations through their gradients. Quantum mechanics works differently: potentials enter Schrödinger's equation directly through the Hamiltonian, and therefore they couple to the wavefunctions even if the fields they generate are zero. While scalar potentials contribute to the energy associated with a state, vector potentials couple to the momentum of charged particles and therefore contribute to the global phase of the wavefunction.

A striking consequence of this difference is the Aharonov-Bohm effect¹ [1, 2, 3, 4], where the phase that a charged particle acquires as it travels around a magnetic flux results in a periodic interference pattern in the recombined wavefunction. Figure 1.1(left) illustrates it: two electron beams that travel around a solenoid threaded by a magnetic flux Φ acquire opposite phase shifts $e^{i\frac{q}{\hbar}\int dr\cdot A} = e^{\pm i\frac{q\Phi}{2\hbar}}$. The sign of the phase shift depends on the direction of the path the electron takes around the vector potential $A(\Phi)$ of the solenoid. The interference pattern is then periodic in Φ , even though the electrons do not directly cross the magnetic field lines, a topological effect that remains robust to changes in the solenoid geometry or the precise path taken by the electrons. In electronic transport, the Aharonov-Bohm effect manifests as a periodic modulation of the conductance across a metallic ring threaded by a flux [5, 6], even though a mesoscopic ring hosts a finite number of modes instead of a single electron (Fig. 1.1(right)).

¹While the effect was first discovered by W. Ehrenberg and R. E. Siday around ten years earlier than Y. Aharonov and D. Bohm, the latter reflected on and brought attention to the role of potentials in quantum mechanics.

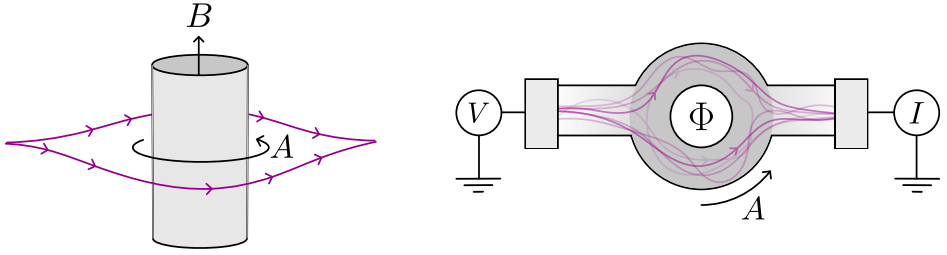


Figure 1.1: (a) Aharonov-Bohm effect thought experiment. An electron beam (purple) splits into two paths that travel around a solenoid threaded by a magnetic flux Φ . The two beams recombine and interfere. (b) Transport of electrons through metallic ring threaded by a magnetic flux Φ .

Identifying topological phenomena in mesoscopic systems is crucial to understanding their universal properties, where individual characteristics of a sample do not affect macroscopic observables. The quantization of the Hall conductivity $\sigma_{xy} = I/V_H$ as a function of magnetic field in two-dimensional electron gases (2DEGs) is a prime example of such a phenomenon. Figure 1.2(left) shows a minimal Hall bar setup that probes the quantum Hall effect, which we understand using different approaches. On the one hand, linear response theory [7] applied to non-interacting electrons predicts that the Hall conductivity $\sigma_{xy} = \frac{e^2}{h} C$, where C is the number of protected modes that propagate along the sample edges. This result relies on the periodicity of the Bloch wavefunctions because C —the Chern number—is an integral over the Brillouin zone:

$$C = \frac{1}{2\pi} \int_{\text{BZ}} d\mathbf{k}^2 \text{tr} \nabla \times \mathcal{A}(\mathbf{k}) \in \mathbb{Z}, \quad (1.1)$$

where $\mathcal{A}_{mn}(\mathbf{k}) = i \langle m\mathbf{k} | \partial_{\mathbf{k}} | n\mathbf{k} \rangle$ is the non-Abelian Berry connection of the states below the Fermi level labeled by m and n . The Hall conductivity is then defined as a bulk property, highlighting the bulk-boundary correspondence of the quantum Hall effect. On the other hand, instead of considering a Hall bar geometry, Laughlin [8] wrapped the two-dimensional electron gas Hall bar into a Corbino disk and threaded a flux through its center, as shown in Fig. 1.2(right). Remarkably, adiabatically increasing $\Phi(t)$ by a quantum of flux results in a quantized charge eC pumped from the inner edge of the disk to the outer edge, despite the gapped nature of the sample. This result is agnostic to the details of the Bloch wavefunctions and it extends beyond single particle systems [9, 10].

Since the discovery of these two effects, a vast number of topological phases have been proposed, with crystalline symmetries and superconductivity playing a central role. The effects of flux insertion are, however, not limited to the quantum Hall effect and the Aharonov-Bohm effect: quantum spin Hall insulators [11], for example, pump spin [12], while topological superconductors pump fermion parity [13, 14]. Identifying these phenomena has been crucial to the understanding of topological phases and their design in mesoscopic systems. In this thesis we ask the questions: *do crystalline topological phases also respond to flux insertion? Does flux reveal any other topological phenomena in mesoscopic systems?* We approach these questions by exploiting the interferometric effect of flux on the wavefunctions, which is captured by electrical quantum transport.

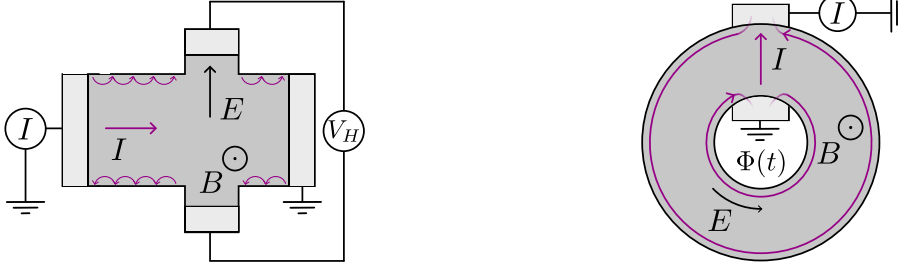


Figure 1.2: Quantum Hall effect and Laughlin's adiabatic charge pumping. (a) Hall bar setup of a 2DEG subject to a magnetic field B . The Hall Voltage V_H is measured across the sample. (b) Corbino disk geometry of the 2DEG with an additional magnetic flux $\Phi(t)$ adiabatically increasing over time. The current $I(t)$ is measured at the outer edge of the disk.

1.2. THE SCATTERING FORMALISM

Mesoscopic systems are small enough to require a quantum mechanical description, and yet large enough to accommodate millions of degrees of freedom. Even in clean and disorder-free samples, electrons behave like waves that scatter as they travel through the uneven potential landscape defined by the sample geometry and its components. Not all electrons, however, contribute to the transport properties of the sample: only those near the Fermi level are relevant. Occupied states far below the Fermi level always come in pairs of opposite velocities, and therefore do not contribute to the current. Despite the complex behavior of the wavefunctions, the Aharonov-Bohm effect manifests in a metallic ring as if it had independent electrons traveling coherently, all acquiring the same phase shift as they transmit through a same arm of the ring.

The scattering formalism is a powerful approach to describe electronic transport: it focuses only on the wavefunctions of the electrons at the Fermi level and describes the phase shifts they acquire as they scatter through the sample. Yet, it provides macroscopic observables such as current and conductance, which emerge from the interference of the wavefunctions. Electrons are injected into the sample from metallic contacts, which are modeled as semi-infinite leads that support a finite number of incoming and outgoing planar modes. The sample is then the only region where the modes scatter, as shown in Fig. 1.3(left). The scattering matrix S relates the amplitudes of the incoming and outgoing modes in the leads [15]:

$$\alpha^{\text{out}} = S\alpha^{\text{in}}, \quad (1.2)$$

where α^{in} and α^{out} are vectors with the modes amplitudes. Because in Hermitian systems current is conserved, the scattering matrix is unitary, $S^\dagger S = SS^\dagger = 1$. In a two-terminal setup, the scattering matrix is a 2×2 block matrix:

$$S = \begin{pmatrix} r_L & t_{LR} \\ t_{RL} & r_R \end{pmatrix}, \quad (1.3)$$

where r_L and r_R are the matrices with reflection coefficients of the left and right leads, respectively, and t_{LR} and t_{RL} are the matrices with transmission coefficients from the right lead to the left lead and vice versa.

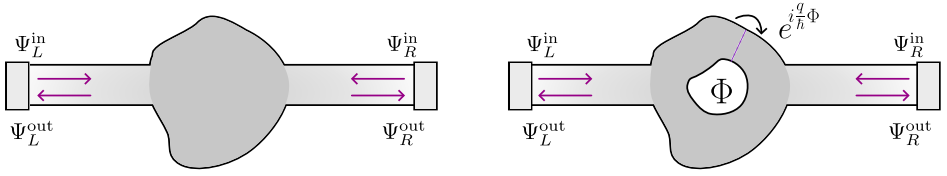


Figure 1.3: A scattering region attached to two semi-infinite leads. Each lead supports a finite number of incoming and outgoing modes that may reflect or transmit. Threading a magnetic flux Φ modifies the hopping terms across a cut by a phase factor $e^{i\frac{q}{h}\Phi}$ (right panel).

A common approach to compute the scattering matrix is to numerically solve the scattering equations at a given energy E :

$$(H - E)(\Psi^{\text{in}}\alpha^{\text{in}} + \Psi^{\text{out}}S(E)\alpha^{\text{in}} + \Psi^{\text{localized}}\alpha^{\text{in}}) = 0, \quad (1.4)$$

where H is the Hamiltonian of the scattering region and semi-infinite leads, and Ψ^{in} , Ψ^{out} , and $\Psi^{\text{localized}}$ are the wavefunctions of the incoming, outgoing, and localized states, respectively. The Kwant Python package for numerical quantum transport simulations [16] takes advantage of the sparsity of tight-binding Hamiltonians to solve Eq. (1.4) efficiently. Alternatively, the Mahaux-Weidenmüller formula [17] provides the scattering matrix in the weak coupling limit:

$$S(E) = 1 - 2\pi i W (E - H + i\pi W^\dagger W)^{-1} W^\dagger, \quad (1.5)$$

where H is the effective Hamiltonian of the scattering region and W is a rectangular matrix with the coupling between the lead's modes and the localized states of H . Both Eq. (1.4) and Eq. (1.5) are useful to express how the scattering matrix transforms under symmetries of the Hamiltonian. Additionally, because in the Mahaux-Weidenmüller formula H and W may only contain degrees of freedom relevant to scattering processes at the Fermi level E , Eq. (1.5) is especially useful to compute an approximation of the scattering matrix analytically.

The scattering formalism unifies the Aharonov-Bohm effect and the quantum Hall effect. On the one hand, the zero-temperature differential conductance is given by the Landauer-Büttiker formula [18, 19, 20]:

$$G = \frac{dI}{dV} \Big|_{V \rightarrow 0} = \frac{2e^2}{h} \text{tr } t^\dagger t, \quad (1.6)$$

where the factor of 2 accounts for spin degeneracy, and I and V are DC current and voltage, respectively. Already in this form, the Landauer-Büttiker formula reveals the Aharonov-Bohm effect: conductance acquires the same periodicity as the scattering matrix. Because threading a magnetic flux is equivalent to inserting a phase factor $e^{i\frac{q}{h}\Phi}$ in the hopping terms of the Hamiltonian across a cut, as shown in Fig. 1.3(right), the Hamiltonian and the scattering matrix become periodic in flux. On the other hand, the charge pumped over an adiabatic cycle of an AC potential $V(\tau)$ is given by the Brouwer formula [21]:

$$Q = \frac{e}{2\pi i} \oint d\tau \text{tr} \left(\frac{dr}{d\tau} r^{-1} \right), \quad (1.7)$$

where $r(\tau)$ is the reflection matrix as a function of the adiabatic parameter τ . In general, Q is not quantized because modes may transmit through the sample, but it becomes quantized in the thermodynamic limit of a gapped system. Applied to Laughlin's Corbino disk, Eq. (1.7) recovers the quantized charge eC pumped from the inner edge to the outer surface. This time, however, the Chern number emerges as a Fermi level property encoded in the geometrical properties of the reflection matrix over the adiabatic cycle of τ , differently from Eq. (1.1).

1.3. FLUX AS AN ANALOGUE OF MOMENTUM

Inserting the phase factor $e^{i\frac{q}{\hbar}\Phi}$ in the hoppings across a single cut is only a gauge choice: distributing the flux over a set of cuts is allowed by the gauge invariance of Schrödinger's equation. The only constraint is that the hoppings around any closed path acquire a phase factor proportional to the flux through the path:

$$\oint d\mathbf{r}' \cdot \mathbf{A}(\mathbf{r}') = \Phi, \quad (1.8)$$

where $\mathbf{A}(\mathbf{r})$ is the vector potential. The gauge in which the flux enters the Hamiltonian through a single cut is, however, equivalent to how momentum enters the Hamiltonian in translational invariant systems. In the latter, Bloch theorem states that the hoppings that wrap around a unit cell acquire a phase factor $e^{i\mathbf{k}\cdot\mathbf{R}}$, where \mathbf{k} is the crystal momentum and \mathbf{R} is a lattice vector of the crystal. Mesoscopic samples are made of several unit cells, making flux an analogue to a supercell momentum parameter. In a Hamiltonian, both quantities transform equivalently under time-reversal symmetry \mathcal{T} :

$$\mathcal{T}^{-1}H(\mathbf{k}, \phi)\mathcal{T} = H(-\mathbf{k}, -\phi). \quad (1.9)$$

Because introducing a flux requires a magnetic field, finite $\phi \neq 0, \pi$ breaks time-reversal symmetry just as finite momentum.

The analogy between flux and momentum is at the core of the generalization of Laughlin's argument to all symmetry classes in the Altland-Zirnbauer classification: the scattering theory of topological insulators and superconductors [22, 23]. The working principle of this theory is to constrain the scattering matrix $S(\mathbf{k}, \phi)$ by the symmetries of the Hamiltonian using Eq. (1.4), and obtain the topological invariant as a function of the reflection matrix $r(\mathbf{k}, \phi)$. To achieve this, we require a sample geometry with leads attached to opposite surfaces, a setup analogue to that of adiabatic charge pumping in the quantum Hall effect. Because attaching leads breaks translational invariance along at least one direction, the scattering invariant of a d -dimensional Hamiltonian is expressed in terms of a $d-1$ -dimensional scattering matrix. For example in class A, computing the Chern number requires a Corbino disk geometry with leads attached to opposite surfaces of the sample:

$$C = \frac{1}{2\pi i} \int_0^{2\pi} d\phi \frac{d}{d\phi} \log \det r(\phi). \quad (1.10)$$

This is equivalent to Eq. (1.7) considering that the reflection matrix $r(\phi) = r^\dagger(\phi)$ is unitary in gapped and sufficiently large systems. In general, because geometric integrals of the unitary reflection matrix are guaranteed to be integers and $r(\mathbf{k}, \phi)$ is smooth in \mathbf{k}

and ϕ , changing a scattering invariant requires finite transmission through the sample. Therefore, scattering invariants may only change when the sample undergoes a delocalization transition, making them a useful tool to study topological phases in the presence of disorder.

In the last few years, a wide variety of topological phases protected by spatial symmetries have been proposed, such as higher-order topological insulators (HOTIs) [24, 25]. These phases are characterized by the existence of protected boundary states of lower dimension than standard topological insulators, such as corner states in two-dimensional HOTIs or hinge states in three-dimensional HOTIs. Topological defects in HOTIs, such as disclinations and dislocations, have been proposed to host fractionally quantized charges [26, 27, 28, 29, 30, 31, 32, 33], manifesting their bulk-boundary correspondence. Because the wavefunctions that surround these defects acquire a phase factor compared to those that do not, this observation hints at a topological response to flux insertion. *How does the scattering theory of topological invariants generalize to crystalline topological phases?* is one of the open questions we address in this thesis.

1.4. FLUX IN SUPERCONDUCTING SYSTEMS

Superconductors, unlike metals, are characterized by the collective behavior of pairs of electrons—Cooper pairs. This provides them with a particle-hole symmetry \mathcal{P} that maps the wavefunctions of electrons to those of holes in addition to complex conjugating the Hamiltonian. As a consequence, the Hamiltonian transforms differently for momenta and flux:

$$\mathcal{P}^{-1}H(\mathbf{k}, \phi)\mathcal{P} = -H(-\mathbf{k}, \phi), \quad (1.11)$$

breaking the analogy between both quantities. An important consequence of this is that threading a magnetic flux Φ through a superconducting ring can no longer be described by a phase factor in the hopping terms of the Hamiltonian. Instead, flux enters everywhere in the sample by making the order parameter wind around the ring, introducing a vortex. Therefore, to ensure the continuity of the order parameter, flux in superconductors may only be inserted in discrete amounts, see Fig. 1.4(a).

One way to lift this restriction is to introduce a weak link in the superconducting ring, as shown in Fig. 1.4(b). This allows the phase of the order parameter to change discontinuously across the weak link, by an amount $\phi = 2\pi\Phi/\Phi_0$, where $\Phi_0 = h/2e$. Such a device is known as a Josephson junction, and one of its most remarkable properties is that it supports a DC current flowing between the two superconductors even in the absence of a voltage bias—the Josephson effect. The current is periodic in the phase difference ϕ across the junction [34] and in a short superconductor-normal metal-superconductor (SNS) junction it is given by:

$$I(\phi) = \frac{e\Delta}{2\hbar} \sum_{p=1}^N \frac{T_p \sin(\phi)}{\sqrt{1 - T_p \sin^2(\phi/2)}}, \quad (1.12)$$

where Δ is the superconducting gap, and T_p are the eigenvalues of $t^\dagger t$, with t the transmission matrix of the normal region in the junction. Additionally, in an SNS junction electrons and holes travel through the junction and Andreev reflect back into each other at the interface with the superconductor. Because the phase factor acquired by electrons

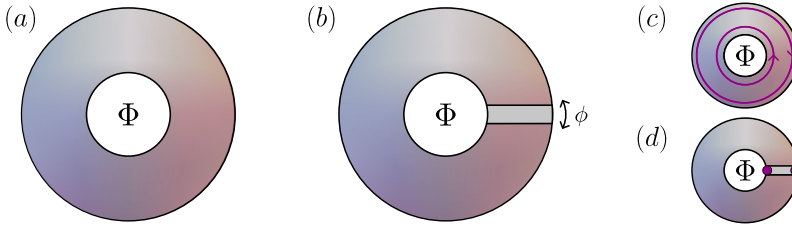


Figure 1.4: (a) A superconducting ring with a magnetic flux Φ . (b) A Josephson junction with phase difference ϕ across the weak link (gray). (c) A superconducting ring that proximitizes a chiral topological insulator with two chiral Majorana modes (purple). (d) A Josephson junction that proximitizes a topological insulator with two Majorana zero modes (purple).

and holes is the same, the Andreev reflection process results in a phase shift of 2ϕ across the junction, giving rise to Andreev bound states localized at the junction and with energies below the superconducting gap Δ . It is these Andreev bound states that carry most of the supercurrent $I(\phi)$ in Eq. (1.12). While the Josephson current is a 2π -periodic function of the phase difference ϕ , it is $h/2e$ -periodic in flux Φ and therefore shows twice the period of the Aharonov-Bohm effect. This is a direct consequence of the pairing of electrons into Cooper pairs and therefore a hallmark of superconductivity.

A period of the Josephson current larger than $h/2e$ is, on the other hand, a signature of topological superconductivity and Majorana zero modes [13]. The quest to create a topological superconductor is a long-term pursuit that relies on carefully proximitizing a semiconductor with strong spin-orbit coupling and broken time-reversal symmetry [35, 36]. Because the topological excitations in superconductors are charge-less Majorana zero modes, a direct extension of Laughlin's charge pumping argument is not successful. Still, topological superconductors respond to flux insertion: vortices in them host Majorana zero modes [37], and by the same principle Josephson junctions that proximitize topological insulators host them too [13]. In the last decade, several experimental platforms have been proposed to observe them: proximitized semiconducting nanowires, planar Josephson junctions, and quantum-dot-based Kitaev chains are the most prominent examples.

Even in the absence of topological superconductivity, planar Josephson junctions exhibit topological phenomena. Reference [38] discovered that Andreev bound states in ballistic and narrow SNS junctions carry current in the direction parallel to the interface. The differential conductance is quantized in units of χ_F , the Euler characteristic of the Fermi surface of the 2DEG, a consequence of the complete absence of backscattering of the Andreev states in the junction. To change the conductance value, the chemical potential of the 2DEG must be tuned so that the Fermi sea topology changes. This is a ballistic effect that requires highly transparent interfaces, and a minimal number of Andreev bound states confined in the junction—a condition satisfied in the short-junction regime. This work gives rise to several questions: *How robust is the absence of backscattering in non-ideal junctions? Does Fermi surface topology protect multi-terminal Andreev transport? What role does superconductivity play in the protection of Andreev transport?*

1.5. THIS THESIS

We summarize the content of this thesis².

CHAPTER 2: TOPOLOGICAL DEFECTS IN OBSTRUCTED ATOMIC INSULATORS

Previous to this thesis, obstructed atomic insulators were identified to host topological defects with quantized charges. This idea was based on the exponentially localized Wannier representation of atomic insulators, which localize in different high symmetry points of the unit cell. In this chapter, we test the hypothesis that topological defects in obstructed topological phases trap quantized charges by constructing two topological defects in a quadrupole insulator: a disclination and a parametric defect. Since disclinations necessarily strain the lattice and parametric defects require closed curves in parameter space, both defects break the four-fold rotation symmetry that protects the quadrupole insulator, even away from their origin. The Wannier representation of the defects is thus determined by the local reflection symmetries of the lattice. Contrary to the hypothesis, we find that the local charge density decays as $\sim 1/r^2$ with distance, leading to a diverging defect charge. Because topological defects are incompatible with four-fold rotation symmetry, we conclude that defect charge quantization is protected by sublattice symmetry, and not higher order topology. Several reported results for the quantized charge of topological defects in obstructed atomic insulators are therefore incorrect.

CHAPTER 3: PFAFFIAN INVARIANT IDENTIFIES MAGNETIC OBSTRUCTED ATOMIC INSULATORS

Reference [39] conjectured that all obstructed atomic insulators are characterized by a Berry-phase-like topological invariant. In this chapter, we disprove this conjecture by deriving a \mathbb{Z}_4 topological invariant for a magnetic obstructed atomic insulator protected by $C_4\mathcal{T}$ symmetry. To formulate this invariant, we apply Stokes' theorem to the Berry curvature over the irreducible Brillouin zone, and constrain the spectrum of the open Wilson lines that compose its boundary. Wilson lines are, however, gauge-dependent, and therefore we use the Pfaffian of a local symmetry operator to fix their gauge ambiguity. As a result, we distinguish the four $C_4\mathcal{T}$ -protected atomic insulators, and establish the correspondence between the invariant and the obstructed phases by constructing a model that captures all phases.

²This text is based on the chapters and papers that compose this thesis.

CHAPTER 4: SCATTERING THEORY OF HIGHER ORDER TOPOLOGICAL PHASES

Do crystalline topological phases respond to flux? To answer this question we generalize the scattering theory for topological invariants to higher-order topological phases. The generalization has a key and non-trivial requirement: the sample geometry with leads attached must respect the crystalline symmetries that protect the topological phase. Because satisfying this requirement requires attaching leads in an arbitrary number of directions, for example in the presence of rotational symmetries, the sample geometry is incompatible with translational invariance. To compensate for the missing momentum-like degrees of freedom, we thread magnetic fluxes through the sample. As a result, we demonstrate that the intrinsic higher order topology is captured by the flux dependence of the reflection matrix. A direct experimental signature of the scattering invariant, for example a pumped observable, remains an open question. Our theory provides an alternative approach for proving bulk–edge correspondence in intrinsic higher order topological phases, especially in the presence of disorder.

Example:

A two-dimensional insulator with two-fold rotational symmetry C_2 and particle-hole symmetry P is the simplest example for illustrating the construction of the scattering invariants in the presence of crystalline symmetries. This system hosts two Majorana zero modes per surface in its second-order topological phase. To satisfy the requirements of the scattering theory, we consider a C_2 symmetric sample geometry with a hole in the center, and C_2 symmetric leads attached to the sample interior and exterior surfaces, as shown in Fig. 1.5. Inserting a magnetic flux Φ through the hole makes the scattering matrix $S(\Phi)$ periodic and $C_2(\Phi) = C_2(0)e^{i\Phi/2}$ acquires a phase factor. Finding the scattering invariant requires constraining $S(\Phi)$ using the C_2 symmetry and the particle-hole symmetry. Because $[S(\Phi), C_2(\Phi)] = 0$, the scattering matrix may be block-diagonalized in the C_2 eigenbasis for any flux value. Additionally, because particle-hole symmetry leaves $\Phi = 0, \pi$ invariant, $S(0)$ and $S(\pi)$ may be made real in the particle-hole basis using P . Moreover, because the C_2 eigenvalues are only real at either $\Phi = 0$ or $\Phi = \pi$, there is a single flux value $\bar{\Phi}$ where both symmetries may be used to simultaneously constrain $S(\Phi)$.

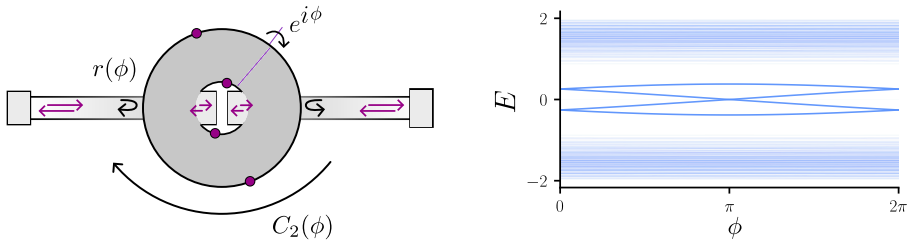


Figure 1.5: (a) Scattering setup for a two-dimensional higher-order topological insulator with C_2 and P symmetries. Each surface of the sample hosts a pair of Majorana zero modes related by the C_2 symmetry (purple dots). (b) Spectral flow of a Hamiltonian protected by C and C_4 in the topological phase. The transparency of the eigenvalues is set by the weight of the wavefunction at the inner edge of the sample. In the trivial phase, an even number of low energy modes cross the Fermi level, while in the topological phase, an odd number of low-energy modes cross the Fermi level. Note that this spectral flow is only schematic, the example in text corresponds to a C_2 symmetric system and therefore has only two low-energy modes per surface.

In the thermodynamic limit, the Majorana zero-modes in the inner edge of the sample are decoupled from the outer edge. Additionally, because at flux $\bar{\Phi}$ the particle-hole and two-fold rotation symmetries commute, the two Majorana zero modes at a same surface may be labeled by different C_2 eigenvalues and thus do not couple. Therefore low-energy Hamiltonian $H(\bar{\Phi})$ and the coupling matrix W are given by:

$$H(\bar{\Phi}) = \begin{pmatrix} 0 & 0 \\ 0 & 0 \end{pmatrix}, \quad W = \begin{pmatrix} t & 0 \\ t^* & 0 \\ 0 & t \\ 0 & t^* \end{pmatrix} \quad (1.13)$$

where t is the coupling strength between the leads and the Majorana zero modes. Using $H(\bar{\Phi})$ and W in the Weidenmüller formula in Eq. (1.5), we find the scattering matrix:

$$S(E=0) = -\sigma_0 \tau_x \quad (1.14)$$

in the particle-hole basis, as S is real. Because $C_2 = \sigma_x \tau_0$, and the reflection matrix $r = S$ at a single normal-superconductor interface, we find that the scattering invariant is:

$$\nu = \det(r_-) = \det(U_{C_2,-} r U_{C_2,-}^\dagger) = -1 \quad (1.15)$$

where $U_{C_2,-}$ is the unitary operator that diagonalizes C_2 , taking into account that r is the particle-hole basis. In the absence of Majorana zero modes $S = 1$, and therefore the scattering invariant $\nu = 1$ in the trivial phase. The matrix determinant arises because in class D the reflection matrix is orthogonal at zero energy, and therefore its eigenvalues are either $+1$ or -1 , giving rise to a \mathbb{Z}_2 invariant.

CHAPTER 5: IDENTIFYING BIASES OF THE MAJORANA SCATTERING INVARIANT

The interfaces between semiconductors and superconductors are nearly impossible to realize disorder-free, making the experimental signatures of Majorana zero modes ambiguous. Experiments only probe topology indirectly: for example, quasi-Majorana states mimic most properties of Majoranas, such as the zero-bias peak in the differential conductance. Establishing a correspondence between an experiment and a theoretical model known to be topological is an approach that resolves this ambiguity.

In this chapter we demonstrate that already theoretically determining whether a finite system is topological is by itself ambiguous. In particular, we show that the scattering topological invariant—a probe of topology most closely related to transport signatures of Majoranas—has multiple biases in finite systems. For example, we identify that quasi-Majorana states also mimic the scattering invariant of Majorana zero modes in intermediate-sized systems. We expect that the bias due to finite size effects is universal, and advocate that the analysis of topology in finite systems should be accompanied by a comparison with the thermodynamic limit. Our results are directly relevant to the applications of the topological gap protocol—the state-of-the-art standard for determining whether a nanowire-based topological superconductor is topological or not.

CHAPTER 6: CHIRAL ADIABATIC TRANSMISSION PROTECTED BY FERMI SURFACE TOPOLOGY

In this chapter, we consider a discrete vortex in a planar Josephson trijunction, a junction where three superconductors with different phase meet at a point. Unexpectedly, we find that the Andreev modes that propagate along each of the junction's arms transmit without any backscattering into one of the other two arms, as shown in Fig. 1.6. The chirality and the number of quantized transmission channels is determined by the topology of the Fermi surface and the vorticity of the superconducting phase differences at the trijunction. We explain this chiral adiabatic transmission (CAT) of Andreev modes as a consequence of the adiabatic evolution of the scattering modes both in momentum and real space. The dispersion relation of the junction then separates the scattering trajectories by introducing inaccessible regions of phase space. We expect that CAT is observable in nonlocal conductance and thermal transport measurements. Furthermore, because it does not rely on particle-hole symmetry, CAT is also possible to observe in metamaterials.

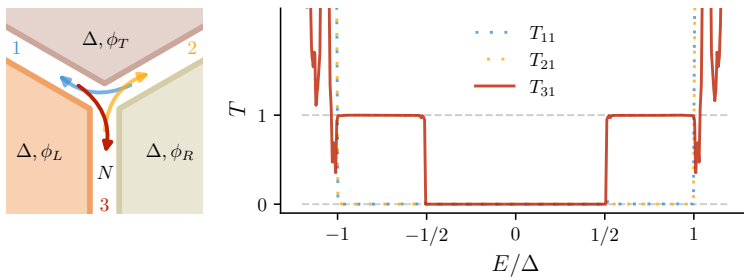


Figure 1.6: (left) A narrow and ballistic planar Josephson trijunction with three superconductors with gap Δ and phases ϕ_L , ϕ_R , and ϕ_T . (right) Transmission of the Andreev modes between the three normal metal (N) arms of the junction.

CHAPTER 7: PYMABLOCK, AN ALGORITHM AND A PACKAGE FOR QUASI-DEGENERATE PERTURBATION THEORY

A common technique in the study of complex quantum-mechanical systems is to reduce the number of degrees of freedom in the Hamiltonian by describing only a selected part of the Hilbert space, for example the low-energy states. Quasi-degenerate perturbation theory allows to do so by finding a unitary transformation that block-diagonalizes the Hamiltonian:

$$H = \begin{pmatrix} H_0^{AA} & 0 \\ 0 & H_0^{BB} \end{pmatrix} + \lambda H', \quad (1.16)$$

where H_0^{AA} and H_0^{BB} are separated by an energy gap, and H' is the perturbation that couples the two subspaces A and B . While the Schrieffer–Wolff transformation achieves this and constructs an effective Hamiltonian, its scaling is suboptimal, it is limited to two subspaces, and implementing it efficiently is both challenging and error-prone.

We introduce an algorithm for constructing an equivalent effective Hamiltonian as well as a Python package, `Pymablock`, that implements it. Our algorithm combines an optimal asymptotic scaling and the ability to handle any number of subspaces and perturbations, with a range of other improvements. The package supports numerical and analytical calculations of any order and it is designed to be interoperable with any other packages for specifying the Hamiltonian. We demonstrate how the package handles constructing a k.p model, analyses a superconducting qubit, and computes the low-energy spectrum of a large tight-binding model. We also compare its performance with reference calculations and demonstrate its efficiency, a summary of which is shown in Fig. 1.7.

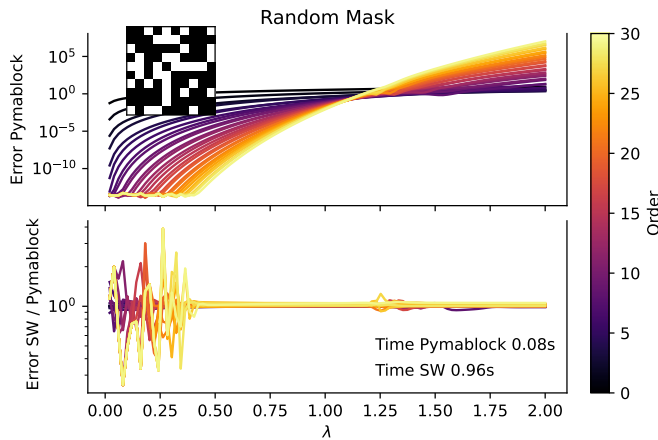


Figure 1.7: Performance comparison of Pymablock and Schrieffer–Wolff perturbation theory for a random Hamiltonian. The goal is to eliminate the white entries of the mask shown in the inset matrix perturbatively. (Top) Absolute error of the eigenvalues of the Pymablock effective Hamiltonian compared to the exact eigenvalues. The value of λ for which curves of the different orders intersect indicates the convergence radius of the perturbative series. (Bottom) Relative error of the eigenvalues of the Pymablock effective Hamiltonian compared to Schrieffer–Wolff perturbation theory. The time spent by Pymablock and Schrieffer–Wolff perturbation theory is shown in text.

REFERENCES

- [1] W. Ehrenberg and R. E. Siday. “The Refractive Index in Electron Optics and the Principles of Dynamics”. In: *Proceedings of the Physical Society. Section B* 62.1 (1949), p. 8. [10.1088/0370-1301/62/1/303](https://doi.org/10.1088/0370-1301/62/1/303).
- [2] Y. Aharonov and D. Bohm. “Significance of Electromagnetic Potentials in the Quantum Theory”. In: *Phys. Rev.* 115 (3 1959), pp. 485–491. [10.1103/PhysRev.115.485](https://doi.org/10.1103/PhysRev.115.485).
- [3] R. G. Chambers. “Shift of an Electron Interference Pattern by Enclosed Magnetic Flux”. In: *Phys. Rev. Lett.* 5 (1 1960), pp. 3–5. [10.1103/PhysRevLett.5.3](https://doi.org/10.1103/PhysRevLett.5.3).
- [4] Y. Aharonov and D. Bohm. “Further Considerations on Electromagnetic Potentials in the Quantum Theory”. In: *Phys. Rev.* 123 (4 1961), pp. 1511–1524. [10.1103/PhysRev.123.1511](https://doi.org/10.1103/PhysRev.123.1511).
- [5] R. A. Webb et al. “Observation of $\frac{h}{e}$ Aharonov-Bohm Oscillations in Normal-Metal Rings”. In: *Phys. Rev. Lett.* 54 (25 1985), pp. 2696–2699. [10.1103/PhysRevLett.54.2696](https://doi.org/10.1103/PhysRevLett.54.2696).
- [6] Sean Washburn and Richard A. Webb and. “Aharonov-Bohm effect in normal metal quantum coherence and transport”. In: *Advances in Physics* 35.4 (1986), pp. 375–422. [10.1080/00018738600101921](https://doi.org/10.1080/00018738600101921).
- [7] D. J. Thouless et al. “Quantized Hall Conductance in a Two-Dimensional Periodic Potential”. In: *Phys. Rev. Lett.* 49 (6 1982), pp. 405–408. [10.1103/PhysRevLett.49.405](https://doi.org/10.1103/PhysRevLett.49.405).
- [8] R. B. Laughlin. “Quantized Hall conductivity in two dimensions”. In: *Phys. Rev. B* 23 (10 1981), pp. 5632–5633. [10.1103/PhysRevB.23.5632](https://doi.org/10.1103/PhysRevB.23.5632).
- [9] N. Regnault and B. Andrei Bernevig. “Fractional Chern Insulator”. In: *Phys. Rev. X* 1 (2 2011), p. 021014. [10.1103/PhysRevX.1.021014](https://doi.org/10.1103/PhysRevX.1.021014).
- [10] Adolfo G. Grushin et al. “Characterization and stability of a fermionic $\nu = 1/3$ fractional Chern insulator”. In: *Phys. Rev. B* 91 (3 2015), p. 035136. [10.1103/PhysRevB.91.035136](https://doi.org/10.1103/PhysRevB.91.035136).
- [11] C. L. Kane and E. J. Mele. “ Z_2 Topological Order and the Quantum Spin Hall Effect”. In: *Phys. Rev. Lett.* 95 (14 2005), p. 146802. [10.1103/PhysRevLett.95.146802](https://doi.org/10.1103/PhysRevLett.95.146802).
- [12] Liang Fu and C. L. Kane. “Time reversal polarization and a Z_2 adiabatic spin pump”. In: *Phys. Rev. B* 74 (19 2006), p. 195312. [10.1103/PhysRevB.74.195312](https://doi.org/10.1103/PhysRevB.74.195312).
- [13] Liang Fu and C. L. Kane. “Josephson current and noise at a superconductor/quantum-spin-Hall-insulator/superconductor junction”. In: *Phys. Rev. B* 79 (16 2009), p. 161408. [10.1103/PhysRevB.79.161408](https://doi.org/10.1103/PhysRevB.79.161408).
- [14] Fan Zhang and C. L. Kane. “Anomalous topological pumps and fractional Josephson effects”. In: *Phys. Rev. B* 90 (2 2014), p. 020501. [10.1103/PhysRevB.90.020501](https://doi.org/10.1103/PhysRevB.90.020501).
- [15] Xavier Waintal et al. “Computational quantum transport”. In: *Preprint* (2024). [10.48550/arXiv.2407.16257](https://arxiv.org/abs/10.48550/arXiv.2407.16257).

- [16] Christoph W Groth et al. “Kwant: a software package for quantum transport”. In: *New Journal of Physics* 16.6 (2014), p. 063065. [10.1088/1367-2630/16/6/063065](https://doi.org/10.1088/1367-2630/16/6/063065).
- [17] Hans A Weidenmüller. “On the theory of nuclear reactions:(I). Shell-model calculations in the continuum”. In: *Nuclear Physics* 75.1 (1966), pp. 189–208.
- [18] R. Landauer. “Spatial Variation of Currents and Fields Due to Localized Scatterers in Metallic Conduction”. In: *IBM Journal of Research and Development* 1.3 (1957), pp. 223–231. [10.1147/rd.13.0223](https://doi.org/10.1147/rd.13.0223).
- [19] Rolf Landauer. “Electrical resistance of disordered one-dimensional lattices”. In: *The Philosophical Magazine: A Journal of Theoretical Experimental and Applied Physics* 21.172 (1970), pp. 863–867. [10.1080/14786437008238472](https://doi.org/10.1080/14786437008238472).
- [20] M. Büttiker. “Four-Terminal Phase-Coherent Conductance”. In: *Phys. Rev. Lett.* 57 (14 1986), pp. 1761–1764. [10.1103/PhysRevLett.57.1761](https://doi.org/10.1103/PhysRevLett.57.1761).
- [21] P. W. Brouwer. “Scattering approach to parametric pumping”. In: *Phys. Rev. B* 58 (16 1998), R10135–R10138. [10.1103/PhysRevB.58.R10135](https://doi.org/10.1103/PhysRevB.58.R10135).
- [22] I. C. Fulga, F. Hassler, and A. R. Akhmerov. “Scattering theory of topological insulators and superconductors”. In: *Phys. Rev. B* 85 (16 2012), p. 165409. [10.1103/PhysRevB.85.165409](https://doi.org/10.1103/PhysRevB.85.165409).
- [23] Dganit Meidan, Tobias Micklitz, and Piet W. Brouwer. “Topological classification of adiabatic processes”. In: *Phys. Rev. B* 84 (19 2011), p. 195410. [10.1103/PhysRevB.84.195410](https://doi.org/10.1103/PhysRevB.84.195410).
- [24] Wladimir A Benalcazar, B Andrei Bernevig, and Taylor L Hughes. “Quantized electric multipole insulators”. In: *Science* 357.6346 (2017), pp. 61–66. [10.1126/science.aah6442](https://doi.org/10.1126/science.aah6442).
- [25] Frank Schindler et al. “Higher-order topological insulators”. In: *Science Advances* 4.6 (2018), eaat0346. [10.1126/sciadv.aat0346](https://doi.org/10.1126/sciadv.aat0346).
- [26] Zhi-Da Song, Luis Elcoro, and B Andrei Bernevig. “Twisted bulk-boundary correspondence of fragile topology”. In: *Science* 367.6479 (2020), pp. 794–797. [10.1126/science.aaz7659](https://doi.org/10.1126/science.aaz7659).
- [27] Bitan Roy and Vladimir Juričić. “Dislocation as a bulk probe of higher-order topological insulators”. In: *Phys. Rev. Res.* 3 (3 2021), p. 033107. [10.1103/PhysRevResearch.3.033107](https://doi.org/10.1103/PhysRevResearch.3.033107).
- [28] Zhi-Kang Lin et al. “Topological Wannier cycles induced by sub-unit-cell artificial gauge flux in a sonic crystal”. In: *Nature Materials* 21.4 (2022), pp. 430–437. [10.1038/s41563-022-01200-w](https://doi.org/10.1038/s41563-022-01200-w).
- [29] Frank Schindler et al. “Topological zero-dimensional defect and flux states in three-dimensional insulators”. In: *Nature communications* 13.1 (2022), p. 5791. [10.1038/s41467-022-33471-x](https://doi.org/10.1038/s41467-022-33471-x).
- [30] Yizhi You et al. “Higher-order symmetry-protected topological states for interacting bosons and fermions”. In: *Phys. Rev. B* 98 (23 2018), p. 235102. [10.1103/PhysRevB.98.235102](https://doi.org/10.1103/PhysRevB.98.235102).

- [31] Yizhi You, Julian Bibo, and Frank Pollmann. “Higher-order entanglement and many-body invariants for higher-order topological phases”. In: *Phys. Rev. Res.* 2 (3 2020), p. 033192. [10.1103/PhysRevResearch.2.033192](https://doi.org/10.1103/PhysRevResearch.2.033192).
- [32] Ryo Takahashi, Yutaro Tanaka, and Shuichi Murakami. “Bulk-edge and bulk-hinge correspondence in inversion-symmetric insulators”. In: *Phys. Rev. Res.* 2 (1 2020), p. 013300. [10.1103/PhysRevResearch.2.013300](https://doi.org/10.1103/PhysRevResearch.2.013300).
- [33] Max Geier, Ion Cosma Fulga, and Alexander Lau. “Bulk-boundary-defect correspondence at disclinations in rotation-symmetric topological insulators and superconductors”. In: *SciPost Phys.* 10 (2021), p. 092. [10.21468/SciPostPhys.10.4.092](https://doi.org/10.21468/SciPostPhys.10.4.092).
- [34] C. W. J. Beenakker. “Universal limit of critical-current fluctuations in mesoscopic Josephson junctions”. In: *Phys. Rev. Lett.* 67 (27 1991), pp. 3836–3839. [10.1103/PhysRevLett.67.3836](https://doi.org/10.1103/PhysRevLett.67.3836).
- [35] Roman M. Lutchyn, Jay D. Sau, and S. Das Sarma. “Majorana Fermions and a Topological Phase Transition in Semiconductor-Superconductor Heterostructures”. In: *Phys. Rev. Lett.* 105 (7 2010), p. 077001. [10.1103/PhysRevLett.105.077001](https://doi.org/10.1103/PhysRevLett.105.077001).
- [36] Yuval Oreg, Gil Refael, and Felix von Oppen. “Helical Liquids and Majorana Bound States in Quantum Wires”. In: *Phys. Rev. Lett.* 105 (17 2010), p. 177002. [10.1103/PhysRevLett.105.177002](https://doi.org/10.1103/PhysRevLett.105.177002).
- [37] N. Read and Dmitry Green. “Paired states of fermions in two dimensions with breaking of parity and time-reversal symmetries and the fractional quantum Hall effect”. In: *Phys. Rev. B* 61 (15 2000), pp. 10267–10297. [10.1103/PhysRevB.61.10267](https://doi.org/10.1103/PhysRevB.61.10267).
- [38] Pok Man Tam and Charles L. Kane. “Probing Fermi Sea Topology by Andreev State Transport”. In: *Phys. Rev. Lett.* 130 (9 2023), p. 096301. [10.1103/PhysRevLett.130.096301](https://doi.org/10.1103/PhysRevLett.130.096301).
- [39] Jennifer Cano et al. “Topology invisible to eigenvalues in obstructed atomic insulators”. In: *Phys. Rev. B* 105 (12 2022), p. 125115. [10.1103/PhysRevB.105.125115](https://doi.org/10.1103/PhysRevB.105.125115).

2

TOPOLOGICAL DEFECTS IN A DOUBLE-MIRROR QUADRUPOLE INSULATOR DISPLACE DIVERGING CHARGE

Isidora Araya Day, Dániel Varjas, and Anton R. Akhmerov

We show that topological defects in quadrupole insulators do not host quantized fractional charges, contrary to what their Wannier representation indicates. In particular, we test the charge quantization hypothesis based on the Wannier representation of a disclination and a parametric defect. Since disclinations necessarily strain the lattice and parametric defects require closed curves in parameter space, both defects break four-fold rotation symmetry, even away from their origin. The Wannier representation of the defects is thus determined by local reflection symmetries. Contrary to the hypothesis, we find that the local charge density decays as $\sim 1/r^2$ with distance, leading to a diverging defect charge. Because topological defects are incompatible with four-fold rotation symmetry, we conclude that defect charge quantization is protected by sublattice symmetry, and not higher order topology.

Own contribution to work: Implemented the numerical simulations, and contributed to interpreting the results and writing the manuscript.

Parts of this chapter have been published as *Topological defects in a double-mirror quadrupole insulator displace diverging charge*, *SciPost Phys. Core* 5, 053 (2022).

A topological quadrupole insulator hosts quantized half-integer corner charges [1, 2, 3, 4, 5], with the Benalcazar-Bernevig-Hughes (BBH) model being a canonical example of this phase (see Fig. 2.1(a)). In the bulk a quantized quadrupole moment serves as a topological invariant, providing the quadrupole insulator with a bulk-corner correspondence [6, 7]. While the precise definition of the bulk quadrupole moment is a subtle issue [8, 9], the bulk-corner correspondence is guaranteed by the combination of the four-fold rotation symmetry and two anti-commuting reflection symmetries.

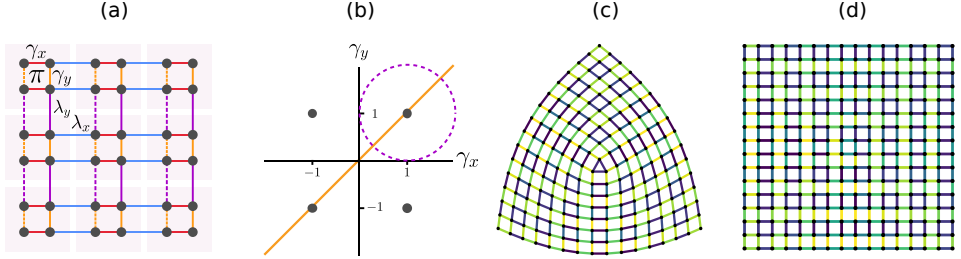


Figure 2.1: (a) The BBH model has four orbitals per unit cell, connected via $\gamma_{x,y}$ and $\lambda_{x,y}$ hoppings. The dashed hopping lines have an extra phase of $-\pi$ with respect to the solid lines, threading a π flux through each plaquette. (b) The phase diagram shows that the bulk gap closes at the grey dots, when $|\gamma_x/\lambda_x| = 1$ and $|\gamma_y/\lambda_y| = 1$. The orange line indicates the set of parameters that preserve four-fold rotation symmetry and the dashed purple curve is a circular gapped path centered in $(\gamma_x, \gamma_y) = (1, 1)$ with radius $\gamma_r = 1$. (c) A disclination is created by effectively removing one orbital from a unit cell. We expect both defects to host localized fractional charges. (d) A parametric defect is inserted in the BBH model using a gapped path in the phase diagram. The parametrization of the hoppings shifts the strongly bounded unit cells around the defect, creating a charge deficiency at it. The hopping strengths are given by the loop shown in (b).

2.1. INTRODUCTION

Disclinations in quadrupole insulators were proposed to serve as bulk probes of topology, emulating the behavior of the corners by trapping quantized fractional charges [10]. Furthermore, Refs. [10, 11] demonstrated that if a band insulator admits a real space Wannier representation—*i. e.* has a vanishing Chern number—then the non-uniform distribution of the Wannier centers establishes the corner and defect charges quantization. The topology of a quadrupole insulator was recently probed via disclination defects, successfully finding defect bound states in microwave metamaterials [12].

An alternative pathway to creating topological defects, so far not explored in the context of quadrupole insulators, is to make the Hamiltonian parameters position-dependent [13, 14] by making the Hamiltonian $H(\mathbf{k}, \mathbf{r})$ gradually vary with position. In conventional topological phases, as long as $H(\mathbf{k}, \mathbf{r})$ remains gapped far away from the defect, the presence of a defect bound state is protected by the defect invariant. Breaking the four-fold rotation symmetry while preserving both reflection symmetries allows us to introduce non-contractible loops in the space of the Hamiltonians of a quadrupole insulator [15], see Fig. 2.1(b). Therefore, similarly to the quantized disclination charge, one may expect that the charge of a topological parametric defect is quantized in a quadrupole insulator.

The topological arguments presented in earlier works, as well as the Wannier center considerations above suggest that the defect charge quantization is a direct consequence

of topology. There is, however, no rigorous proof that the defect charge quantization is indeed a consequence of the quantized quadrupole moment. Our goal, therefore, is to put the charge quantization hypothesis to a test and rigorously identify the conditions under which the defect charge is quantized.

2.2. TOPOLOGICAL DEFECTS IN THE QUADRUPOLE INSULATOR

To test the hypothesis we use the BBH tight-binding model: a two-dimensional lattice with four orbitals per unit cell. Figure 2.1(a) shows the model, which corresponds to a quadrupole insulator that admits a Wannier representation, and whose Bloch Hamiltonian is:

$$\mathcal{H}(\mathbf{k}) = [\gamma_x + \lambda_x \cos(k_x)]\Gamma_4 + \lambda_x \sin(k_x)\Gamma_3 + [\gamma_y + \lambda_y \cos(k_y)]\Gamma_2 + \lambda_y \sin(k_y)\Gamma_1,$$

where $\gamma_{x,y}$ and $\lambda_{x,y}$ account for intra-cell and inter-cell hopping amplitudes, respectively. Here $\Gamma_k = -\sigma_2 \otimes \tau_k$ for $k \in \{1, 2, 3\}$, and $\Gamma_4 = \sigma_1 \otimes \tau_0$, with σ_i and τ_i Pauli matrices acting on the orbital degrees of freedom.

We introduce a disclination by removing the quarter of the lattice that is spanned by $\theta \in [3\pi/2, 2\pi)$, changing the positions of the remaining sites according to $\theta \rightarrow 4/3\theta$, while keeping $r \equiv |\mathbf{r}|$ constant (see Fig. 2.1(c)). We keep the lattice isotropic by choosing $\gamma_x = \gamma_y = \gamma$ and $\lambda_x = \lambda_y = \lambda$. If the disclination center lies between the strongly coupled sites, the disclination removes an orbital from one of the strongly coupled clusters. The Wannier centers are located at the center of these clusters, such that the resulting strongly bonded triangle has 3/2 electrons at half-filling, and therefore a half-integer charge. An alternative way to come to the same conclusion is by observing that each of the three corners must have a charge 1/2 because the quadrupole insulator is in its topological phase. The remaining half integer charge must then be bound to the disclination center—the only remaining lattice defect.

Both the argument above and the proof of Ref. [10] ignore the effect of lattice distortion around the defect center. To study the effect of strain on the tight-binding model, we modulate the hopping amplitudes by changing them proportionally to the bond length:

$$\begin{aligned} \gamma'(\mathbf{r}_1, \mathbf{r}_2) &= \gamma(1 + \alpha_\gamma(|\mathbf{r}_1 - \mathbf{r}_2| - a)) \\ \lambda'(\mathbf{r}_1, \mathbf{r}_2) &= \lambda(1 + \alpha_\lambda(|\mathbf{r}_1 - \mathbf{r}_2| - a)), \end{aligned} \quad (2.1)$$

where γ' and λ' are hopping amplitudes coupling the orbitals that would be connected by a hopping γ or λ without a disclination, $a = 1/2$ is the bond rest length, and $\mathbf{r}_1, \mathbf{r}_2$ are the coordinates of the two orbitals. The factors α_γ and α_λ are the electron-lattice couplings. To keep the system in the topological phase, we require that far away from the disclination the ratio $|\gamma'/\lambda'| < 1$. Because the disclination necessarily introduces strain, without fine-tuning that ensures $\alpha_\gamma = \alpha_\lambda = 0$, the disclination necessarily breaks the four-fold rotation symmetry even far away from its center.

A parametric defect is an alternative way to create a quantized fractional charge. We create this defect in the BBH model at an arbitrary lattice coordinate \mathbf{r}_0 . We fix $\lambda_x = \lambda_y = 1$ and vary the hopping strengths γ_x and γ_y with displacement \mathbf{r} from the defect. For simplicity we consider a defect where γ_x and γ_y only depend on the angle θ between \mathbf{r} and the x -axis. We require that as the angle θ of \mathbf{r} in polar coordinates advances by 2π , the vector (γ_x, γ_y) encloses a loop around the point $(1, 1)$. As an example,

Fig. 2.1(d) shows the hopping strengths corresponding to the circular loop in the parameter space shown in purple in Fig. 2.1(b). The center of the defect has an odd-sized cluster of strongly coupled sites, which contains a half-integer number of electrons at half-filling, similarly to a disclination. Tracking the positions of the Wannier centers within the unit cell [15] as a function of r , shown in Fig. 2.2, demonstrates the presence of the defect charge.

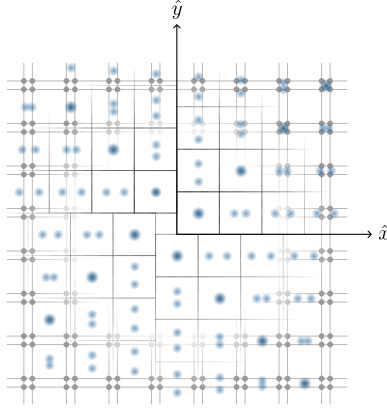


Figure 2.2: The parametric defect interpolates between the trivial (top right quadrant) and topological (bottom left quadrant) phases of the BBH model (grey dots connected by lines) by smoothly modulating the hoppings and preserving local mirror symmetries. While in the trivial phase the Wannier centers (blue circles) are localized at the center of the unit cell, they are localized at the corners in the topological phase. In all unit cells the Wannier centers come in pairs invariant under local mirror symmetries. The square cells, each centered in between pairs of nearest Wannier centers, tile the space away from the defect. The unoccupied quarter unit cell at $r = 0$ corresponds to the missing fractional charge $e/2$.

While the defect charge quantization hypothesis relies only on the spatial symmetry arguments, the BBH model Eq. (2.1) is minimal and therefore it has additional symmetries. In particular, the sublattice symmetry of the BBH model by itself leads to charge quantization. To see this we consider the local charge density in a unit cell

$$\rho_{ij} = \sum_{E_l < E_F} \sum_{\alpha} |\Psi_{\alpha l}^{ij}|^2, \quad (2.2)$$

where $E_l \leq E_F \equiv 0$ labels the occupied energies with the Fermi level fixed in the bulk gap and $\alpha \in \{1, 2, 3, 4\}$ labels the four orbitals of the unit cell. The indices i, j are the lattice coordinates of a unit cell, where the defect origin is at $i = 0, j = 0$, and $\Psi_{\alpha l}^{ij} = \langle i, j, \alpha | \Psi_l \rangle$. We express the total number of states in a unit cell through the contributions of eigenstates at different energies:

$$\begin{aligned} 4 &= \sum_{E_l < 0} \sum_{\alpha=1}^4 |\Psi_{\alpha l}^{ij}|^2 + \sum_{E_l=0} \sum_{\alpha=1}^4 |\Psi_{\alpha l}^{ij}|^2 + \sum_{E_l > 0} \sum_{\alpha=1}^4 |\Psi_{\alpha l}^{ij}|^2 \\ &= 2 \sum_{E_l < 0} \sum_{\alpha=1}^4 |\Psi_{\alpha l}^{ij}|^2 + \sum_{E_l=0} \sum_{\alpha=1}^4 |\Psi_{\alpha l}^{ij}|^2 = 2\rho_{ij} + \sum_{E_l=0} \sum_{\alpha=1}^4 |\Psi_{\alpha l}^{ij}|^2, \end{aligned} \quad (2.3)$$

where we use the sublattice symmetry in the second equality. Finally, the total defect charge q_{tot} integrated over a square-shaped area surrounding the defect is the charge excess with respect to the uniform charge density $\rho_{ij} = 2$:

$$q_{\text{tot}}(R) = \sum_{i,j=-R/2}^{R/2} (\rho_{ij} - 2). \quad (2.4)$$

Substituting Eq. (2.3) into Eq. (2.4) we obtain

$$q_{\text{tot}}(R) = -\frac{1}{2} \sum_{i,j=-R/2}^{R/2} \sum_{E_l=0}^4 \sum_{\alpha=1}^4 |\Psi_{\alpha l}^{ij}|^2. \quad (2.5)$$

Therefore in presence of the sublattice symmetry, the total defect charge is $N_0/2$, where N_0 is the number of zero-energy modes localized at the defect. The number of the zero-energy modes, in turn, is defined by the second winding number of the Hamiltonian around the defect, and protected already by the sublattice symmetry alone [14]. Furthermore, because of the bulk gap, the zero-modes are exponentially localized.

Sublattice symmetry also guarantees the disclination charge quantization, despite the center of the disclination locally breaking the sublattice symmetry. To demonstrate this, we use perturbation theory and consider $3/4^{\text{th}}$ of the BBH lattice the unperturbed Hamiltonian. This Hamiltonian inherits sublattice symmetry from the BBH model and therefore it hosts fractional and exponentially localized charges at its six corners. To obtain a disclination, we add a perturbation that consists on the hopping terms that couple orbitals from neighboring unit cells on the position-transformed lattice, such that the lattice is glued. Using that the system is gapped, we conclude that the Fermi level Green's function, and therefore charge density, changes by an amount that decays exponentially with distance from the disclination's origin. Because sublattice symmetry applies near the sample corners, we conclude there is a $1/2$ charge that may only be located near the disclination.

To distinguish the topological properties of the quadrupole insulator from the effect of the sublattice symmetry, we add hoppings with magnitude δ connecting sites from the same sublattice in the neighboring unit cells. In order to preserve the anti-commuting reflection and the four-fold rotation symmetries of the original model, we choose the value of all these hoppings to be the same. We change the sign of the additional hoppings when gluing the different sides of the wedge at the disclination in order for the cut to be gauge-compatible with the rest of the lattice.

2.3. DIVERGENCE OF THE DEFECT CHARGE

We numerically study the defect charge inserting the defects at the center of a $L^2 = 50 \times 50$ square system. We create the parametric defect using a circular path of radius $\gamma_r = 1$ centered at $\gamma_x/\lambda_x = \gamma_y/\lambda_y = 1$ (see Fig. 2.1(b)), and the disclination using $\gamma = \lambda/2 = 0.5$ and $\alpha_\gamma = \alpha_\lambda = \alpha_\delta = 1$. To obtain the defect charges we integrate the charge density distributions shown in Fig. 2.3(a-d). Our results in Fig. 2.4(a) confirm that the total defect charge converges to $1/2$ in presence of sublattice symmetry, and demonstrate an apparent convergence to a non-quantized value otherwise, unless the electron-lattice coupling is neglected, in agreement with Ref. [10]. This lack of quantization is explained by considering

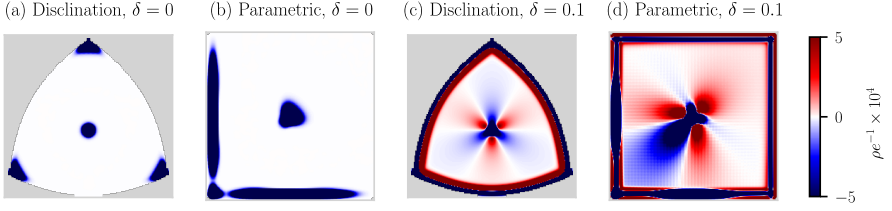


Figure 2.3: Local charge density at half-filling in the defects. A defect displaces both negative (blue) and positive (red) excess charge in the absence of sublattice symmetry, resulting in a divergent defect charge. (a-b) The parametric defect and the disclination with sublattice symmetry. (c-d) The parametric defect and the disclination without sublattice symmetry.

the absolute charge deviation:

$$q(R) = \sum_{i,j=-R/2}^{R/2} |\rho_{ij} - 2|. \quad (2.6)$$

While the absolute charge deviation converges to a finite value in presence of sublattice symmetry, it diverges when the sublattice symmetry and the local four-fold rotation symmetry are broken, as shown in Fig. 2.4(b). According to our expectations, the defect charge convergence is exponential (Fig. 2.4(c)). On the other hand, the divergence matches a $\sim 1/r^2$ decay of the local charge density, as confirmed by $\Delta q(R) = q(R+1) - q(R) \propto 1/R$ in Fig. 2.4(d). The lack of absolute convergence in combination with conditional convergence means that depending on the summation order, the defect charge may assume an arbitrary value according to the Riemann rearrangement theorem. While the absolute convergence of charge deviation is required, it is also a weaker condition on charge quantization than the vanishing charge variance studied in Ref. [16].

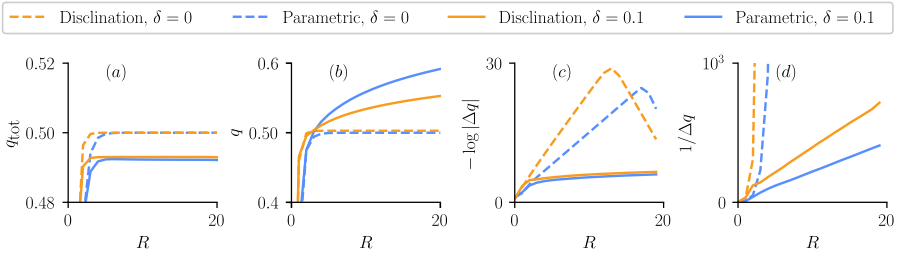


Figure 2.4: The defect charge diverges in the absence of sublattice symmetry. (a) The total charge q_{tot} integrates to $1/2$ only when sublattice symmetry is present (dashed lines), otherwise q_{tot} depends on the integration area (solid lines), demonstrating the lack of absolute convergence. (b) In the presence of sublattice symmetry (dashed lines), the charge deviation q is quantized to $1/2$, otherwise it diverges (solid lines). The divergence of the parametric defect's charge is more pronounced when the paths are asymmetric in parameter space. (c) The defect charge deviation converges exponentially when $\delta = 0$ (dashed lines), as $-\log|q(R+1) - q(R)| \propto R$. (d) For $\delta \neq 0$ the local charge density decays as $1/R^2$ as indicated by $q(R+1) - q(R) \propto 1/R$.

In order to confirm the total charge divergence we determine the asymptotic behav-

ior of the local charge density away from the defect. Sufficiently far away from the defect in a large enough sample, the Hamiltonian's position dependence becomes small compared to the inverse energy gap while it changes slowly in space. Thus, the local real space variations of the Hamiltonian determine the charge density and its local response is captured by perturbation theory that treats the position dependence as a perturbation. To account for $\rho \propto 1/r^2$ found via numerical simulations, it is enough to consider a general position-dependent perturbation expanded to second order around \mathbf{r}^* far away from the defect center \mathbf{r}_0 ,

$$H'(\delta\mathbf{r}) = H'^0 + \delta\mathbf{r}_i H_i'^1 + \delta\mathbf{r}_i H_{ij}'^2 \delta\mathbf{r}_j + h.c., \quad (2.7)$$

where H'^0 , H'^1 and H'^2 are the zeroth, first and second order components of the Hamiltonian perturbation, and $\delta\mathbf{r} \equiv \mathbf{r} - \mathbf{r}^*$. By construction, H'^0 , H'^1 , and H'^2 are invariant under reflection. While H'^1 is reflection-symmetric, $\mathbf{r}_i H_i'^1$ is odd under reflection symmetries. The perturbative response of the local charge density is invariant under reflection and it is a power series of H'^1 and H'^2 . As a consequence of being odd under reflection, the first order contribution of H'^1 to the charge density vanishes, while the contribution of H'^2 and the second order contribution of H'^1 remain. Because both types of defects have a finite $dH/d\theta \rightarrow \text{const}$ with $r \rightarrow \infty$, $H'^1 \sim 1/r$ and $H'^2 \sim 1/r^2$. Therefore, we confirm that the charge density universally decays as $1/r^2$ unless the Hamiltonian is fine-tuned or it has additional symmetries.

2.4. CONCLUSION

In summary, we investigated charge quantization of defect bound states in quadrupole insulators as it was predicted in Refs. [10, 11] and reported in Ref. [12]. Specifically, we analyzed a disclination and a parametric defect in the BBH model and found that the previously reported charge quantization is a consequence of the sublattice symmetry, or of neglecting the effects of lattice strain around the disclination. The importance of sublattice symmetry was appreciated in the early studies of soliton-fermion bound states in one-dimensional models [17, 18, 19]. This symmetry is not inherent to quadrupole insulators, but without it the defect charge is not quantized, because the absolute charge deviation diverges. Our findings demonstrate that topological protection of the filled bands, despite being characterized by a quantized topological invariant, is weaker than the protection of individual states in topological insulators.

ACKNOWLEDGEMENTS

We thank B. Seradjeh for drawing our attention to relevant literature. D. V. is thankful to R. Queiroz for enlightening discussions.

DATA AVAILABILITY

The code used to produce the reported results is available on Zenodo [20].

Author contributions D. V. defined the project goal and formulated the hypothesis. I. A. D. implemented the numerical checks with guidance from D. V. and A. R. A. All authors interpreted the results and contributed to the project planning. I. A. D. and A. R. A. wrote the manuscript with input from D. V.

Funding information This work was supported by the Netherlands Organization for Scientific Research (NWO/OCW), as part of the Frontiers of Nanoscience program and an NWO VIDI grant 016.Vidi.189.180. We acknowledge the support from QuTech Academy through the Scholarship. D. V. was supported by the Swedish Research Council (VR) and the Knut and Alice Wallenberg Foundation.

REFERENCES

- [1] Wladimir A. Benalcazar, B. Andrei Bernevig, and Taylor L. Hughes. “Electric multipole moments, topological multipole moment pumping, and chiral hinge states in crystalline insulators”. In: *Phys. Rev. B* 96 (24 2017), p. 245115. [10.1103/PhysRevB.96.245115](https://doi.org/10.1103/PhysRevB.96.245115).
- [2] Marc Serra-Garcia et al. “Observation of a phononic quadrupole topological insulator”. In: *Nature* 555.7696 (2018), pp. 342–345. [10.1038/nature25156](https://doi.org/10.1038/nature25156).
- [3] Christopher W Peterson et al. “A quantized microwave quadrupole insulator with topologically protected corner states”. In: *Nature* 555.7696 (2018), pp. 346–350. [10.1038/nature25777](https://doi.org/10.1038/nature25777).
- [4] Stefan Imhof et al. “Topoelectrical-circuit realization of topological corner modes”. In: *Nature Physics* 14.9 (2018), pp. 925–929. [10.1038/s41567-018-0246-1](https://doi.org/10.1038/s41567-018-0246-1).
- [5] Christopher W Peterson et al. “A fractional corner anomaly reveals higher-order topology”. In: *Science* 368.6495 (2020), pp. 1114–1118. [10.1126/science.aba7604](https://doi.org/10.1126/science.aba7604).
- [6] Wladimir A Benalcazar, B Andrei Bernevig, and Taylor L Hughes. “Quantized electric multipole insulators”. In: *Science* 357.6346 (2017), pp. 61–66. [10.1126/science.aah6442](https://doi.org/10.1126/science.aah6442).
- [7] Martin Rodriguez-Vega, Abhishek Kumar, and Babak Seradjeh. “Higher-order Floquet topological phases with corner and bulk bound states”. In: *Phys. Rev. B* 100 (8 2019), p. 085138. [10.1103/PhysRevB.100.085138](https://doi.org/10.1103/PhysRevB.100.085138).
- [8] Seishiro Ono, Luka Trifunovic, and Haruki Watanabe. “Difficulties in operator-based formulation of the bulk quadrupole moment”. In: *Phys. Rev. B* 100 (24 2019), p. 245133. [10.1103/PhysRevB.100.245133](https://doi.org/10.1103/PhysRevB.100.245133).
- [9] Haruki Watanabe and Seishiro Ono. “Corner charge and bulk multipole moment in periodic systems”. In: *Phys. Rev. B* 102 (16 2020), p. 165120. [10.1103/PhysRevB.102.165120](https://doi.org/10.1103/PhysRevB.102.165120).
- [10] Tianhe Li et al. “Fractional disclination charge in two-dimensional C_n -symmetric topological crystalline insulators”. In: *Phys. Rev. B* 101 (11 2020), p. 115115. [10.1103/PhysRevB.101.115115](https://doi.org/10.1103/PhysRevB.101.115115).
- [11] Wladimir A. Benalcazar, Tianhe Li, and Taylor L. Hughes. “Quantization of fractional corner charge in C_n -symmetric higher-order topological crystalline insulators”. In: *Phys. Rev. B* 99 (24 2019), p. 245151. [10.1103/PhysRevB.99.245151](https://doi.org/10.1103/PhysRevB.99.245151).
- [12] Christopher W Peterson et al. “Trapped fractional charges at bulk defects in topological insulators”. In: *Nature Physics* 589.1 (2021), pp. 376–380. <https://doi.org/10.1038/s41586-020-03117-3>.

- [13] B. Seradjeh, C. Weeks, and M. Franz. “Fractionalization in a square-lattice model with time-reversal symmetry”. In: *Phys. Rev. B* 77 (3 2008), p. 033104. [10.1103/PhysRevB.77.033104](https://doi.org/10.1103/PhysRevB.77.033104).
- [14] Jeffrey C. Y. Teo and C. L. Kane. “Topological defects and gapless modes in insulators and superconductors”. In: *Phys. Rev. B* 82 (11 2010), p. 115120. [10.1103/PhysRevB.82.115120](https://doi.org/10.1103/PhysRevB.82.115120).
- [15] Eslam Khalaf et al. “Boundary-obstructed topological phases”. In: *Phys. Rev. Research* 3 (1 2021), p. 013239. [10.1103/PhysRevResearch.3.013239](https://doi.org/10.1103/PhysRevResearch.3.013239).
- [16] S. Kivelson and J. R. Schrieffer. “Fractional charge, a sharp quantum observable”. In: *Phys. Rev. B* 25 (10 1982), pp. 6447–6451. [10.1103/PhysRevB.25.6447](https://doi.org/10.1103/PhysRevB.25.6447).
- [17] R. Jackiw and C. Rebbi. “Solitons with fermion number $\frac{1}{2}$ ”. In: *Phys. Rev. D* 13 (12 1976), pp. 3398–3409. [10.1103/PhysRevD.13.3398](https://doi.org/10.1103/PhysRevD.13.3398).
- [18] W. P. Su, J. R. Schrieffer, and A. J. Heeger. “Solitons in Polyacetylene”. In: *Phys. Rev. Lett.* 42 (25 1979), pp. 1698–1701. [10.1103/PhysRevLett.42.1698](https://doi.org/10.1103/PhysRevLett.42.1698).
- [19] A. J. Heeger et al. “Solitons in conducting polymers”. In: *Rev. Mod. Phys.* 60 (3 1988), pp. 781–850. [10.1103/RevModPhys.60.781](https://doi.org/10.1103/RevModPhys.60.781).
- [20] Isidora Araya Day, Anton R. Akhmerov, and Dániel Varjas. *Topological defects in a double-mirror quadrupole insulator displace diverging charge*. Feb. 2022. [10.5281/zenodo.5939935](https://doi.org/10.5281/zenodo.5939935).

3

PFAFFIAN INVARIANT IDENTIFIES MAGNETIC OBSTRUCTED ATOMIC INSULATORS

Isidora Araya Day, Anastasiia Varentcova, Dániel Varjas and Anton R. Akhmerov

We derive a \mathbb{Z}_4 topological invariant that extends beyond symmetry eigenvalues and Wilson loops and classifies two-dimensional insulators with a $C_4\mathcal{T}$ symmetry. To formulate this invariant, we consider an irreducible Brillouin zone and constrain the spectrum of the open Wilson lines that compose its boundary. We fix the gauge ambiguity of the Wilson lines by using the Pfaffian at high symmetry momenta. As a result, we distinguish the four $C_4\mathcal{T}$ -protected atomic insulators, each of which is adiabatically connected to a different atomic limit. We establish the correspondence between the invariant and the obstructed phases by constructing both the atomic limit Hamiltonians and a $C_4\mathcal{T}$ -symmetric model that interpolates between them. The phase diagram shows that $C_4\mathcal{T}$ insulators allow ± 1 and 2 changes of the invariant, where the latter is overlooked by symmetry indicators.

Own contribution to work: Contributed to developing the idea, searching the literature, writing the code, and writing the manuscript.

Parts of this chapter have been published as *Pfaffian invariant identifies magnetic obstructed atomic insulators*, SciPost Phys. 15, 114 (2023).

3.1. INTRODUCTION

Topological crystalline insulators are phases of matter where it is impossible to define exponentially localized Wannier functions that respect the crystalline symmetries [1, 2]. Obstructed atomic insulators, on the contrary, allow symmetric and exponentially localized Wannier functions whose centers occupy maximal Wyckoff positions, such that a continuous and symmetric deformation cannot move them [3, 4, 5]. The symmetry representations of the occupied orbitals at high symmetry momenta—symmetry indicators [6, 7, 8]—distinguish part of the obstructed atomic insulators, but not all [9]. Reference [9] constructed Berry phase-based topological invariants that distinguish these phases in specific examples and put forward the conjecture of the universality of this approach.

Two-dimensional magnetic insulators belonging to the magnetic plane group pd' that are symmetric under the product of four-fold rotation (C_4) and spinful time-reversal symmetry (\mathcal{T}) support distinct obstructed atomic insulating phases. A general Wyckoff position has an orbit of size four, hence a crystal with two occupied orbitals must have the Wannier centers located at maximal Wyckoff positions. This restriction allows the four distinct phases labeled by ν shown in Fig. 3.1: a spin singlet in the center or the corner of the Wigner-Seitz unit cell, and two phases with z -oriented spins located at the middle of the unit cell edge. The product δ of the eigenvalues of $C_2 = (C_4\mathcal{T})^2$ at the C_2 -invariant momenta $X = (\pi, 0)$ or $Y = (0, \pi)$ differentiate the singlet phases from the spin-polarized ones [10]. However, even the full set of symmetry indicators only provides an incomplete topological classification: phases $\nu = 0$ and $\nu = 2$ have identical representation content at every high-symmetry momentum. The crystalline symmetry guarantees that all the Wilson loops along reciprocal lattice vectors provide the same information as the symmetry indicators, and therefore distinguishing all four phases requires extending the approach of Ref. [9] to construct the topological invariant.

Our main result is a topological invariant ν that captures all the obstructed phases in a $C_4\mathcal{T}$ -symmetric two-dimensional magnetic insulator. We identify the invariant by constructing a discrete quantity that utilizes the symmetry constraints on the wave functions, following a reasoning similar to the \mathbb{Z}_2 invariant in topological insulators [11, 12, 6]. Instead of the time-reversal symmetry operator \mathcal{T} , we use the operator

$$\Theta = \frac{C_4\mathcal{T} - (C_4\mathcal{T})^{-1}}{\sqrt{2}}, \quad (3.1)$$

that protects the Kramers-like pairs at the high symmetry momenta $\Gamma = (0, 0)$ and $M = (\pi, \pi)$ [13, 14]. This definition of Θ is different from $\Theta = (C_4\mathcal{T} + C_4^{-1}\mathcal{T})/\sqrt{2}$ used in Refs. [13, 14], which relies on using the operators C_4 and \mathcal{T} absent within the symmetry group, but it is equivalent otherwise.

3.2. PFAFFIAN TOPOLOGICAL INVARIANT

To exploit the symmetry, we formulate the invariant by using the occupied states only in the irreducible Brillouin zone (IBZ). Without loss of generality, we choose the irreducible Brillouin zone shown in Fig. 3.2, with the boundary path $\Gamma \rightarrow M \rightarrow X \rightarrow M \rightarrow \Gamma$. Stokes'

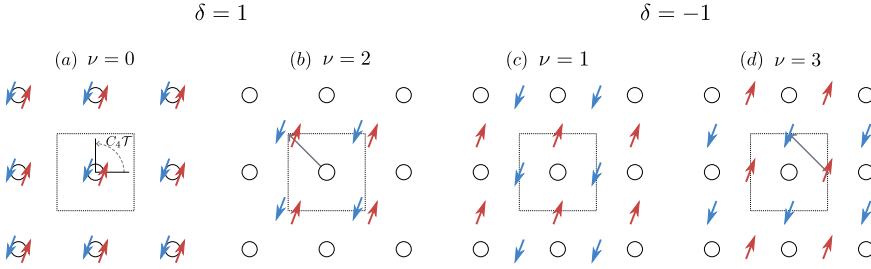


Figure 3.1: Different atomic limits of the $C_4\mathcal{T}$ -symmetric insulator. The system is made out of atoms (empty circles) placed in the center of the Wigner-Seitz unit cell (square). The $C_4\mathcal{T}$ symmetry (grey dashed arrow) rotates the system by 90° around the atom and flips the spins. The four distinct atomic insulators are: (a) spin singlet located on the atom, (b) spin singlet at the corner of the unit cell, and (c-d) spins pointing in $\pm z$ -direction. The two spins (red/blue) in a unit cell are of different orbital characters in all panels. The phases shown in panels (b) and (d) are related to the ones in panels (a) and (c) by a fractional lattice translation (grey solid arrows).

theorem applied to the IBZ equates the Berry flux to the boundary Berry phase:

$$\int_{\text{IBZ}} \text{tr} \mathcal{F} d\mathbf{k}^2 - \oint_{\partial\text{IBZ}} \text{tr} \mathcal{A} d\mathbf{k} = 0 \pmod{2\pi}, \quad (3.2)$$

where $\mathcal{A}_{mn}(\mathbf{k}) = i \langle m\mathbf{k} | \partial_{\mathbf{k}} | n\mathbf{k} \rangle$ is the non-Abelian Berry connection, $\mathcal{F}_{mn}(\mathbf{k}) = \nabla \times \mathcal{A}_{mn}(\mathbf{k})$ is the non-Abelian Berry curvature, and $|n\mathbf{k}\rangle$ is an orthonormal basis of the occupied eigenstates of the Bloch Hamiltonian. Since the Berry connection integral may change by multiples of 2π upon singular gauge transformations, while the Berry flux is fully gauge-invariant, Eq. (3.2) only holds modulo 2π . We rewrite the Stokes' theorem in terms of the Wilson line

$$\mathcal{W}_{\mathcal{C}} = \exp\left(i \int_{\mathcal{C}} \mathcal{A} d\mathbf{k}\right), \quad (3.3)$$

where the exponent is path-ordered along \mathcal{C} . Under a gauge transformation of the occupied wavefunctions $|n\mathbf{k}\rangle \rightarrow \sum_m |m\mathbf{k}\rangle U_{mn}(\mathbf{k})$, the Wilson line transforms according to $\mathcal{W}_{\mathcal{C}} \rightarrow U^\dagger(\mathbf{k}_f) \mathcal{W}_{\mathcal{C}} U(\mathbf{k}_i)$, where \mathbf{k}_i and \mathbf{k}_f are the initial and final points of \mathcal{C} . If the path \mathcal{C} is closed, Eq. (3.3) defines a Wilson loop, whose eigenvalues are gauge invariant, while the Wilson line spectrum is gauge dependent [15]. Substituting Eq. (3.3) into Eq. (3.2) yields

$$\int_{\text{IBZ}} \text{tr} \mathcal{F} d\mathbf{k}^2 + i \log \det \mathcal{W}_{\partial\text{IBZ}} = 0 \pmod{2\pi}. \quad (3.4)$$

This identity defines the discrete quantity that we use for the topological invariant. However, without applying symmetry constraints, Eq. (3.4) carries no information due to the gauge ambiguity of 2π .

To resolve the gauge ambiguity, we split the Wilson loop $\mathcal{W}_{\partial\text{IBZ}}$ into three symmetry-constrained parts. Specifically, we consider the Wilson lines from $\Gamma \rightarrow M$, $M \rightarrow X \rightarrow M$, and $M \rightarrow \Gamma$. Because all of these Wilson lines start and end at $C_4\mathcal{T}$ -invariant momenta, we constrain their spectrum using the Θ operator. We define the dressed Wilson line determinant as

$$\widetilde{\det} \mathcal{W}_{\mathcal{C}} = \text{pf}^{-1} w(\mathbf{k}_f) \det \mathcal{W}_{\mathcal{C}} \text{pf} w(\mathbf{k}_i). \quad (3.5)$$

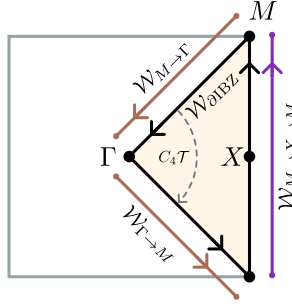


Figure 3.2: The irreducible Brillouin zone (yellow) spans the Brillouin zone together with its $C_4\mathcal{T}$ -images. Its boundary is constrained by $C_4\mathcal{T}$ -symmetry (grey dashed arrow), so we split the Wilson loop $\mathcal{W}_{\partial\text{IBZ}}$ (black arrows) at the high symmetry momenta Γ and M . Two $C_4\mathcal{T}$ -equivalent Wilson lines, $\mathcal{W}_{\Gamma\rightarrow M}$ and $\mathcal{W}_{M\rightarrow\Gamma}$, (brown arrows), and a Wilson loop, $\mathcal{W}_{M\rightarrow X\rightarrow M}$, (purple arrow), compose the resulting path.

Here \mathbf{k}_i and \mathbf{k}_f must be either Γ or M , the start and end points of the path \mathcal{C} , respectively. The antisymmetric overlap matrix $w(\mathbf{k})$ is the projection of the Θ operator on the occupied states $w_{mn}(\mathbf{k}) = \langle n\mathbf{k}|\Theta|m\mathbf{k}\rangle$, and pf is the Pfaffian. An alternative approach to define the dressed Wilson line is to use the generalized Pfaffian [16] of the $C_4\mathcal{T}$ overlap matrix $w'_{mn}(\mathbf{k}) = \langle n\mathbf{k}|C_4\mathcal{T}|m\mathbf{k}\rangle$, or the Pfaffian of the antisymmetrized overlap matrix [17], $(w' - w'^T)/2$. Due to the gauge transformation property $w(\mathbf{k}) \rightarrow U^\dagger(\mathbf{k})w(\mathbf{k})U^*(\mathbf{k})$, and the identity $\text{pf}(CAC^T) = \det(C)\text{pf}(A)$, the dressed Wilson line determinant is gauge invariant. Furthermore, because the three paths combine into the contour of the IBZ,

$$\det \mathcal{W}_{\partial\text{IBZ}} = \widetilde{\det} \mathcal{W}_{\Gamma\rightarrow M} \widetilde{\det} \mathcal{W}_{M\rightarrow X\rightarrow M} \widetilde{\det} \mathcal{W}_{M\rightarrow\Gamma} = \widetilde{\det}^2 \mathcal{W}_{\Gamma\rightarrow M} \widetilde{\det} \mathcal{W}_{M\rightarrow X\rightarrow M}. \quad (3.6)$$

Here we used that $M \rightarrow \Gamma$ is the $C_4\mathcal{T}$ -image of $\Gamma \rightarrow M$, and therefore $\widetilde{\det} \mathcal{W}_{\Gamma\rightarrow M} = \widetilde{\det} \mathcal{W}_{M\rightarrow\Gamma}$. Finally, we recognize that the initial and final momenta of $M \rightarrow X \rightarrow M$ are the same, so that $\widetilde{\det} \mathcal{W}_{M\rightarrow X\rightarrow M} = \det \mathcal{W}_{M\rightarrow X\rightarrow M}$ is the Wilson loop determinant. The C_2 -invariance of this path further constrains the Wilson loop determinant

$$\det \mathcal{W}_{M\rightarrow X\rightarrow M} = \prod_{n \in \text{occ}} \frac{\zeta_n(X)}{\zeta_n(M)} = \prod_{n \in \text{occ}} \zeta_n(X) \equiv \delta, \quad (3.7)$$

where $\zeta_n(\mathbf{k}) = \pm i$ is the eigenvalue of the operator C_2 of the n th occupied band at C_2 -invariant momenta [18]. For the second equality, we observe that the product of C_2 eigenvalues at the M point is always trivial due to the Kramers-like degeneracy. As a consequence, the Wilson loop determinant is equal to the C_2 symmetry indicator $\delta = \pm 1$.

To construct the invariant we substitute Eq. (3.6) into Eq. (3.4), subtract the logarithm of Eq. (3.7), and obtain

$$\nu = \frac{1}{\pi} \left[\int_{\text{IBZ}} \text{tr} \mathcal{F} d\mathbf{k}^2 + 2i \log \widetilde{\det} \mathcal{W}_{\Gamma\rightarrow M} \right] \pmod{4}. \quad (3.8)$$

This is our main result. The invariant is defined modulo 4 because each dressed Wilson line determinant is well-defined modulo 2π . The invariant is also quantized to integer values and it stays constant as long as the spectrum is gapped. However, at this point, the relation between the invariant and the different phases is not yet established.

3.3. MODEL HAMILTONIAN CONSTRUCTION

To show that ν distinguishes the four atomic insulators shown in Fig. 3.1, we test it by applying it to the corresponding phases. We construct the Hamiltonians of each atomic limit from coupled spinful p -type orbitals. The orbitals are located at the center of the unit cell and transform into each other under C_4 rotations. Using the standard representation of spin 1/2, yields

$$C_4\mathcal{T} = \tau_y e^{-i\sigma_z\pi/4} \sigma_y \mathcal{K}, \quad (3.9)$$

where τ_i are the Pauli matrices in orbital space in the basis p_x, p_y , σ_i are the Pauli matrices in spin space, and \mathcal{K} is complex conjugation. In the trivial limit, we couple opposite spins within each orbital in the unit cell to obtain a spin singlet located on each atom, as shown in Fig. 3.3(a). In the obstructed atomic limits the spins are localized in between unit cells, hence we couple opposite spins from the same orbital type that belong to neighboring unit cells, as shown in Fig. 3.3(b-d). Specifically, to couple opposite spin-polarized states in all the atomic limits, we use the operator

$$S(\mathbf{r}, \delta\mathbf{r}, \mathbf{\Omega}) = |\mathbf{r} + \delta\mathbf{r}, \mathbf{\Omega}\rangle \langle \mathbf{r}, -\mathbf{\Omega}| + |\mathbf{r}, -\mathbf{\Omega}\rangle \langle \mathbf{r} + \delta\mathbf{r}, \mathbf{\Omega}|, \quad (3.10)$$

where $|\mathbf{r}\rangle$ is the state localized at a unit cell with coordinates \mathbf{r} , $\delta\mathbf{r}$ is the displacement between the coupled unit cells, and $|\mathbf{\Omega}\rangle$ is a spin oriented in the xy -plane along the direction $\mathbf{\Omega}$. We require $|\mathbf{\Omega}\rangle = -iC_2|-\mathbf{\Omega}\rangle$. This guarantees that the occupied eigenstate of S is a $+i$ eigenstate of a C_2 rotation around $\mathbf{r} + \delta\mathbf{r}/2$ or, in other words, it is a $+z$ -spin located at $\mathbf{r} + \delta\mathbf{r}/2$. Without loss of generality, we choose $\mathbf{\Omega} = \hat{y}$. Since the occupied states in the atomic limits are z -aligned spins of different orbital characters, as shown in Fig. 3.3, we use the projector on the two orthogonal p -orbitals

$$T_{\pm} = \frac{1}{2} \left[1 \pm (\tau_z \cos \phi + \tau_x \sin \phi) \right], \quad (3.11)$$

to couple spins within orthogonal orbitals. Here ϕ is an arbitrary orbital polarization in xy -plane that we choose as $\phi = 0$. The atomic limits shown in Fig. 3.3 are then given by the Hamiltonians

$$H^{(\nu)} = \sum_{\mathbf{r}} \left[T_+ S(\mathbf{r}, \delta\mathbf{r}_\nu, \mathbf{\Omega}) - T_- S(\mathbf{r}, \hat{\mathbf{z}} \times \delta\mathbf{r}_\nu, \hat{\mathbf{z}} \times \mathbf{\Omega}) \right] \quad (3.12)$$

for $\nu = 0, 1, 2, 3$, where $\delta\mathbf{r}_0 = 0$, $\delta\mathbf{r}_1 = \hat{x}$, $\delta\mathbf{r}_2 = \hat{x} + \hat{y}$, and $\delta\mathbf{r}_3 = \hat{y}$. We recognize that $H^{(3)} = -H^{(1)}$, in agreement with the atomic limits in Fig. 3.1(c-d) being the time-reversed images of each other.

3.4. CONFIRMATION OF THE INVARIANT

To confirm that the invariant is quantized and that it only changes under gap closing transitions, we construct a model of a $C_4\mathcal{T}$ -invariant planar magnetic insulator with no other symmetries. Its Hamiltonian interpolates between the four atomic limits and contains additional onsite terms breaking extra symmetries

$$H = \alpha H^{(0)} + \beta H^{(1)} + \gamma H^{(2)} + \sum_{i=4}^{N=23} \lambda_i H^{(i)}. \quad (3.13)$$

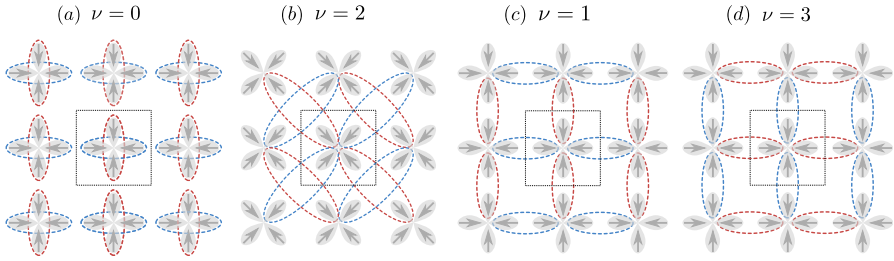


Figure 3.3: Construction of the atomic limits from coupling opposite spins within p_x and p_y orbitals (orthogonal pairs of arrows) located at the center of the unit cell (square). Positive couplings (red ellipses) result in $+z$ -oriented spins, while negative ones (blue ellipses) result in $-z$ -oriented spins.

Here α , β , and γ are the weights of the atomic limit Hamiltonians, and λ_i are the amplitudes of the 19 other $C_4\mathcal{T}$ -invariant onsite terms $H^{(i)}$, which we generate using Qsymm [19]. We choose $\alpha \in [0, 1]$, $\beta \in [-1, 1]$, and $\gamma = 1 - \alpha - |\beta| \in [0, 1]$, such that the $\nu = 3$ atomic limit is included in the negative range of β . We use Adaptive [20] to sample Hamiltonians whose energy gaps we find via numerical minimization. We numerically compute the invariant using occupied band projectors to discretize the Wilson lines [15] over a Brillouin zone grid of 20×20 momenta, where we choose the upper right quadrant of the Brillouin zone as the IBZ for simplicity. Choosing a different IBZ does not change the invariant because all the possible IBZ are smoothly connected to one another, but Eq. (3.8) only takes integer values. The phase diagram in Fig. 3.4(a) shows the interpolation between the atomic limits without additional $C_4\mathcal{T}$ -invariant terms ($\lambda_i = 0$), where the conservation of the orbital polarization protects the gapless region. To break additional symmetries we set $\lambda_i = 0.08$ and obtain the phase diagram in Fig. 3.4(b). Our results confirm that ν is quantized and it labels the four phases, each adiabatically connected to an atomic limit. The phase diagrams show transitions with ν changing by ± 1 or by 2, where the former are accompanied by a gap closing at the X point that changes the C_2 indicator of Eq. (3.7). If the gap closes at a different momentum, the transition is overlooked by the C_2 indicator, but not by the invariant ν , which changes by 2.

The construction of the atomic limits shown in Fig. 3.3, suggests that the boundary charge of each phase depends on the lattice termination. To determine the bulk-boundary correspondence of the phases, we compute the charge density in square and rhombus-shaped lattices, such that the termination cuts a different number of bonds along the boundary. We place the Fermi level inside the gap, $E_F = 0.15$, and compute the deviation of charge per unit cell from $2e$ —the charge density at half-filling. We use Kwant [21] to construct square and rhombus geometries of $L^2 = 7 \times 7$ and $L^2 = 9 \times 9$ unit cells, respectively, for each phase. We choose the amplitudes α , β , and γ as 0.6, 0.2, 0.2, where the biggest amplitude determines the phase, and set the symmetry breaking terms $\lambda_i = 0.01$. While the trivial phase lacks boundary modes in either geometry, the obstructed phases localize $1/2e$ per bond cut by the boundary, as shown in Fig. 3.5.

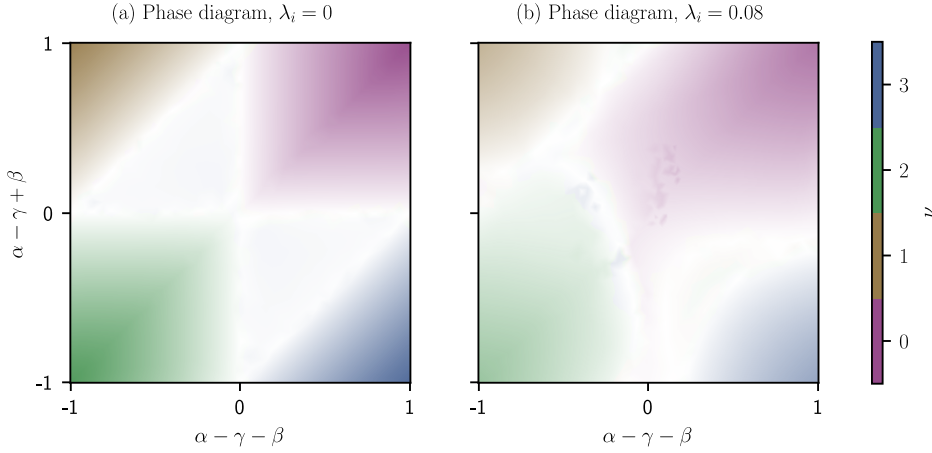


Figure 3.4: Phase diagram of the $C_4\mathcal{T}$ model without (a) and with (b) additional symmetry breaking terms. The invariant is quantized and it distinguishes the four atomic limits at the corners of panel (a). Away from the atomic limits, the invariant stays quantized and the energy gap becomes smaller (increasing transparency). Across phase transitions the invariant changes by ± 1 and 2 via energy gap closings (white) at X or a different momentum, respectively.

3.5. CONCLUSIONS

In summary, we derived an invariant that distinguishes the inequivalent atomic insulating phases of the $p4'$ planar magnetic group. We applied Stokes' theorem to the Berry connection over the irreducible Brillouin zone and exploited the $C_4\mathcal{T}$ symmetry to constrain the phase contributed by the open Wilson lines and a Wilson loop. While the Wilson loop contribution is equal to that of the eigenvalues of C_2 at the X point, and is therefore insufficient to distinguish all phases, the Berry flux and the Wilson lines complete the \mathbb{Z}_4 invariant. Alternatively, our invariant is equivalent to the vorticity of the Pfaffian of the overlap matrix w over half a Brillouin zone modulo 4, similar to the \mathbb{Z}_2 invariant Refs. [11, 12, 6, 13, 14], although this formulation has the disadvantage of requiring a smooth gauge. We constructed models away from the atomic limits and found that the obstructed phases may undergo both transitions changing the invariant by ± 1 or 2, depending on whether the energy gap closes at X or a different momentum.

Our work confirms that the Berry phase alone is insufficient to classify obstructed atomic insulators protected by magnetic space groups. Applying the approach presented here to other magnetic groups will allow to complete the construction of topological invariants that distinguish all obstructed atomic insulating phases. Different values of the topological invariant may exist in neighboring domains of altermagnets [22], where the \mathcal{T} symmetry is spontaneously broken. The bulk-boundary correspondence will then govern the spin and charge properties of the domain walls, and therefore influence their energetic stability.

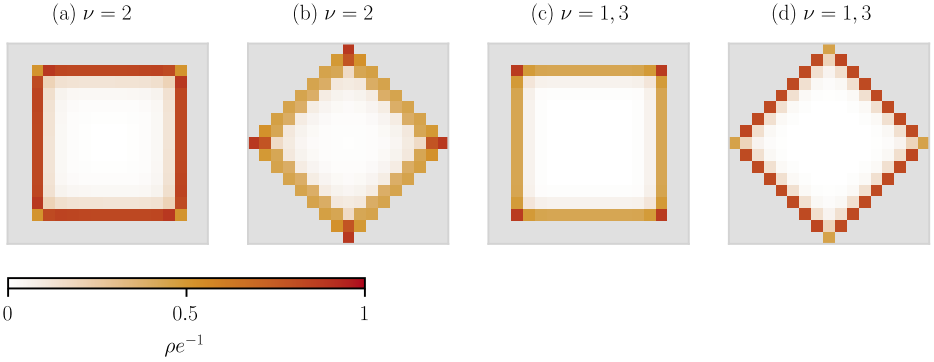


Figure 3.5: The local charge density of the four phases depends on the termination of the lattice, in agreement with the construction procedure. In the obstructed phase $\nu = 2$, $1e$ per unit cell localizes at the edge, and $1/2e$ at the corner in a square lattice (a), and vice versa in a rhombus geometry (b). In the obstructed phases $\nu = 1$ and $\nu = 3$, $1/2e$ per unit cell localizes at the edge, and $1e$ at the corner in a square lattice (c), and vice versa in a rhombus geometry (d).

ACKNOWLEDGEMENTS

We are grateful to I. C. Fulga, K. K. Pöyhönen, A. Lau, H. Spring, A. L. R. Manesco, and F. Schindler for fruitful discussions.

DATA AVAILABILITY

The code used to produce the reported results is available on Zenodo [23].

Author contributions D. V. initiated the project and identified the initial formulation of the invariant. A. V. implemented the computation of the invariant with input from D. V., validated it, studied the bulk boundary correspondence, and wrote the initial summary with D. V. D. V. and A. R. A. constructed the atomic limits model. I. A. D. identified the relevant literature, and developed the idea to its final form with D. V. and A. R. A. I. A. D. wrote the final implementation of the code with input from A. R. A., and wrote the manuscript with input from D. V. and A. R. A. The project was managed by A. R. A. with contributions from D. V.

Funding information This work was supported by the Netherlands Organization for Scientific Research (NWO/OCW) as part of the Frontiers of Nanoscience program, and an NWO VIDI grant 016.Vidi.189.180. D. V. was supported by NWO VIDI Grants 680-47-537, the Swedish Research Council (VR), and the Knut and Alice Wallenberg Foundation.

REFERENCES

- [1] Alexey A. Soluyanov and David Vanderbilt. “Wannier representation of \mathbb{Z}_2 topological insulators”. In: *Phys. Rev. B* 83 (3 2011), p. 035108. [10.1103/PhysRevB.83.035108](https://doi.org/10.1103/PhysRevB.83.035108).

- [2] Nicola Marzari et al. “Maximally localized Wannier functions: Theory and applications”. In: *Rev. Mod. Phys.* 84.4 (2012), p. 1419. [10.1103/RevModPhys.84.1419](https://doi.org/10.1103/RevModPhys.84.1419).
- [3] Barry Bradlyn et al. “Topological quantum chemistry”. In: *Nature* 547.7663 (2017), pp. 298–305. [10.1038/nature23268](https://doi.org/10.1038/nature23268).
- [4] Jennifer Cano et al. “Building blocks of topological quantum chemistry: Elementary band representations”. In: *Phys. Rev. B* 97 (3 2018), p. 035139. [10.1103/PhysRevB.97.035139](https://doi.org/10.1103/PhysRevB.97.035139).
- [5] Jennifer Cano and Barry Bradlyn. “Band representations and topological quantum chemistry”. In: *Annu. Rev. Condens. Ma. P.* 12 (2021), pp. 225–246. [10.1146/annurev-conmatphys-041720-124134](https://doi.org/10.1146/annurev-conmatphys-041720-124134).
- [6] Liang Fu and C. L. Kane. “Topological insulators with inversion symmetry”. In: *Phys. Rev. B* 76 (4 2007), p. 045302. [10.1103/PhysRevB.76.045302](https://doi.org/10.1103/PhysRevB.76.045302).
- [7] Jorrit Kruthoff et al. “Topological Classification of Crystalline Insulators through Band Structure Combinatorics”. In: *Phys. Rev. X* 7 (4 2017), p. 041069. [10.1103/PhysRevX.7.041069](https://doi.org/10.1103/PhysRevX.7.041069).
- [8] Hoi Chun Po, Ashvin Vishwanath, and Haruki Watanabe. “Symmetry-based indicators of band topology in the 230 space groups”. In: *Nat. Commun.* 8.1 (2017), pp. 1–9. [10.1038/s41467-017-00133-2](https://doi.org/10.1038/s41467-017-00133-2).
- [9] Jennifer Cano et al. “Topology invisible to eigenvalues in obstructed atomic insulators”. In: *Phys. Rev. B* 105 (12 2022), p. 125115. [10.1103/PhysRevB.105.125115](https://doi.org/10.1103/PhysRevB.105.125115).
- [10] Rui-Xing Zhang and Chao-Xing Liu. “Topological magnetic crystalline insulators and corepresentation theory”. In: *Phys. Rev. B* 91 (11 2015), p. 115317. [10.1103/PhysRevB.91.115317](https://doi.org/10.1103/PhysRevB.91.115317).
- [11] C. L. Kane and E. J. Mele. “ Z_2 Topological Order and the Quantum Spin Hall Effect”. In: *Phys. Rev. Lett.* 95 (14 2005), p. 146802. [10.1103/PhysRevLett.95.146802](https://doi.org/10.1103/PhysRevLett.95.146802).
- [12] Liang Fu and C. L. Kane. “Time reversal polarization and a Z_2 adiabatic spin pump”. In: *Phys. Rev. B* 74 (19 2006), p. 195312. [10.1103/PhysRevB.74.195312](https://doi.org/10.1103/PhysRevB.74.195312).
- [13] Heqiu Li and Kai Sun. “Pfaffian Formalism for Higher-Order Topological Insulators”. In: *Phys. Rev. Lett.* 124 (3 2020), p. 036401. [10.1103/PhysRevLett.124.036401](https://doi.org/10.1103/PhysRevLett.124.036401).
- [14] Heqiu Li and Kai Sun. “Topological insulators and higher-order topological insulators from gauge-invariant one-dimensional lines”. In: *Phys. Rev. B* 102 (8 2020), p. 085108. [10.1103/PhysRevB.102.085108](https://doi.org/10.1103/PhysRevB.102.085108).
- [15] Aris Alexandradinata, Xi Dai, and B Andrei Bernevig. “Wilson-loop characterization of inversion-symmetric topological insulators”. In: *Phys. Rev. B* 89.15 (2014), p. 155114. [10.1103/PhysRevB.89.155114](https://doi.org/10.1103/PhysRevB.89.155114).
- [16] Dániel Varjas. “Generalizations of the Pfaffian to non-antisymmetric matrices”. In: *Preprint* (2022). [10.48550/arXiv.2209.02578](https://doi.org/10.48550/arXiv.2209.02578).
- [17] Aris Alexandradinata and B. Andrei Bernevig. “Berry-phase description of topological crystalline insulators”. In: *Phys. Rev. B* 93 (20 2016), p. 205104. [10.1103/PhysRevB.93.205104](https://doi.org/10.1103/PhysRevB.93.205104).

- [18] Chen Fang, Matthew J. Gilbert, and B. Andrei Bernevig. “Bulk topological invariants in noninteracting point group symmetric insulators”. In: *Phys. Rev. B* 86 (11 2012), p. 115112. [10.1103/PhysRevB.86.115112](https://doi.org/10.1103/PhysRevB.86.115112).
- [19] Dániel Varjas, Tómas Ö. Rosdahl, and Anton R. Akhmerov. “Qsymm: algorithmic symmetry finding and symmetric Hamiltonian generation”. In: *New Journal of Physics* 20.9 (2018), p. 093026. [10.1088/1367-2630/aadf67](https://doi.org/10.1088/1367-2630/aadf67).
- [20] Bas Nijholt et al. “Adaptive: parallel active learning of mathematical functions”. In: *Zenodo* 1182437 (2019). [10.5281/zenodo.6600606](https://doi.org/10.5281/zenodo.6600606).
- [21] Christoph W Groth et al. “Kwant: a software package for quantum transport”. In: *New Journal of Physics* 16.6 (2014), p. 063065. [10.1088/1367-2630/16/6/063065](https://doi.org/10.1088/1367-2630/16/6/063065).
- [22] Libor Šmejkal, Jairo Sinova, and Tomas Jungwirth. “Emerging Research Landscape of Altermagnetism”. In: *Phys. Rev. X* 12 (4 2022), p. 040501. [10.1103/PhysRevX.12.040501](https://doi.org/10.1103/PhysRevX.12.040501).
- [23] Isidora Araya Day et al. *Pfaffian invariant identifies magnetic obstructed atomic insulators*. 2022. [10.5281/zenodo.7006801](https://doi.org/10.5281/zenodo.7006801).

4

SCATTERING THEORY OF HIGHER ORDER TOPOLOGICAL PHASES

R. Johanna Zijderfeld, **Isidora Araya Day**, and Anton R. Akhmerov

The surface states of intrinsic higher order topological phases are protected by the spatial symmetries of a finite sample. This property makes the existing scattering theory of topological invariants inapplicable because the scattering geometry is either incompatible with the symmetry or does not probe the bulk topology. We resolve this obstacle by using a symmetric scattering geometry that probes transport from the inside to the outside of the sample. We demonstrate that the intrinsic higher order topology is captured by the flux dependence of the reflection matrix. Our finding follows from identifying the spectral flow of a flux line as a signature of higher order topology. We show how this scattering approach applies to several examples of higher order topological insulators and superconductors. Our theory provides an alternative approach for proving bulk–edge correspondence in intrinsic higher order topological phases, especially in presence of disorder.

Own contribution to work: Contributed to the initial idea, the final project scope, identifying the topological invariants, writing code, and writing the manuscript.

Parts of this chapter have been published as *Scattering theory of higher order topological phases*, [SciPost Phys.](#) 19, 058 (2025).

4.1. INTRODUCTION

The protection of surface states in higher order topological phases is more subtle than in topological insulators. Similar to strong topological insulators, higher order topological insulators (HOTIs) host surface states protected by local symmetries (time-reversal, particle-hole, or chiral), but they rely on additional spatial symmetries [1]. While in strong topological phases the existence of the edge state is guaranteed on the whole surface, in HOTIs any point of the surface may be gapped and the surface state may be freely moved around. In two dimensions, for example, a second order topological insulator with chiral symmetry hosts zero-dimensional corner states at zero energy [2]. If this system has reflection symmetries, these states may be removed by modifying the lattice termination—such phases are called extrinsic HOTIs [3, 4, 5]—shown in Fig. 4.1(a). An intrinsic HOTI, on the other hand, hosts corner states protected by the bulk–boundary correspondence. In two dimensions, for example, the combination of chiral and four-fold rotation guarantees that changing the surface of the sample in a symmetric way may not remove the corner states, see Fig. 4.1(b).

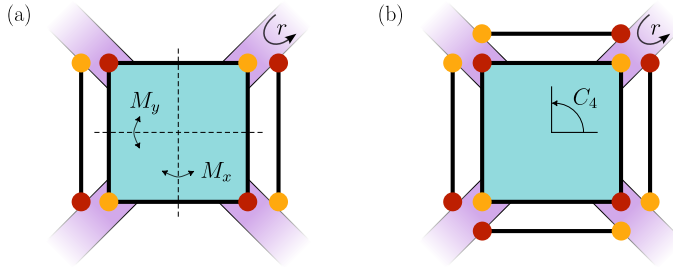


Figure 4.1: Extrinsic and intrinsic higher order phases in the BBH model. The leads (purple) are attached to the corners of the sample to probe the corner states in the different sublattices (red and orange) via the reflection matrix r . (a) An extrinsic phase has states that may be removed by changing the lattice termination (vertical chains) (b) An intrinsic phase has states that are protected by the bulk topology and cannot be removed by changing the lattice termination.

Despite the different nature of the surface states, important properties of topological insulators also apply to higher order phases. First, some higher order phases are stable in the presence of disorder, similar to strong topological phases [6, 7, 8, 9, 10]. This protection follows from the observation that removing a protected surface state requires coupling it with its symmetry partner, which, however, is located at the opposite edge of the sample. Therefore, because disorder acts locally, it does not remove the protected surface states. Secondly, several works used flux response and dislocation defects as a signature of higher order topology [11, 12, 13, 14, 15, 16, 17, 18], generalizing the Laughlin argument. This is reminiscent of the spectral flow in strong topological phases. We thus identify two open questions:

- Can we characterize the topology of a HOTI in the presence of disorder?
- Is there a correspondence between surface states existing at boundaries of symmetric samples and flux response?

We adopt the scattering perspective to answer both questions. The scattering approach considers a transport setup and studies the reflection matrix from the surface of a finite sample. Previous works demonstrated that the reflection matrix at the Fermi level encodes the topological invariant of strong topological insulators [19, 20]. The topology of the reflection matrix changes simultaneously with the appearance of perfect transmission through a finite sample. Therefore, the scattering formalism proves that the changes of the scattering invariant—the invariant determined using the reflection matrix—are accompanied by delocalization transitions in disordered samples. Deep within the localized phase the reflection matrix is unitary and it contains information about the low energy spectrum of the boundary. In a topological system, this probes the anomalous Hamiltonian of the protected surface states. Furthermore, because this approach starts from a real space description of the system, scattering invariants allow to study topological phases in amorphous [21] and quasi-crystalline materials. Finally, determining the reflection matrix is more computationally efficient than obtaining the full spectrum [22], making this approach competitive.

A direct application of the scattering formalism to higher order topological insulators is to consider a finite sample and to attach leads where the zero modes may be located [23, 24, 3]. The scattering invariant computed this way may change whenever transmission between disconnected leads appears, which may happen both when the bulk gap closes and when the surface gap closes. The sensitivity to the surface gap closing makes this approach suitable to probe the topology of the extrinsic HOTIs, but makes its applicability to intrinsic HOTIs unclear. Due to the reliance on the protection by the surface gap, we call the established approach an *extrinsic scattering invariant*, and we demonstrate that it fails when applied to intrinsic HOTIs using the Benalcalázar–Bernevig–Hughes (BBH) model [25] as an example.

We resolve the limitation of the scattering theory of topological invariants and develop its extension to intrinsic HOTIs by defining the *intrinsic scattering invariants*. We demonstrate that our approach correctly classifies the topological phases in a disordered BBH model. We then extend the approach to other second order HOTIs, and answer positively to the question of the existence of a relation between higher order topology and flux response.

4.2. WHY THE EXTRINSIC SCATTERING INVARIANT IS INSUFFICIENT

The most direct approach to applying a scattering invariant to a HOTI is to use the appearance of the protected zero modes on the edge. This requires probing a reflection matrix of a finite symmetric sample with leads attached to its edges in a symmetric way. Symmetry class-dependent functions of the reflection matrix at each lead count the number of protected zero modes at the edge, and their parity was used as a scattering probe for HOTIs [3]. This extrinsic scattering invariant, and similar real space HOTI invariants [26, 27], rely on knowing the position of protected edge states, and therefore they are limited in usefulness for characterizing an unknown system.

To illustrate the limitations of the extrinsic scattering invariant, we consider an example two-dimensional intrinsic HOTI with four-fold rotation anticommuting with sublattice symmetry, known as the BBH model [25]. We construct a circular sample, attach

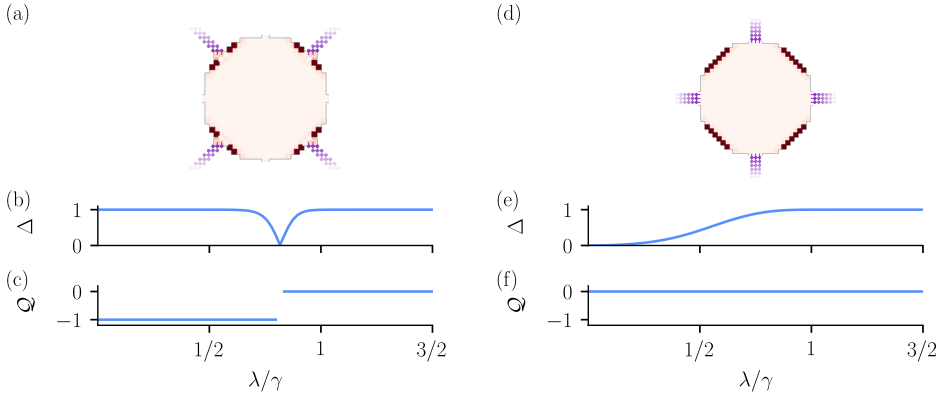


Figure 4.2: Scattering geometries that probe the topology of a two-dimensional intrinsic higher order topological insulator using an extrinsic scattering invariant. Panels (a) and (d) show the local charge density of the zero modes in the scattering region with leads (purple) attached in two different configurations. The gap of the reflection matrix $\Delta = |\det r|$ in (b/e) and the signature of r in (c/f)—the invariant \mathcal{Q} —are sensitive to the location of the leads.

four leads¹ to its edges, and compute the reflection matrix r of a single lead as a function of model parameters. Applying the sublattice symmetry constraint, we transform r to the basis where $r = r^\dagger$. In this basis, the topological invariant \mathcal{Q} is the signature of the reflection matrix [19]—the difference between the number of positive and negative eigenvalues of r .

We characterize the topological transition by additionally computing the gap of the reflection matrix: $\Delta = |\det r|$. This gap is a useful probe of scattering topological invariants because it must vanish simultaneously with the topological invariant changing. Figure 4.2 shows the signature \mathcal{Q} and the reflection gap Δ as a function of λ/γ , with λ the intra-cell hopping and γ the inter-cell hopping of the BBH model. The value $\lambda/\gamma = 1$ corresponds to the topological phase transition of the BBH model [25], which is shifted in a finite sample due to finite-size effects. We observe that the topological invariant strongly depends on the sample geometry. When the leads are attached at the points where the zero modes are located, the invariant changes at the phase transition as expected [Fig. 4.2(a-c)]. On the other hand, if the leads are attached exactly between the zero modes, as shown in Fig. 4.2(e-f), the invariant stays constant across the phase transition.

This failure of the extrinsic scattering invariant to probe the topology of the intrinsic HOTI is a consequence of the invariant being sensitive to the precise location of the zero modes as well as the possibility for the invariant to change without the bulk gap closing. The same limitation likely applies to several other real space probes of HOTI phases, such as localizer invariant [28], multipole winding number [26], mode-shell correspondence [29], and Bott index [30].

¹Throughout the manuscript we use ideal leads, as defined in Ref. [20]

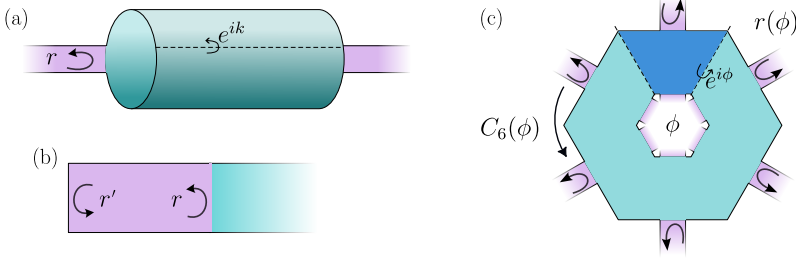


Figure 4.3: Scattering geometries that probe the existence of zero-energy surface states using the bulk symmetries. The reflection matrix r encodes the amplitudes of the wavefunctions that are reflected back into the lead (purple) from the scattering region (turquoise). (a) Scattering setup used to probe topological phases protected by local symmetries. A two-dimensional bulk Hamiltonian defines a one-dimensional reflection matrix by attaching leads along one direction and applying twisted boundary conditions in the other. The reflection matrices r and r' capture the appearance of zero-energy bound states (b). (c) Scattering setup used to probe topological phases protected by spatial symmetries. A two-dimensional six-fold symmetric bulk Hamiltonian defines a one-dimensional reflection matrix by attaching symmetric leads and introducing a flux through the center of the scattering region. The blue area shows the matrix elements of the symmetry operator that gain a phase factor due to the flux, defining $C_6(\phi)$. The scattering setup probes the reflection from the outer lead, which is composed of six disjoint parts related to each other by the rotation symmetry.

4.3. INTRINSIC SCATTERING INVARIANT CONSTRUCTION

The scattering matrix $S(E)$ relates the incoming and outgoing wavefunctions between the leads at an energy E , and its elements are given by the scattering equation:

$$(H - E)(\Psi^{\text{in}} \alpha^{\text{in}} + \Psi^{\text{out}} S(E) \alpha^{\text{in}} + \Psi^{\text{localized}} \alpha^{\text{in}}) = 0, \quad (4.1)$$

where H is the Hamiltonian of the scattering region and the leads, and Ψ^{in} , Ψ^{out} , and $\Psi^{\text{localized}}$ are the wavefunctions of the incoming, outgoing, and localized states, respectively. These wavefunctions are matrices with columns corresponding to different modes, see App. 4.6 for a detailed description. To treat topology due to antisymmetries that map E to $-E$ on the same footing, we set the energy E to zero. The incoming and outgoing wavefunctions occupy the same lead sites and orbitals, while the localized wavefunctions are only defined in the scattering region. The total number of modes is the number of columns of the wavefunction matrices $N_{\text{modes}} = N_{\text{sites}} \times N_{\text{orbitals}}$, where N_{sites} is the number of sites to which the leads are attached, and N_{orbitals} is the number of orbitals per site in the lead. The scattering equations define a valid solution for any combination of amplitudes α^{in} of the incoming modes. Because the scattering matrix in Eq. (4.1) specifies a relation between the amplitudes of the incoming and outgoing wavefunctions, the scattering matrix is a linear map rather than an operator. Separating the leads into two groups imposes a block structure on the scattering matrix:

$$S = \begin{pmatrix} r & t' \\ t & r' \end{pmatrix}, \quad (4.2)$$

where r , r' are reflection matrices, and t , t' are the transmission matrices.

The scattering theory of topological invariants [20] relates the topology of a bulk Hamiltonian $H_{\text{bulk}}(\mathbf{k}_d)$ in a d -dimensional space, with \mathbf{k}_d the wave vector, to the topol-

ogy of a $d - 1$ -dimensional effective Hamiltonian $H_{\text{eff}}(\mathbf{k}_{d-1})$. The dimensional reduction procedure to obtain this effective Hamiltonian is as follows:

1. Construct a large finite sample with the Hamiltonian of the scattering region equal to H_{bulk} .
2. Attach two leads along one of the dimensions and apply twisted periodic boundary conditions along all other dimensions, as shown in Fig. 4.3(a). The phases along each dimension define the new wave vector \mathbf{k}_{d-1} .
3. Compute the reflection matrix $r(\mathbf{k}_{d-1})$ of one of these leads.
4. Choose a proper symmetry representation so that the symmetry constraints on $r(\mathbf{k}_{d-1})$ simplify.
5. Define $H_{\text{eff}}(\mathbf{k}_{d-1})$ using:

$$H_{\text{eff}} = \begin{cases} r = r^\dagger & \text{if } H_{\text{bulk}} \text{ has chiral symmetry,} \\ \begin{pmatrix} 0 & r \\ r^\dagger & 0 \end{pmatrix} & \text{otherwise.} \end{cases} \quad (4.3)$$

This effective Hamiltonian has zero eigenvalues simultaneously with $r(\mathbf{k}_{d-1})$ and a symmetry class different from the symmetry of H_{bulk} . The zero eigenvalues of $r(\mathbf{k}_{d-1})$ correspond to quantized transmission eigenvalues from one lead to the other, which only happens if the gap of H_{bulk} closes. Because of this relation, the topological invariants of H_{eff} and H_{bulk} are equal. An alternative interpretation of the scattering invariant is to consider a boundary between the topological bulk and a trivial region. In this case, the boundary Green's function defines the topology of the bulk [31]. In the scattering description this boundary corresponds to interrupting the lead with a reflection matrix r' of the trivial region, as shown in Fig. 4.3(b). The zero energy modes at an interface of an infinite system appear whenever rr' has an eigenvalue equal to 1, and therefore the protected zero energy solutions at the interface are encoded in r .

While the procedure above may be applied to intrinsic HOTIs, the resulting scattering geometry either has leads swapped by the symmetry of the HOTI, or is incompatible with the global spatial symmetry protecting the HOTI phase. This incompatibility makes the topology of H_{eff} different from the higher order topology of H_{bulk} . Instead, in order to apply the scattering approach to an intrinsic HOTI, the scattering geometry must be compatible with the global spatial symmetry protecting the HOTI phase, and this symmetry must map the leads onto themselves. At the same time, the two leads must be separated by the bulk rather than belonging to the same surface, such that no topological boundary modes propagate between them. This is required in order for zeros of the reflection matrix to correspond to the bulk gap closing and therefore to probe only bulk topological transitions. Otherwise, zeros of the reflection matrix could appear due to the closing of the surface gap and therefore not probe the bulk topology, as illustrated in Sec. 4.2. To satisfy the requirements of the scattering theory we propose to use a finite geometry with a hole: an annulus in two dimensions or a cylinder in three dimensions, and attach one lead to the inside and one lead to the outside of the sample. Figure 4.3(c)

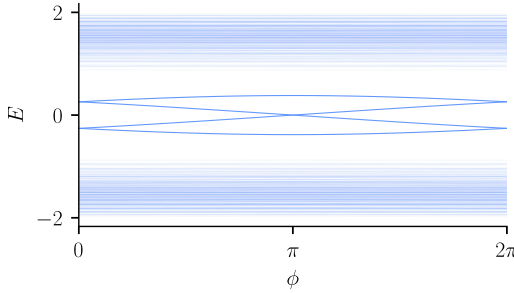


Figure 4.4: Energy spectrum of a topological BBH model in an annulus geometry as a function of the threaded flux ϕ . The transparency of the bands is proportional to the weight of the wavefunctions on the inner ring of the annulus, such that the four states closest to the Fermi level are localized on the inner ring, while the states at the outer ring are not shown. Sublattice symmetry makes the positive and negative energies symmetric, pinning the states crossing to zero energy, but not at any specific value of ϕ —the crossing at $\phi = \pi$ is fine-tuned. The spectral flow of the zero modes is only present in the topological phase. The annulus used for the computation has an inner radius $r_{\text{inner}} = 1$ and an outer radius $r_{\text{outer}} = 10$, $\lambda/\gamma = 0.4$.

shows such a scattering geometry with both the inner and outer leads consisting of several disjoint parts that are related among themselves by the rotating symmetry. Whether the leads are attached to the entire circumference or only a part of it changes the magnitude of the finite size effects, but keeps the topological properties of the scattering geometry the same.

Similar to the dimensional reduction procedure, we apply twisted boundary conditions in the direction parallel to the cylinder axis, which introduces a wave vector k_{d-2} . Without introducing additional parameters, this would result in a $d-2$ -dimensional reflection matrix, which loses information about the angular direction along the cylinder and is unlikely to be sufficient to determine the HOTI topology. To preserve the information about the angular direction, we therefore introduce a flux ϕ through the center of the cylinder, which acts as an additional momentum parameter. The resulting procedure maps a d -dimensional bulk onto a $d-1$ -dimensional $H_{\text{eff}}(\phi, \mathbf{k}_{d-2})$, similar to the dimensional reduction of the strong topological insulators. Contracting the inner radius of the cylinder to a point generally gaps out the surface modes due to finite size effects. Therefore, the flux is also necessary to cancel this splitting, as shown in Fig. 4.4. This cancellation of the finite size splitting was reported in Ref. [32], in a specific symmetry class. By confirming that the scattering invariants work in the annulus geometry, we show that the flux response is a general feature of the higher order topology.

We derive the constraints on the scattering matrix S by considering all the symmetries of the Hamiltonian H and separately applying each of them to the scattering matrix. Applying an operator \mathcal{O} which may be unitary or antiunitary to the scattering equation gives us the transformed scattering equation:

$$\tilde{H}(R_{\mathcal{O}}(\phi, \mathbf{k}_{d-2}))(\mathcal{O}\Psi^{\text{in}}\alpha^{\text{in}} + \mathcal{O}\Psi^{\text{out}}S(\phi, \mathbf{k}_{d-2})\alpha^{\text{in}} + \mathcal{O}\Psi^{\text{localized}}\alpha^{\text{in}}) = 0, \quad (4.4)$$

where $\tilde{H}(R_{\mathcal{O}}(\phi, \mathbf{k}_{d-2})) = \mathcal{O}H(\phi, \mathbf{k}_{d-2})\mathcal{O}^{-1}$ is the transformed Hamiltonian, and $R_{\mathcal{O}}$ is the action of the operator in parameter space, which in general depends on flux and momenta. To obtain the transformed scattering matrix $\tilde{S}(R_{\mathcal{O}}(\phi, \mathbf{k}_{d-2}))$, we act with the

operator on \mathcal{O} on the wavefunctions and coefficients of the wavefunctions, and equate the coefficients of the wavefunctions in Eq. (4.1) and Eq. (4.4) (see App. 4.7 for a detailed derivation). The action of an operator on the lead wavefunctions depends on whether this operator is unitary or antiunitary, and whether it is a symmetry or an antisymmetry of the Hamiltonian. We denote the unitary symmetries \mathcal{U} , unitary antisymmetries \mathcal{C} (chiral symmetry), antiunitary symmetries \mathcal{T} (time-reversal symmetry), and antiunitary antisymmetries \mathcal{P} (particle-hole symmetry). The action of these 4 types of operators on the lead modes is [20]²:

$$\mathcal{U}\Psi^{\text{in}} = \Psi^{\text{in}}V_{\mathcal{U}}(\phi, \mathbf{k}_{d-2}), \quad \mathcal{U}\Psi^{\text{out}} = \Psi^{\text{out}}Q_{\mathcal{U}}(\phi, \mathbf{k}_{d-2}), \quad (4.5a)$$

$$\mathcal{P}\Psi^{\text{in}} = \Psi^{\text{in}}V_{\mathcal{P}}(\phi, \mathbf{k}_{d-2}), \quad \mathcal{P}\Psi^{\text{out}} = \Psi^{\text{out}}Q_{\mathcal{P}}(\phi, \mathbf{k}_{d-2}), \quad (4.5b)$$

$$\mathcal{T}\Psi^{\text{in}} = \Psi^{\text{out}}V_{\mathcal{T}}(\phi, \mathbf{k}_{d-2}), \quad \mathcal{T}\Psi^{\text{out}} = \Psi^{\text{in}}Q_{\mathcal{T}}(\phi, \mathbf{k}_{d-2}), \quad (4.5c)$$

$$\mathcal{C}\Psi^{\text{in}} = \Psi^{\text{out}}V_{\mathcal{C}}(\phi, \mathbf{k}_{d-2}), \quad \mathcal{C}\Psi^{\text{out}} = \Psi^{\text{in}}Q_{\mathcal{C}}(\phi, \mathbf{k}_{d-2}), \quad (4.5d)$$

where $V_{\mathcal{O}}(\phi, \mathbf{k}_{d-2})$ and $Q_{\mathcal{O}}(\phi, \mathbf{k}_{d-2})$ are unitary matrices, which we compute by projecting the operator \mathcal{O} onto the lead wavefunctions. By combining the transformed scattering equation Eq. (4.4) with the transformed wavefunctions in Eqs. (4.5), we obtain the transformed reflection matrix \tilde{r} :

$$\tilde{r}(R_{\mathcal{U}}(\phi, \mathbf{k}_{d-2})) = Q_{\mathcal{U}}(\phi, \mathbf{k}_{d-2})r(\phi, \mathbf{k}_{d-2})V_{\mathcal{U}}^{\dagger}(\phi, \mathbf{k}_{d-2}) \quad (4.6a)$$

$$\tilde{r}(-\phi, -\mathbf{k}_{d-2}) = Q_{\mathcal{P}}(\phi, \mathbf{k}_{d-2})r^*(\phi, \mathbf{k}_{d-2})V_{\mathcal{P}}^{\dagger}(\phi, \mathbf{k}_{d-2}) \quad (4.6b)$$

$$\tilde{r}(-\phi, -\mathbf{k}_{d-2}) = V_{\mathcal{T}}(\phi, \mathbf{k}_{d-2})r^T(\phi, \mathbf{k}_{d-2})Q_{\mathcal{T}}^{\dagger}(\phi, \mathbf{k}_{d-2}) \quad (4.6c)$$

$$\tilde{r}(\phi, \mathbf{k}_{d-2}) = V_{\mathcal{C}}(\phi, \mathbf{k}_{d-2})r^{\dagger}(\phi, \mathbf{k}_{d-2})Q_{\mathcal{C}}^{\dagger}(\phi, \mathbf{k}_{d-2}). \quad (4.6d)$$

If \mathcal{O} is a symmetry, then $\tilde{r} = r$ and Eqs. (4.6) provide symmetry constraints on r .

Due to $r(\phi, \mathbf{k}_{d-2})$ being a linear map (as a submatrix of S), the symmetry operations (4.6) apply to $r(\phi, \mathbf{k}_{d-2})$ differently than to H_{bulk} . Additionally, due to Eq. (4.3), whenever H_{bulk} has chiral symmetry, H_{eff} does not, and vice versa. This results in the Altland–Zirnbauer symmetry class of H_{bulk} being related to that of H_{eff} according to the Bott periodicity [20]. For example, in the symmetry class D ($\mathcal{P}^2 = 1$), particle-hole symmetry constraint is equivalent to $H_{\text{bulk}}(\mathbf{k}) = -H_{\text{bulk}}^*(-\mathbf{k})$ up to a basis choice. The reflection matrix symmetry constraint (4.6b) is then equivalent to $r(-\phi, \mathbf{k}_{d-2}) = r^*(-\phi, -\mathbf{k}_{d-2})$. After applying (4.3), the effective Hamiltonian belongs to the symmetry class BDI ($\mathcal{T}^2 = \mathcal{P}^2 = 1$).

The first step in determining how the spatial unitary symmetries apply to the effective Hamiltonian is to identify the transformation $R_{\mathcal{U}}(\phi, \mathbf{k}_{d-2})$ under the symmetry operator \mathcal{U} . The scattering geometry of Fig. 4.3(c) respects all symmetries that leave the rotation axis invariant. The momenta \mathbf{k}_{d-2} transform as vectors while the flux ϕ transforms as a pseudovector pointing along the rotation axis. Translations and rotations both keep (ϕ, \mathbf{k}_{d-2}) invariant. Inversion symmetry changes the sign of all vector components, while keeping pseudovectors the same:

$$R_{\mathcal{I}}(\phi, \mathbf{k}_{d-2}) = (\phi, -\mathbf{k}_{d-2}). \quad (4.7)$$

²Note that we choose a different convention for V and Q than in Ref. [20]. Swapping $V \leftrightarrow V^T$ and $Q \leftrightarrow Q^T$ would make our convention equivalent to Ref. [20].

Finally, a reflection symmetry M results in

$$R_M(\phi, \mathbf{k}_{d-2}) = (\mp\phi, \pm\mathbf{k}_{d-2}), \quad (4.8a)$$

with the sign depending on whether M commutes or anticommutes with rotation around the axis. The next step requires constructing a symmetry operator in presence of flux ϕ inserted at the rotation axis. We choose a gauge where the flux ϕ enters H_{bulk} as a phase $\exp i\phi$ for all hoppings across a branch cut, as shown in Fig. 4.3(c). Spatial rotations rotate this branch cut by $2\pi/n$, with n the number of rotations needed to do one full rotation, and inversion rotates it by π . Therefore, to keep the Hamiltonian invariant, wavefunctions in the scattering region between the initial and final position of the branch cut acquire a phase $\exp i\phi$, as shown in Fig. 4.3(c). We therefore find that the operator C_n of the rotation by $2\pi/n$ exponentiates to a flux dependent value: $C_n^n(\phi) = C_n^n(0) \exp i\phi$, and accordingly the representations of the rotation symmetry V_{C_n}, Q_{C_n} then satisfy $V_{C_n}^n = C_n^n(0) \exp i\phi$ and $Q_{C_n}^n = C_n^n(0) \exp i\phi$. Similarly, inversion rotates the branch cut by π and squares to $\mathcal{I}^2(\phi) = \mathcal{I}^2(0) \exp i\phi$, so that $V_{\mathcal{I}}^2 = \mathcal{I}^2(0) \exp i\phi$ and $Q_{\mathcal{I}}^2 = \mathcal{I}^2(0) \exp i\phi$. The periodic dependence $r(\phi) = r(\phi + 2\pi)$ invites interpreting ϕ as a momentum of H_{eff} with the Brillouin zone spanned by \mathbf{k}_{d-2} and ϕ . Within this parallel, a C_n rotation symmetry of H_{bulk} which increments the polar angle by $2\pi/n$, results in a translation symmetry by $1/n$ of a unit cell of H_{eff} . Likewise, inversion symmetry results in a combination of reflection with respect to the plane perpendicular to the rotation axis and translation by half a unit cell in H_{eff} . In other words, inversion of the original scattering geometry acts as a glide symmetry on H_{eff} .

Rotations, inversions, and reflections are unitary symmetries, and therefore the symmetry constraints on the reflection matrix $r(\phi, \mathbf{k}_{d-2})$ are given by Eq. (4.6a). More general spatial symmetries, like the $C_4\mathcal{T}$ symmetry that protects the HOTI phase in three dimensions [1], are a combination of a unitary operation with an antiunitary transformation or an antisymmetry. We derive the symmetry constraints on the reflection matrix r by applying the individual operators in the symmetry sequentially, and then combining the results. For example, the $C_4\mathcal{T}$ symmetry is composed of the four-fold rotation C_4 and time-reversal \mathcal{T} operators, under which the reflection matrix r transforms according to Eqs. (4.6a) and (4.6c) respectively. Therefore, the transformation of the reflection matrix under $C_4\mathcal{T}$ is given by the product of the transformations under C_4 and \mathcal{T} :

$$\tilde{r}(-\phi, -\mathbf{k}_{d-2}) = V_{C_4\mathcal{T}}(\phi, \mathbf{k}_{d-2}) r^T(\phi, \mathbf{k}_{d-2}) Q_{C_4\mathcal{T}}^\dagger(\phi, \mathbf{k}_{d-2}), \quad (4.9)$$

where we define $V_{C_4\mathcal{T}} = V_{C_4}(\phi, \mathbf{k}_{d-2}) V_{\mathcal{T}}(\phi, \mathbf{k}_{d-2})$ and $Q_{C_4\mathcal{T}} = Q_{\mathcal{T}}(\phi, \mathbf{k}_{d-2}) Q_{C_4}(\phi, \mathbf{k}_{d-2})$. Once again, if $C_4\mathcal{T}$ is a symmetry, then $\tilde{r} = r$ and the symmetry constraints on r are given by the above equation.

In practice, the first step in determining the topological invariant requires finding a basis for the incoming and outgoing wavefunctions where the symmetry constraints on the reflection matrix are minimal. Choosing an appropriate basis simplifies the time-reversal symmetry constraint to either symmetry or antisymmetry of $r(\phi, \mathbf{k}_{d-2})$, particle-hole symmetry becomes a reality constraint, and chiral symmetry becomes a Hermiticity constraint, as shown in App. 4.7. In the presence of multiple symmetries, we choose the basis where the chiral symmetry gives a Hermiticity constraint if it is present, ac-

ording to Eq. (4.3), and the other symmetries have a minimal compatible form, following Ref. [20]. After performing this transformation, we rely on the established theory of Hamiltonian topological invariants to determine the topological invariant of H_{eff} .

4.4. APPLICATIONS OF THE INTRINSIC SCATTERING INVARIANT

To confirm the universality of the procedure presented in the previous section, we demonstrate how it applies to several important examples of HOTIs. These examples illustrate the ways in which the spatial symmetries of the HOTI phase translate into a symmetry group of the dimensionally reduced Hamiltonian. While we do not aim to provide a complete catalog of scattering invariants for HOTIs, this section presents a strong argument in favor of the universality of the procedure.

4

4.4.1. INTRINSIC SCATTERING INVARIANT OF BBH MODEL

To construct the intrinsic scattering invariant of the BBH model, we first consider the reflection matrix of an annulus-shaped lattice with a flux ϕ and inner and outer leads, as shown in Fig. 4.5(a). In the topological phase, both surfaces of the annulus host four zero-dimensional protected zero modes. Four-fold rotation and sublattice symmetries given by Eqs. (4.6a) and (4.6d) constrain the reflection matrix $r(\phi)$ as

$$r(\phi) = Q_{C_4}(\phi) r(\phi) V_{C_4}^\dagger(\phi) = V_C r^\dagger(\phi) Q_C^\dagger, \quad (4.10)$$

where $V_{C_4}^4(\phi) = Q_{C_4}^4(\phi) = -\exp i\phi$ acquire a phase factor due to the flux ϕ , as explained in Sec. 4.3. Additionally, from $C^2 = 1$ we obtain that $V_C^\dagger = Q_C$. Combining the anticommutation $C_4 C = -C C_4$ with Eqs. (4.5a, 4.5d) additionally yields

$$V_C V_{C_4}(\phi) = -Q_{C_4}(\phi) V_C. \quad (4.11)$$

With all the constraints, we are ready to determine the intrinsic scattering invariant of the BBH model.

As the first step, we simplify the problem by observing that $C_2 \equiv C_4^2$ commutes both with C and C_4 . Because $C_2^2(\phi) = -\exp(i\phi)$, interpreting ϕ as a momentum parameter of the effective Hamiltonian means that the problem is invariant under translation by half a unit cell in the corresponding direction. Therefore, we unfold the Brillouin zone and reduce the unit cell to a primitive one to eliminate redundant degrees of freedom. Because the eigenvalues of C_2 are $\pm i \exp(i\phi/2)$, they are periodic over 4π and the two subspaces of C_2 —and of any operator that commutes with it—swap over a 2π interval. Therefore, we project r and the remaining symmetries onto the subspace of C_2 with the eigenvalue $i \exp i\phi/2$, and consider their dependence on $\phi \in [0, 4\pi)$. The range of $\phi \in [2\pi, 4\pi)$ of the $i \exp i\phi/2$ eigenspace is equivalent to the range $\phi \in [0, 2\pi)$ of the $-i \exp i\phi/2$ eigenspace, so choosing one subspace over twice the interval provides an equivalent representation. To avoid dealing with 4π periodicity, we redefine $\phi := \phi/2$, which yields $r(\phi)$ that satisfies symmetry constraints equivalent to those in Eq. (4.10), but with $V_{C_4}^2 = Q_{C_4}^2 = i \exp i\phi$ instead. We call this procedure factoring out a symmetry, because $r(\phi)$ is no longer constrained by C_2 . We describe how to factor out a symmetry and transform the remaining symmetries to the new basis in App. 4.8.

We proceed simplifying the symmetry constrains by transforming to the eigenbasis of the remaining symmetry operators. We redefine $r(\phi) := V_C^\dagger r(\phi)$ and $V_{C_4}(\phi) = -Q_{C_4}(\phi) := V_C V_{C_4}(\phi)$, and simplify the symmetry constraints to

$$r(\phi) = -V_{C_4}(\phi)r(\phi)V_{C_4}^\dagger(\phi) = r^\dagger(\phi). \quad (4.12)$$

The first equality corresponds to an anticommutation relation, which makes $r(\phi)$ a block-offdiagonal matrix in the basis of V_{C_4} . The second equality establishes that $r(\phi)$ is also Hermitian in this basis. We then transform $r(\phi)$ to the eigenbasis of V_{C_4} , and obtain the effective Hamiltonian

$$H_{\text{eff}}(\phi) = \begin{pmatrix} 0 & h(\phi) \\ h^\dagger(\phi) & 0 \end{pmatrix}, \quad h(\phi + 2\pi) = h^\dagger(\phi), \quad (4.13)$$

where the blocks of $H_{\text{eff}}(\phi)$ are in the basis of the different eigensubspaces of V_{C_4} . The eigensubspaces of V_{C_4} swap under $\phi \rightarrow \phi + 2\pi$, and therefore the effective Hamiltonian in Equation (4.13) is 4π -periodic in ϕ . Contrary to the dimensional reduction procedure used for strong topological insulators, this Hamiltonian has a sublattice-like symmetry—more specifically, a glide sublattice symmetry—just like its parent BBH model. The final step is to apply the topological invariant of $H_{\text{eff}}(\phi)$, however, to the best of our knowledge, the topology of one-dimensional systems combining fractional translations and sublattice symmetries has not been studied before. Therefore, we proceed to construct the invariant, although in most cases one may apply the already established invariants to the effective Hamiltonian.

Because $H_{\text{eff}}(\phi)$ is gapped as long as $h(\phi)$ has no zero eigenvalues, its topological invariant must be a function of $\det h(\phi)$. Because $\det h(\phi + 2\pi) = \det h^*(\phi)$, $\det h(\phi)$ crosses the real axis an odd number of times in the interval $\phi \in [0, 2\pi)$. The \mathbb{Z}_2 invariant of this system is the parity of the number of the crossings by $\det h(\phi)$ of the positive real axis. The crossings of the real axis appear and disappear only in pairs, hence the parity of the number of crossings changes only if $\det h(\phi) = 0$ for some ϕ . Therefore we identify the scattering invariant of the BBH model to be:

$$\mathcal{Q} = \text{sign} \left(\det h(-\pi) \exp \left[\frac{1}{2} \int_{-\pi}^{\pi} d \log \det h(\phi) \right] \right) \in \mathbb{Z}_2. \quad (4.14)$$

Because to compute $h(\phi)$ we project $r(\phi)$ onto the subspaces of C_2 as described in App. 4.8, we require special care to ensure that $H_{\text{eff}}(\phi)$ depends continuously on ϕ . We address this need by computing an eigenvalue decomposition of $V_{C_2}(\phi)$ and $Q_{C_2}(\phi)$ that varies smoothly with ϕ , as described in the App. 4.9. At this point, we have constructed a scattering invariant that uses all of the spatial symmetries of the BBH model, an important difference from extrinsic scattering invariants. Additionally, the invariant requires knowledge of the reflection matrix at all values of $\phi \in [0, 2\pi)$, in agreement with the spectral flow in Fig. 4.4, where the zero-energy crossings of the BBH model are not pinned to any specific value of ϕ .

We construct the model and compute the scattering matrix using Kwant [33]. To demonstrate that the scattering invariant applies to disordered systems, we add a C_4 -symmetric disorder to the BBH model. Specifically, we choose the intra-cell hopping

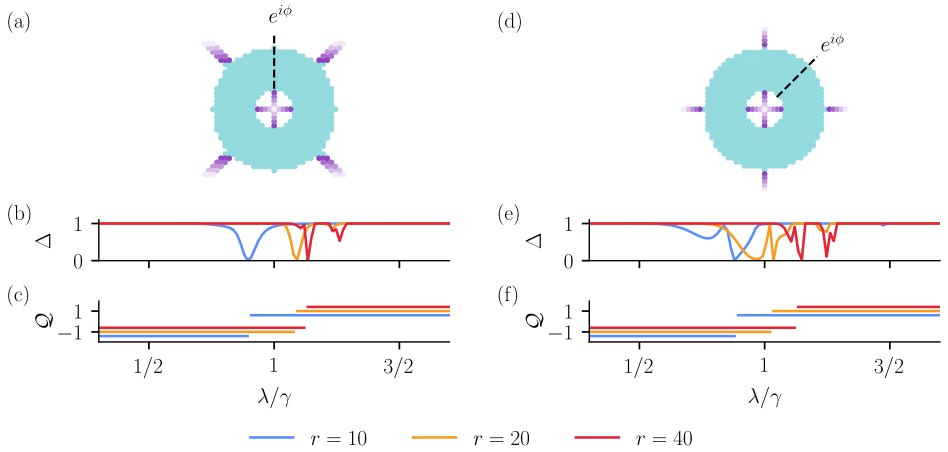


Figure 4.5: Two scattering geometries of the BBH model and their intrinsic invariant in the presence of globally symmetric disorder. (a/d) Annulus geometry with a flux ϕ threaded through the center and leads (purple) attached to the inner and outer rings. In (a) the leads are attached where the zero modes are located and in (d) the leads are in between the zero modes. The gap of the reflection matrix $\Delta = \min |\det r(\phi)|$ in (b/e) closes simultaneously with the sign change of the invariant Q in (c/f). The results are shown for different outer ring sizes $r = 10, 20, 40$, and in (c/f) the values of Q are minimally shifted for clarity.

equal to $\lambda[1 + \delta(x, y)]$, where $\delta(x, y) = \delta(y, -x)$ is symmetric under C_4 rotations, and each $\delta(x, y)$ not related by symmetry is an independent normally distributed random variable with zero mean and standard deviation $1/2$. Enforcing the global symmetry of the disorder distribution is necessary to compute the invariant, because we use the subspaces of the symmetry operator to project the reflection matrix. We present the resulting topological invariant for a single disorder realization in Fig. 4.5. The invariant correctly changes at the phase transition of the BBH model, even when the lead is attached far from the corner charges. Because scattering invariants rely on the unitarity of the reflection matrix, the phase transition point is sensitive to finite-size effects that may arise from the overlap of the wavefunctions between the inner and outer radius of the annulus. Figures 4.5(b-f) show the gap of the reflection matrix $\Delta = \min |\det r(\phi)|$ and the invariant Q as a function of λ/γ for different outer radii r of the annulus. In the thermodynamic limit of $r \rightarrow \infty$ and complete absence of disorder, the invariant changes sign at $\lambda = \gamma$, as expected from the bulk topological invariant of the BBH model. Regardless of the presence of disorder or the size of the annulus, the invariant is always quantized and changes sign only if the reflection matrix has a zero eigenvalue.

4.4.2. SYSTEMS WITH MAGNETIC ROTATION SYMMETRY

A natural application of scattering invariants arises in network models, which provide an efficient way to compute transport properties of large systems. This makes network models a widely used platform to study localization–delocalization transitions in quantum Hall systems [34, 35] and higher-order topological insulators, as done, for example, in Refs. [36, 6, 37, 38]. Topological invariants in network models, however, have an am-

ambiguous topological classification due to the absence of a bulk Hamiltonian. In this section, we demonstrate how the scattering topological invariant resolves the ambiguous topological classification of HOTI network models by considering a two-dimensional $C_4\mathcal{T}$ -symmetric topological superconductor. We use the network model introduced in Ref. [39], where $\mathcal{P}^2 = 1$ and $(C_4\mathcal{T})^4 = -1$, to construct an annulus geometry and, similar to tight-binding models, attach a lead to both the inside and outside of the disk, as shown in Fig. 4.6(a). We construct the scattering geometry and compute the reflection matrix using a network models package [40].

To construct the scattering invariant, we start by factoring out the $C_2 = (C_4\mathcal{T})^2$ symmetry that commutes with the reflection matrix and with all other symmetries. This consists of projecting the reflection matrix onto one of the two eigensubspaces of C_2 and redefining the momentum parameter $\phi := (\phi - \pi)/2$, as described in Sec. 4.4.1 and App. 4.8. After simplifying the symmetry representation, the particle-hole symmetry and the $C_4\mathcal{T}$ symmetry constraints on r become

$$r(\phi) = r^*(-\phi), \quad r(\phi) = -r^T(-\phi) \exp(-i\phi/2), \quad (4.15)$$

making the reflection matrix 4π -periodic. At $\phi = 0$, these constraints define a real anti-symmetric reflection matrix, and therefore the topological invariant is:

$$\mathcal{Q} = \text{sign Pf } H_{\text{eff}}(0) = \text{sign Pf } r(0) \in \mathbb{Z}_2. \quad (4.16)$$

Similar to the BBH model, the spectral flow of the Hamiltonian spectrum of this model has a pair of zero-modes, which appear at $\phi = 0$, and are protected by particle-hole symmetry and a Kramers-like degeneracy originating from the $C_4\mathcal{T}$ symmetry. Figure 4.6(b) shows the phase diagram of the network model as a function of the network parameters. The invariant only changes if the reflection matrix has a zero eigenvalue, and it correctly identifies the HOTI phase of the network model as found in Ref. [39].

Our theory for scattering invariants relies on constructing a symmetric scattering geometry and attaching symmetric leads to both the outside and inside surfaces. We further demonstrate the universality of this procedure by applying it to a three-dimensional $C_4\mathcal{T}$ -symmetric HOTI [41] with protected hinge modes. We consider the model introduced in Ref. [41]:

$$\begin{aligned} H(\mathbf{k}) = & \tau_z \sigma_0 (\cos k_x + \cos k_y + \cos k_z - 3 - \mu) + q_1 \sum_{i=x,y,z} \tau_x \sigma_i \sin k_i \\ & + q_2 \sum_{j=x,y} \tau_y \sigma_j \sin k_j \sin k_z + q_3 \tau_x \sigma_0 + p (\cos k_x - \cos k_y) \tau_y \sigma_0, \end{aligned} \quad (4.17)$$

where σ_i and τ_i are Pauli matrices acting on the spin and orbital degrees of freedom, k_i are the components of the wave vector, q_i and p are strengths of the Hamiltonian terms that break additional symmetries, and μ drives the system through the phase transition. Because the model is three-dimensional, the dimensional reduction procedure results in a two-dimensional effective Hamiltonian for the scattering invariant. Additionally, because $C_4\mathcal{T}$ symmetry rotates the system around the z -axis, we choose to keep k_z and ϕ as the momentum parameters of the effective Hamiltonian, and x and y as the spatial coordinates of the scattering geometry. Therefore, we use a translationally invariant

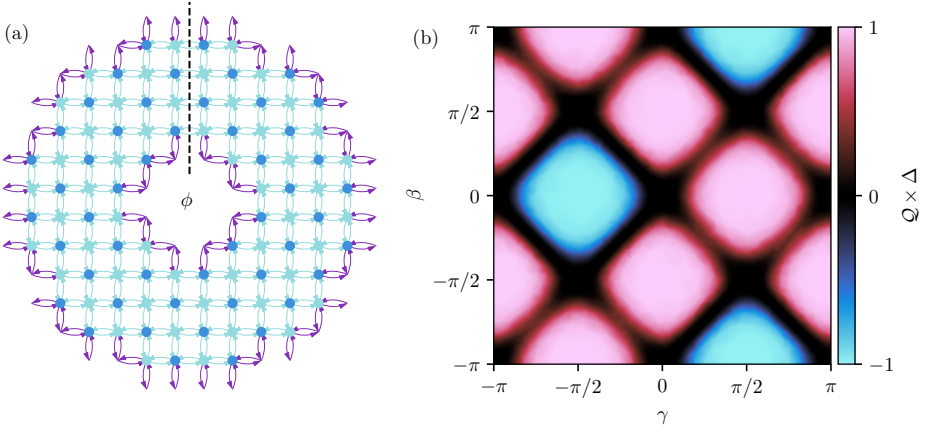


Figure 4.6: Two-dimensional $C_4\mathcal{T} + \mathcal{P}$ -symmetric network model and its corresponding phase diagram. (a) Annulus geometry (blue) with leads (purple) attached to the inside and outside of the disk. The scattering unit cell has two sites and a flux ϕ is threaded through its center. (b) Phase diagram as a function of network parameters β, γ for fixed $\alpha = \pi/2$ and $\delta = 0$.

cylindrical geometry with leads attached to the inside and outside of the cylinder, such that a total of eight hinge modes propagate along the outer and inner surfaces, as shown in Fig. 4.7(a). We construct the scattering geometry and model using Kwant [33] and Qsymm [42].

To construct the scattering invariant, once again we start by factoring out the $C_2 = (C_4\mathcal{T})^2$ symmetry that commutes with the reflection matrix and with all other symmetries, as described in Sec. 4.4.1. We obtain the reflection matrix constraints as:

$$r(\phi, k_z) = -r^T(-\phi, -k_z) \exp(-i\phi/2). \quad (4.18)$$

Differently from the two-dimensional network model example, this model does not have a particle-hole symmetry, and the reflection matrix is not constrained to be real. However, at $\phi = 0$ and $k_z = 0, \pi$, the reflection matrix is still real and antisymmetric. The topological invariant is then the same as that of a two-dimensional class AII topological insulator [20], or if expressed in terms of H_{eff} , it is the invariant of the one-dimensional class DIII topological superconductor [43]:

$$Q = \frac{\text{Pf}[H_{\text{eff}}(0, \pi)]}{\text{Pf}[H_{\text{eff}}(0, 0)]} \exp \left[-\frac{1}{2} \int_0^\pi d \log \det H_{\text{eff}}(0, k_z) \right] \in \mathbb{Z}_2, \quad (4.19)$$

where $H_{\text{eff}}(0, k_z) = r(0, k_z)$. The resulting phase diagram is shown in Fig. 4.7(b-c).

We observe that both in the two-dimensional and three-dimensional cases, the topological invariant is determined by the reflection matrix at $\phi = 0$. This is similar to an earlier work on antiferromagnetic topological insulators [44]. Such behavior occurs whenever an antiunitary symmetry is multiplied by a fractional translation, which makes the square of the symmetry operator change between different high symmetry lines in the

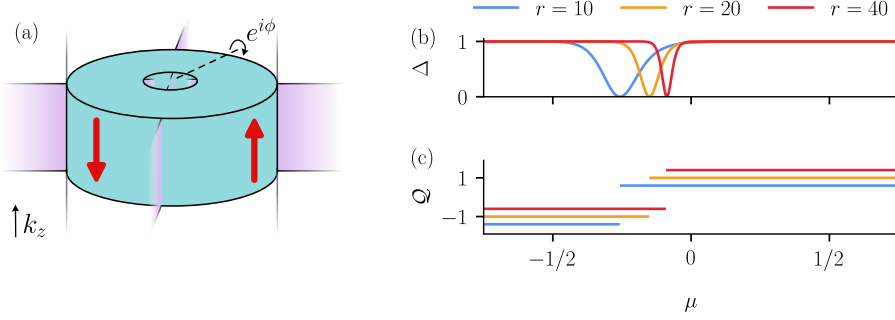


Figure 4.7: Three-dimensional $C_4\mathcal{T}$ -symmetric HOTI. (a) Infinite cylindrical scattering geometry with a flux ϕ threaded through the center. The leads (purple) are attached to the inside and outside of the cylinder, both are surfaces with four edge modes (red). (b) Gap of the reflection matrix $\Delta = \min |\det r(\phi, k_z)|$ and (c) invariant Q as a function of the onsite potential μ . For this computation we use $q_1 = 1$ and $q_2 = q_3 = p = 0.1$.

Brillouin zone. In our construction, the same principle applies to fractional rotations. Thanks to this observation, we also conclude that the topological classification of systems with magnetic rotation exponentiating to $+1$ is identical, except that the relevant value of ϕ shifts in the reduced Brillouin zone.

4.4.3. AXION INSULATOR: 3D INVERSION

Finally, in this section, we demonstrate how to apply the scattering invariant to point-group symmetries, which lack a preferred direction for the leads or boundary modes. As an example, we consider a three-dimensional axion insulator [45, 46, 47], which is a second-order HOTI protected by inversion symmetry. A finite axion insulator sample hosts a chiral mode that encircles the entire sample [48], as shown in Fig. 4.8(a). Inversion symmetry forbids the chiral mode from being contracted to a point, but it does not constrain its position on the surface.

We construct a minimal model of an axion insulator with the following Hamiltonian:

$$H = -\mu\tau_z\sigma_0 + \sum_{i=x,y,z} 2(1 - \cos k_i)\tau_z\sigma_0 + \alpha \sum_{i=x,y,z} \sin k_i\sigma_i\tau_x + \mathbf{B}\tau_0\boldsymbol{\sigma}. \quad (4.20)$$

Here σ_i and τ_i are Pauli matrices acting on the spin and orbital degrees of freedom, and k_i are the components of the wave vector. The Hamiltonian parameter α is the spin-orbit coupling strength, \mathbf{B} is a magnetic field, which we use to break time-reversal symmetry, and μ is the chemical potential. This model is trivial for $\mu < 0$ and topological for $\mu > 0$. Because the HOTI is protected by inversion symmetry, we construct an inversion-symmetric scattering geometry for applying the scattering invariant. Such a geometry is a translationally-invariant cylinder where k_z and ϕ are the momentum parameters of the effective Hamiltonian, and x and y are the spatial coordinates of the scattering geometry.

Inversion symmetry maps $k_z \rightarrow -k_z$ and $\phi \rightarrow \phi$, and constrains the reflection matrix $r(\phi, k_z)$ as:

$$V_{\mathcal{I}}(\phi)r(\phi, k_z)Q_{\mathcal{I}}^{\dagger}(\phi) = r(\phi, -k_z), \quad V_{\mathcal{I}}^2(\phi) = Q_{\mathcal{I}}^2(\phi) = e^{-i\phi}. \quad (4.21)$$

This follows from Eqs. (4.5a) and (4.21), and becomes a commutation relation for $k_z =$

$0, \pi$. The equivalent H_{eff} (4.3) is two-dimensional, and it has a combination of a glide symmetry and a sublattice symmetry. This topological phase was analyzed in Ref. [49], and its topological invariant relies on block-diagonalizing the reflection matrix by projecting it onto the eigenbasis of $V_{\mathcal{I}}(\phi)$ and $Q_{\mathcal{I}}(\phi)$ at $k_z = 0$ and $k_z = \pi$. The scattering invariant is:

$$\mathcal{Q} = \text{sign} \left[\frac{\det r_+(-\pi, 0) \exp \frac{1}{2} \int_{-\pi}^{\pi} d\phi \ln \det r_+(\phi, 0)}{\det r_+(-\pi, \pi) \exp \frac{1}{2} \int_{-\pi}^{\pi} d\phi \ln \det r_+(\phi, \pi)} \exp \frac{1}{2} \int_0^{\pi} dk_z \ln \det r(-\pi, k_z) \right], \quad (4.22)$$

where $r_+(\phi, k_z)$ is the reflection matrix projected onto the subspace of $V_{\mathcal{I}}(\phi)$ and $Q_{\mathcal{I}}(\phi)$ with eigenvalue $e^{i\phi/2}$. Its graphical representation is shown in Fig. 4.8(b), and we identify the numerator and denominator of the fraction as the way of defining $\sqrt{\det r(-\pi, 0)}$ and $\sqrt{\det r(-\pi, \pi)}$ without the sign ambiguity. Similar to Sec. 4.4.1, we apply the procedure of App. 4.9 to ensure that the integrands are smooth functions of ϕ . By applying the invariant to the scattering matrix of our example system, we confirm that the invariant switches at the phase transition, as shown in Fig. 4.8(c-d). Fig. 4.8(d) shows an extended range of μ where the invariant flips sign due to the Fermi surface that appears for such values of μ .

Scattering invariants are a powerful tool to study localization–delocalization transitions in disordered systems because they establish a direct connection between topology and transport properties. Reference [6], for example, studied the effect of the bulk delocalization transition of disordered axion insulators using a network model, and claimed that an earlier analysis [50, 51] of topological phases protected by an average symmetry does not extend to HOTIs. Our scattering invariant, however, allows us to formulate a proof of the existence of the delocalized phase in a disordered axion insulator along the lines of Ref. [50]. We do this by considering a finite but large cylindrical sample with disorder in one half being an inversion image of the disorder in the other half, such that locally disorder breaks inversion symmetry, but globally the system is inversion symmetric. Because the scattering invariant must change across the phase transition, a mode must perfectly transmit between the inner and outer radius of the cylinder as a phase transition is crossed. Additionally, because the system is three-dimensional, this implies that the perfectly transmitted mode is accompanied by a metallic phase. This argument establishes that the axion insulator must have a delocalized phase in the presence of disorder that is symmetric on average.

4.5. CONCLUSION AND DISCUSSION

We presented a general construction of scattering invariants for second order intrinsic higher order topological insulators and superconductors. To do so, we established a general procedure that relies on the compatibility of the spatial symmetries that protect a HOTI with the geometry of the scattering region. Determining the topological invariant required us to consider a geometry with separated inside and outside regions, and to consider the flux dependence of the reflection matrix. Similar to the dimensional reduction procedure for strong topological insulators [20], from a given model we constructed a lower-dimensional effective Hamiltonian in a different symmetry class, and used the topological invariant of this effective Hamiltonian to determine the topological phase of the original model. Differently from the standard scattering theory of topological in-

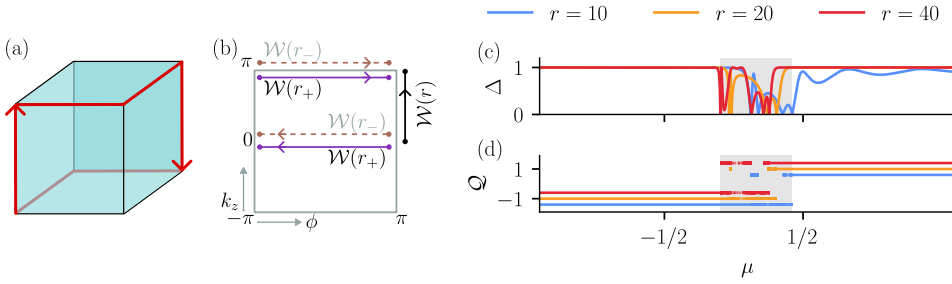


Figure 4.8: A three-dimensional inversion-symmetric second-order HOTI, the axion insulator. (a) Finite geometry in the HOTI phase with a protected edge mode (red) encircling the entire sample. (b) Brillouin zone of the effective Hamiltonian H_{eff} with the path and windings \mathcal{W} of the invariant calculation. (c) Gap of the reflection matrix $\Delta = \min |\det r(\phi, k_z)|$. (d) Scattering invariant \mathcal{Q} as a function of the chemical potential μ . The extended range of μ (gray) for which the sign of the invariant changes is due to the Fermi surface.

sulators, our procedure maps a rotation symmetry on a translation symmetry, and an inversion symmetry on a glide symmetry.

We have applied the procedure to several prominent examples:

- The BBH model, a 2D HOTI protected by anticommuting C_4 and \mathcal{C} symmetries.
- A 2D HOTI with a $C_4\mathcal{T}$ and \mathcal{P} symmetry, for which we used a network model demonstration.
- A 3D HOTI with $C_4\mathcal{T}$ symmetry.
- A 3D axion insulator with inversion symmetry.

In all cases, the scattering invariant correctly identified the topological phase transitions regardless of the detailed geometry of the scattering region. The topological invariants that we used employ reasoning previously identified for antiferromagnetic topological insulators [44] or for topological crystalline insulators [49]. Additionally, our approach enables us to factor out a pure rotation that commutes with the other symmetries, while the Hamiltonian approach [41] requires special treatment of such symmetries.

Our examples, together with general arguments, indicate that our approach applies to all the second order HOTIs. On the other hand, higher order HOTIs, in particular three-dimensional phases with zero-dimensional protected modes, do not seem to fit into our framework. This is because one can choose the cylinder geometry so that the corner modes do not appear on its inner or outer boundary. We expect that the need for holes with a flux in the scattering geometry extends to higher order HOTIs. More specifically, we conjecture that third order HOTIs need a scattering geometry with two holes and two fluxes ϕ_i threaded through them, in such a way that the dimensional reduction procedure maps to a $d-1$ -dimensional $H_{\text{eff}}(\phi_1, \phi_2, \mathbf{k}_{d-3})$. The finite size gap of the surface states at the boundaries then goes to zero as a function of the fluxes introduced.

Finally, our work reveals a different perspective on higher order topological insulators from those presented in the literature. We have found that a nontrivial reflection matrix always corresponds to the appearance of a zero energy mode in the original model's

rectangular matrix with ones in the diagonal and zeros everywhere else. Reference [22] contains a detailed review of the scattering matrix formalism.

The scattering matrix $S(E)$ relates the incoming and outgoing wavefunctions between the leads at an energy E , and its elements are given by the scattering equations:

$$(H_{ab} - E\delta_{ab})(\Psi_{bn}^{\text{in}}\alpha_n^{\text{in}} + \sum_m \Psi_{bm}^{\text{out}}S_{mn}\alpha_n^{\text{in}} + \Psi_{bn}^{\text{localized}}\alpha_n^{\text{in}}) = 0, \quad (4.24)$$

where H_{ab} is the Hamiltonian, and a and b label the sites and orbital degrees of freedom of the scattering region and the leads. The incoming and outgoing wavefunctions Ψ^{in} and Ψ^{out} are finite in the leads and vanish in the scattering region, while the localized wavefunctions $\Psi^{\text{localized}}$ are defined in the scattering region and may decay exponentially into the leads if evanescent modes are present. The wavefunctions are matrices where each column corresponds to a mode, and the rows label the sites and orbitals matching the size of the Hamiltonian. The total number of modes is $N_{\text{modes}} = N_{\text{sites}} \times N_{\text{orbitals}}$ for ideal leads, i.e., leads that do not host any evanescent modes, where N_{sites} is the number of sites from which the leads are attached, and N_{orbitals} is the number of orbitals per site in the lead. The scalars α_n^{in} are the amplitudes of each incoming mode n . Because the leads are translational-invariant, the leads modes are plane waves and we solve Eq. (4.24) using a sparse finite system of equations [22].

In the context of scattering topological invariants, we are interested in the topology of the scattering region. Therefore, H_{sr} is a HOTI Hamiltonian that preserves the symmetries of interest, while H_{lead} only needs to globally preserve the symmetries. In practice, we create either a tight-binding model of the scattering region or a network model. We make the tight-binding model of a scattering region using the Kwant package [33] and test the symmetries of the Hamiltonian using Qsymm [42]. Additionally, we construct ideal leads using Kwant, see Ref. [54] for the code. A network model, such as we used for the 2D $C_4\mathcal{T} + \mathcal{P}$ symmetric system in section 4.4.2 consists of a combination of scattering matrices, each as a node within the network. The links in between the nodes connect the different scattering regions and the leads are once again plane waves to the scattering regions.

4.7. SYMMETRY CONSTRAINTS ON SCATTERING MATRICES

In this section, we derive the constraints on the reflection matrix r imposed by a symmetry operator \mathcal{O} . In general, applying an operator \mathcal{O} to the scattering equation in Eq. (4.1) at $E = 0$ gives:

$$\tilde{H}(R_{\mathcal{O}}(\phi, \mathbf{k}_{d-2}))(\mathcal{O}\Psi^{\text{in}}\alpha^{\text{in}} + \mathcal{O}\Psi^{\text{out}}S(\phi, \mathbf{k}_{d-2})\alpha^{\text{in}} + \mathcal{O}\Psi^{\text{localized}}\alpha^{\text{in}}) = 0, \quad (4.25)$$

where $\tilde{H}(R_{\mathcal{O}}(\phi, \mathbf{k}_{d-2})) = \mathcal{O}H(\phi, \mathbf{k}_{d-2})\mathcal{O}^{-1}$ is the transformed Hamiltonian, and $R_{\mathcal{O}}$ is the action of the operator in parameter space. If the operator \mathcal{O} is a symmetry of the Hamiltonian, Eq. (4.25) constrains the scattering matrix S and the reflection matrix r . To derive the constraints on r , we equate the coefficients of the wavefunctions in the scattering equations to the ones in the symmetry-transformed scattering equations. Therefore, we start by applying \mathcal{O} to the incoming and outgoing wavefunctions. Because \mathcal{O} may be a unitary or antiunitary operator, and a symmetry or antisymmetry, we consider four cases.

4.7.1. UNITARY SYMMETRY

Unitary symmetries map incoming and outgoing wavefunctions within the same Hilbert space:

$$\mathcal{O}\Psi^{\text{in}} = \Psi^{\text{in}}V_{\mathcal{O}}(\phi, \mathbf{k}_{d-2}), \quad \mathcal{O}\Psi^{\text{out}} = \Psi^{\text{out}}Q_{\mathcal{O}}(\phi, \mathbf{k}_{d-2}), \quad (4.26)$$

where $V_{\mathcal{O}}$ and $Q_{\mathcal{O}}$ are matrices that act on the wavefunctions. Applying \mathcal{O} to the wavefunctions twice gives:

$$\begin{aligned} \mathcal{O}(\mathcal{O}\Psi^{\text{in}}) &= \mathcal{O}(\Psi^{\text{in}}V_{\mathcal{O}}) = \Psi^{\text{in}}V_{\mathcal{O}}^2(\phi, \mathbf{k}_{d-2}) \\ \mathcal{O}(\mathcal{O}\Psi^{\text{out}}) &= \mathcal{O}(\Psi^{\text{out}}Q_{\mathcal{O}}) = \Psi^{\text{out}}Q_{\mathcal{O}}^2(\phi, \mathbf{k}_{d-2}). \end{aligned} \quad (4.27)$$

As a consequence, we obtain the following constraint:

$$\begin{aligned} (\Psi^{\text{in}})^{\dagger}\mathcal{O}^2\Psi^{\text{in}} &= V_{\mathcal{O}}^2(\phi, \mathbf{k}_{d-2}), \\ (\Psi^{\text{out}})^{\dagger}\mathcal{O}^2\Psi^{\text{out}} &= Q_{\mathcal{O}}^2(\phi, \mathbf{k}_{d-2}), \end{aligned} \quad (4.28)$$

if \mathcal{O} is a unitary symmetry.

Finally, we combine Eqs. (4.26) and (4.25):

$$\begin{aligned} \tilde{H}(R_{\mathcal{O}}(\phi, \mathbf{k}_{d-2}))(\Psi^{\text{in}}V_{\mathcal{O}}(\phi, \mathbf{k}_{d-2})\alpha^{\text{in}} + \Psi^{\text{out}}Q_{\mathcal{O}}(\phi, \mathbf{k}_{d-2})S(\phi, \mathbf{k}_{d-2})\alpha^{\text{in}} + \Psi^{\text{localized}}\alpha^{\text{in}}) &= 0, \\ \Rightarrow \tilde{H}(R_{\mathcal{O}}(\phi, \mathbf{k}_{d-2}))(\Psi^{\text{in}}\alpha^{\text{in}'} + \Psi^{\text{out}}Q_{\mathcal{O}}(\phi, \mathbf{k}_{d-2})S(\phi, \mathbf{k}_{d-2})V_{\mathcal{O}}^{\dagger}(\phi, \mathbf{k}_{d-2})\alpha^{\text{in}'} + \Psi^{\text{localized}}\alpha^{\text{in}}) &= 0. \end{aligned} \quad (4.29)$$

where we identified $\alpha^{\text{in}'} = V_{\mathcal{O}}(\phi, \mathbf{k}_{d-2})\alpha^{\text{in}}$. Because \mathcal{O} is a symmetry, the solutions of Eq. (4.29) are those of Eq. (4.1) for $S(R_{\mathcal{O}}(\phi, \mathbf{k}_{d-2}))$. Therefore, the scattering matrix S is constrained by the symmetry operator \mathcal{O} as:

$$Q_{\mathcal{O}}(\phi, \mathbf{k}_{d-2})S(\phi, \mathbf{k}_{d-2})V_{\mathcal{O}}^{\dagger}(\phi, \mathbf{k}_{d-2}) = S(R_{\mathcal{O}}(\phi, \mathbf{k}_{d-2})). \quad (4.30)$$

4.7.2. ANTIUNITARY ANTISYMMETRY

Antiunitary antisymmetries map incoming and outgoing wavefunctions within the same Hilbert space, like unitary symmetries:

$$\mathcal{O}\Psi^{\text{in}} = \Psi^{\text{in}}V_{\mathcal{O}}(\phi, \mathbf{k}_{d-2}), \quad \mathcal{O}\Psi^{\text{out}} = \Psi^{\text{out}}Q_{\mathcal{O}}(\phi, \mathbf{k}_{d-2}), \quad (4.31)$$

where $V_{\mathcal{O}}$ and $Q_{\mathcal{O}}$ are matrices that act on the wavefunctions. Applying \mathcal{O} to the wavefunctions twice gives:

$$\begin{aligned} \mathcal{O}(\mathcal{O}\Psi^{\text{in}}) &= \mathcal{O}(\Psi^{\text{in}}V_{\mathcal{O}}) = \Psi^{\text{in}}V_{\mathcal{O}}(\phi, \mathbf{k}_{d-2})V_{\mathcal{O}}^*(\phi, \mathbf{k}_{d-2}) \\ \mathcal{O}(\mathcal{O}\Psi^{\text{out}}) &= \mathcal{O}(\Psi^{\text{out}}Q_{\mathcal{O}}) = \Psi^{\text{out}}Q_{\mathcal{O}}(\phi, \mathbf{k}_{d-2})Q_{\mathcal{O}}^*(\phi, \mathbf{k}_{d-2}), \end{aligned} \quad (4.32)$$

where we applied the conjugate operator \mathcal{K} to the matrices $V_{\mathcal{O}}$ and $Q_{\mathcal{O}}$. As a consequence, we obtain the following constraint:

$$\begin{aligned} (\Psi^{\text{in}})^{\dagger}\mathcal{O}^2\Psi^{\text{in}} &= V_{\mathcal{O}}(\phi, \mathbf{k}_{d-2})V_{\mathcal{O}}^*(\phi, \mathbf{k}_{d-2}) \\ (\Psi^{\text{out}})^{\dagger}\mathcal{O}^2\Psi^{\text{out}} &= Q_{\mathcal{O}}(\phi, \mathbf{k}_{d-2})Q_{\mathcal{O}}^*(\phi, \mathbf{k}_{d-2}), \end{aligned} \quad (4.33)$$

if \mathcal{O} is an antiunitary antisymmetry.

Finally, we combine Eqs. (4.31) and (4.25):

$$\begin{aligned} \tilde{H}(R_{\mathcal{O}}(\phi, \mathbf{k}_{d-2}))(\Psi^{\text{in}} V_{\mathcal{O}}(\phi, \mathbf{k}_{d-2}) \alpha^{\text{in}*} + \Psi^{\text{out}} Q_{\mathcal{O}}(\phi, \mathbf{k}_{d-2}) S^*(\phi, \mathbf{k}_{d-2}) \alpha^{\text{in}*} + \Psi^{\text{localized}} \alpha^{\text{in}*}) &= 0, \\ \Rightarrow \tilde{H}(R_{\mathcal{O}}(\phi, \mathbf{k}_{d-2}))(\Psi^{\text{in}} \alpha^{\text{in}'} + \Psi^{\text{out}} Q_{\mathcal{O}}(\phi, \mathbf{k}_{d-2}) S^*(\phi, \mathbf{k}_{d-2}) V_{\mathcal{O}}^{\dagger}(\phi, \mathbf{k}_{d-2}) \alpha^{\text{in}'} + \Psi^{\text{localized}} \alpha^{\text{in}}) &= 0. \end{aligned} \quad (4.34)$$

where we identified $\alpha^{\text{in}'} = V_{\mathcal{O}}(\phi, \mathbf{k}_{d-2}) \alpha^{\text{in}*}$. Because \mathcal{O} is a symmetry, the solutions of Eq. (4.34) are those of Eq. (4.1) for $S(R_{\mathcal{O}}(\phi, \mathbf{k}_{d-2}))$. Therefore, the scattering matrix S is constrained by the symmetry operator \mathcal{O} as:

$$Q_{\mathcal{O}}(\phi, \mathbf{k}_{d-2}) S^*(\phi, \mathbf{k}_{d-2}) V_{\mathcal{O}}^{\dagger}(\phi, \mathbf{k}_{d-2}) = S(R_{\mathcal{O}}(\phi, \mathbf{k}_{d-2})). \quad (4.35)$$

For example, in the presence of particle-hole symmetry Eq. (4.35) establishes that S is isomorphic to a real matrix S' at time-reversal invariant momenta if $\mathcal{P}^2 = 1$. To see this, we use that $V_{\mathcal{P}} V_{\mathcal{P}}^* = Q_{\mathcal{P}} Q_{\mathcal{P}}^* = \mathcal{P}^2 = \pm 1$ to manipulate Eq.(4.35) and obtain

$$\left(\sqrt{Q_{\mathcal{P}}(\phi, \mathbf{k}_{d-2})}^* S(\phi, \mathbf{k}_{d-2}) \sqrt{V_{\mathcal{P}}(\phi, \mathbf{k}_{d-2})}^T \right)^* = \pm \sqrt{Q_{\mathcal{P}}(\phi, \mathbf{k}_{d-2})}^* S(-\phi, -\mathbf{k}_{d-2}) \sqrt{V_{\mathcal{P}}(\phi, \mathbf{k}_{d-2})}^T, \quad (4.36)$$

where $\sqrt{Q_{\mathcal{P}}}$ and $\sqrt{V_{\mathcal{P}}}$ denote the square root of the matrix. At time-reversal invariant momenta we define $S' = \sqrt{Q_{\mathcal{P}}}^* S \sqrt{V_{\mathcal{P}}}^T$ and find $S' = S'^*$ for $\mathcal{P}^2 = 1$, and $S' = \sigma_y S'^* \sigma_y$ for $\mathcal{P}^2 = -1$. The σ_y operator is required to satisfy $\sqrt{Q_{\mathcal{P}}} \sqrt{Q_{\mathcal{P}}}^* = \sqrt{V_{\mathcal{P}}} \sqrt{V_{\mathcal{P}}}^* = -1$. This constraint may be incompatible with other constraints if multiple symmetries are present.

4.7.3. UNITARY ANTISYMMETRY

Unitary antisymmetries map incoming and outgoing wavefunctions to each other:

$$\mathcal{O} \Psi^{\text{in}} = \Psi^{\text{out}} V_{\mathcal{O}}(\phi, \mathbf{k}_{d-2}), \quad \mathcal{O} \Psi^{\text{out}} = \Psi^{\text{in}} Q_{\mathcal{O}}(\phi, \mathbf{k}_{d-2}), \quad (4.37)$$

where $V_{\mathcal{O}}$ and $Q_{\mathcal{O}}$ are matrices that act on the wavefunctions. Applying \mathcal{O} to the wavefunctions twice gives:

$$\begin{aligned} \mathcal{O}(\mathcal{O} \Psi^{\text{in}}) &= \mathcal{O}(\Psi^{\text{out}} V_{\mathcal{O}}) = \Psi^{\text{in}} Q_{\mathcal{O}}(\phi, \mathbf{k}_{d-2}) V_{\mathcal{O}}(\phi, \mathbf{k}_{d-2}) \\ \mathcal{O}(\mathcal{O} \Psi^{\text{out}}) &= \mathcal{O}(\Psi^{\text{in}} Q_{\mathcal{O}}) = \Psi^{\text{out}} V_{\mathcal{O}}(\phi, \mathbf{k}_{d-2}) Q_{\mathcal{O}}(\phi, \mathbf{k}_{d-2}), \end{aligned} \quad (4.38)$$

where we applied the conjugate operator \mathcal{K} to the matrices $V_{\mathcal{O}}$ and $Q_{\mathcal{O}}$. As a consequence, we obtain the following constraint:

$$\begin{aligned} (\Psi^{\text{in}})^{\dagger} \mathcal{O}^2 \Psi^{\text{in}} &= Q_{\mathcal{O}}(\phi, \mathbf{k}_{d-2}) V_{\mathcal{O}}(\phi, \mathbf{k}_{d-2}) \\ (\Psi^{\text{out}})^{\dagger} \mathcal{O}^2 \Psi^{\text{out}} &= V_{\mathcal{O}}(\phi, \mathbf{k}_{d-2}) Q_{\mathcal{O}}(\phi, \mathbf{k}_{d-2}) \end{aligned} \quad (4.39)$$

if \mathcal{O} is a unitary antisymmetry.

Finally, we combine Eqs. (4.37) and (4.25):

$$\begin{aligned} \tilde{H}(R_{\mathcal{O}}(\phi, \mathbf{k}_{d-2}))(\Psi^{\text{out}} V_{\mathcal{O}}(\phi, \mathbf{k}_{d-2}) \alpha^{\text{in}} + \Psi^{\text{in}} Q_{\mathcal{O}}(\phi, \mathbf{k}_{d-2}) S(\phi, \mathbf{k}_{d-2}) \alpha^{\text{in}} + \Psi^{\text{localized}} \alpha^{\text{in}}) &= 0, \\ \Rightarrow \tilde{H}(R_{\mathcal{O}}(\phi, \mathbf{k}_{d-2}))(\Psi^{\text{in}} \alpha^{\text{in}'} + \Psi^{\text{out}} V_{\mathcal{O}}(\phi, \mathbf{k}_{d-2}) S^{\dagger}(\phi, \mathbf{k}_{d-2}) Q_{\mathcal{O}}^{\dagger}(\phi, \mathbf{k}_{d-2}) \alpha^{\text{in}'} + \Psi^{\text{localized}} \alpha^{\text{in}}) &= 0. \end{aligned} \quad (4.40)$$

where we identified $\alpha^{\text{in}'} = Q_{\mathcal{O}}(\phi, \mathbf{k}_{d-2})S(\phi, \mathbf{k}_{d-2})\alpha^{\text{in}}$. Because \mathcal{O} is a symmetry, the solutions of Eq. (4.40) are those of Eq. (4.1) for $S(R_{\mathcal{O}}(\phi, \mathbf{k}_{d-2}))$. Therefore, the scattering matrix S is constrained by the symmetry operator \mathcal{O} as:

$$V_{\mathcal{O}}(\phi, \mathbf{k}_{d-2})S^{\dagger}(\phi, \mathbf{k}_{d-2})Q_{\mathcal{O}}^{\dagger}(\phi, \mathbf{k}_{d-2}) = S(R_{\mathcal{O}}(\phi, \mathbf{k}_{d-2})). \quad (4.41)$$

For example, in the presence of chiral symmetry Eq. (4.41) establishes that S is isomorphic to a Hermitian matrix S' . To find the transformation that makes S Hermitian, we first observe that $Q_{\mathcal{C}}V_{\mathcal{C}} = V_{\mathcal{C}}Q_{\mathcal{C}} = \mathcal{C}^2 = 1$ from Eq. (4.39). Then, we use $Q_{\mathcal{C}}^{\dagger} = V_{\mathcal{C}}$ in Eq. (4.41) and find $S' = S'^{\dagger}$ for $S'(\phi, \mathbf{k}_{d-2}) = V_{\mathcal{C}}^{\dagger}(\phi, \mathbf{k}_{d-2})S(\phi, \mathbf{k}_{d-2})$.

4.7.4. ANTIUNITARY SYMMETRY

Antiunitary symmetries map incoming and outgoing wavefunctions to each other:

$$\mathcal{O}\Psi^{\text{in}} = \Psi^{\text{out}}V_{\mathcal{O}}(\phi, \mathbf{k}_{d-2}), \quad \mathcal{O}\Psi^{\text{out}} = \Psi^{\text{in}}Q_{\mathcal{O}}(\phi, \mathbf{k}_{d-2}), \quad (4.42)$$

where $V_{\mathcal{O}}$ and $Q_{\mathcal{O}}$ are matrices that act on the wavefunctions. Applying \mathcal{O} to the wavefunctions twice gives:

$$\begin{aligned} \mathcal{O}(\mathcal{O}\Psi^{\text{in}}) &= \mathcal{O}(\Psi^{\text{out}}V_{\mathcal{O}}) = \Psi^{\text{in}}Q_{\mathcal{O}}(\phi, \mathbf{k}_{d-2})V_{\mathcal{O}}^*(\phi, \mathbf{k}_{d-2}) \\ \mathcal{O}(\mathcal{O}\Psi^{\text{out}}) &= \mathcal{O}(\Psi^{\text{in}}Q_{\mathcal{O}}) = \Psi^{\text{out}}V_{\mathcal{O}}(\phi, \mathbf{k}_{d-2})Q_{\mathcal{O}}^*(\phi, \mathbf{k}_{d-2}), \end{aligned} \quad (4.43)$$

where we applied the conjugate operator \mathcal{K} to the matrices $V_{\mathcal{O}}$ and $Q_{\mathcal{O}}$. As a consequence, we obtain the following constraint:

$$\begin{aligned} (\Psi^{\text{in}})^{\dagger}\mathcal{O}^2\Psi^{\text{in}} &= Q_{\mathcal{O}}(\phi, \mathbf{k}_{d-2})V_{\mathcal{O}}^*(\phi, \mathbf{k}_{d-2}), \\ (\Psi^{\text{out}})^{\dagger}\mathcal{O}^2\Psi^{\text{out}} &= V_{\mathcal{O}}(\phi, \mathbf{k}_{d-2})Q_{\mathcal{O}}^*(\phi, \mathbf{k}_{d-2}) \end{aligned} \quad (4.44)$$

if \mathcal{O} is an antiunitary symmetry.

Finally, we combine Eqs. (4.42) and (4.25):

$$\begin{aligned} \tilde{H}(R_{\mathcal{O}}(\phi, \mathbf{k}_{d-2}))(\Psi^{\text{out}}V_{\mathcal{O}}(\phi, \mathbf{k}_{d-2})\alpha^{\text{in}*} + \Psi^{\text{in}}Q_{\mathcal{O}}(\phi, \mathbf{k}_{d-2})S^*(\phi, \mathbf{k}_{d-2})\alpha^{\text{in}*} + \Psi^{\text{localized}}\alpha^{\text{in}*}) &= 0, \\ \Rightarrow \tilde{H}(R_{\mathcal{O}}(\phi, \mathbf{k}_{d-2}))(\Psi^{\text{in}}\alpha^{\text{in}'} + \Psi^{\text{out}}V_{\mathcal{O}}(\phi, \mathbf{k}_{d-2})S^T(\phi, \mathbf{k}_{d-2})Q_{\mathcal{O}}^{\dagger}(\phi, \mathbf{k}_{d-2})\alpha^{\text{in}'} + \Psi^{\text{localized}}\alpha^{\text{in}}) &= 0. \end{aligned} \quad (4.45)$$

where we identified $\alpha^{\text{in}'} = Q_{\mathcal{O}}(\phi, \mathbf{k}_{d-2})S^*(\phi, \mathbf{k}_{d-2})\alpha^{\text{in}*}$. Because \mathcal{O} is a symmetry, the solutions of Eq. (4.45) are those of Eq. (4.1) for $S(R_{\mathcal{O}}(\phi, \mathbf{k}_{d-2}))$. Therefore, the scattering matrix S is constrained by the symmetry operator \mathcal{O} as:

$$V_{\mathcal{O}}(\phi, \mathbf{k}_{d-2})S^T(\phi, \mathbf{k}_{d-2})Q_{\mathcal{O}}^{\dagger}(\phi, \mathbf{k}_{d-2}) = S(R_{\mathcal{O}}(\phi, \mathbf{k}_{d-2})). \quad (4.46)$$

For example, in the presence of time-reversal symmetry Eq. (4.46) establishes that S is isomorphic to an (anti)symmetric matrix S' at time-reversal invariant momenta. To see this, we first observe that $Q_{\mathcal{T}}V_{\mathcal{T}}^* = V_{\mathcal{T}}Q_{\mathcal{T}}^* = \mathcal{T}^2 = \pm 1$ from Eq. (4.44). Then, we use $Q_{\mathcal{T}}^{\dagger} = V_{\mathcal{T}}^*$ in Eq. (4.46) and find

$$(S(\phi, \mathbf{k}_{d-2})V_{\mathcal{T}}^T(\phi, \mathbf{k}_{d-2}))^T = \pm S(-\phi, -\mathbf{k}_{d-2})V_{\mathcal{T}}^T(\phi, \mathbf{k}_{d-2}). \quad (4.47)$$

At time-reversal invariant momenta, we obtain $S' = \pm S'^T$ for $S' = SV_{\mathcal{T}}^T$.

4.8. FACTORING OUT COMMUTING SYMMETRIES

Whenever a symmetry group has a unitary symmetry C_n that commutes with all other elements and satisfies $C_n^n(\phi) = C_n^n(0) \exp(i\phi)$, we use the subspaces of C_n to make the reflection matrix block-diagonal. Because the eigenvalues of C_n are proportional to $\exp(i(\phi + 2\pi j)/n)$, for $j \in [0, n)$ the index of the eigenvalue, the periodicity of each of the blocks of the reflection matrix becomes $2\pi n$. A phase change of 2π corresponds to a map from the j th block to the next—the $j + 1$ th block. Therefore, instead of considering the entire reflection matrix over the 2π range, we work with only one block over the $2\pi n$ range. We call this procedure factoring out the symmetry C_n , because C_n is no longer a symmetry of a single block.

For example, in Sec. 4.4.1, in addition to the constraints of C_4 and \mathcal{C} , $C_2 = (C_4)^2$ further constrains the reflection matrix as:

$$V_{C_2}(\phi)r(\phi)Q_{C_2}^\dagger = r(\phi), \quad (4.48)$$

where $V_{C_2} = (V_{C_4})^2$ and $Q_{C_2} = (Q_{C_4})^2$. We use the commutation relation in Eq. (4.48) to block-diagonalize r into two blocks associated with the $\lambda_\pm(\phi) = \pm i \exp(-i\phi/2)$ eigenvalues of C_2 :

$$U_{V_{C_2}}(\phi) \begin{pmatrix} \lambda_+(\phi) & \\ & \lambda_-(\phi) \end{pmatrix} U_{V_{C_2}}^\dagger(\phi) r(\phi) U_{Q_{C_2}}(\phi) \begin{pmatrix} \lambda_+(\phi) & \\ & \lambda_-(\phi) \end{pmatrix} U_{Q_{C_2}}^\dagger(\phi) = r(\phi), \quad (4.49)$$

where $U_{V_{C_2}}(\phi)$ and $U_{Q_{C_2}}(\phi)$ are the eigenvectors of $V_{C_2}(\phi)$ and $Q_{C_2}(\phi)$. Because $[C_2, C_4] = [C_2, \mathcal{C}] = 0$, each block remains constrained by C_4 and \mathcal{C} . Additionally, because the eigenvalues of C_2 swap when ϕ changes by 2π , the blocks of r swap as well. Therefore, each block contains the full information of the reflection matrix in the 4π range. Without loss of generality, we redefine $2\phi \rightarrow \phi$ and redefine $r(\phi)$ as one of the blocks:

$$r(\phi) := U_{V_{C_2}, -}^\dagger(\phi) r(\phi) U_{Q_{C_2}, -}(\phi). \quad (4.50)$$

The projection in Eq. (4.50) requires applying two different unitaries from the left and right, because r is a linear map from the space of outgoing wavefunctions to the space of incoming wavefunctions.

In Sec. 4.4.2 we use the same strategy to block-diagonalize the reflection matrix r into two blocks associated with the $\pm i \exp(-i\phi/2)$ eigenvalues of C_2 . In Sec. 4.4.3 we block-diagonalize r into two blocks associated with the $\pm i \exp(-i\phi/2)$ eigenvalues of \mathcal{I} at the $k_z = 0, \pi$ lines, which are invariant under inversion.

4.9. IMPLEMENTATION OF A SMOOTH GAUGE CHOICE FOR V AND Q

The expressions for the topological invariants in Eq. (4.14), (4.19), (4.22) involve integrals of the reflection matrices $r(\phi)$ and $r(\phi, \mathbf{k}_{d-2})$ over a line. The reflection matrices are, however, linear maps and not operators, making their eigenvalues gauge-dependent and, in general, discontinuous functions of ϕ and \mathbf{k}_{d-2} . To compute the invariants we need to choose a gauge for the reflection matrices that makes their eigenvalues continuous functions of ϕ and \mathbf{k}_{d-2} .

Because the reflection matrices in the invariant expressions are a result of applying a parameter-dependent basis transformation to the original reflection matrices (see

Eq. (4.50)), we need to construct a smooth gauge for the eigenvectors of $V(\phi)$ and $Q(\phi)$. To do this, we first compute $V(\phi)$ and $Q(\phi)$ for a set of N values $\phi \in [0, 2\pi]$, such that they are 2π -periodic. Then, we compute the eigendecomposition of $V(\phi)$ and $Q(\phi)$ for each ϕ and separate them into two sets:

$$\begin{aligned} V(\phi) &= \lambda_+(\phi)U_{V,+}(\phi)U_{V,+}^\dagger(\phi) + \lambda_-(\phi)U_{V,-}(\phi)U_{V,-}^\dagger(\phi), \\ Q(\phi) &= \lambda_+(\phi)U_{Q,+}(\phi)U_{Q,+}^\dagger(\phi) + \lambda_-(\phi)U_{Q,-}(\phi)U_{Q,-}^\dagger(\phi), \end{aligned} \quad (4.51)$$

where $\lambda_\pm(\phi)$ are eigenvalues of $V(\phi)$ and $Q(\phi)$ smoothly varying with ϕ , and $U_{V,\pm}(\phi)$ and $U_{Q,\pm}(\phi)$ are the corresponding eigenvectors arranged as columns. The latter are not necessarily smooth functions of ϕ , and our goal is to construct a smooth gauge for them.

We construct a smooth gauge for each of the four sets of eigenvectors $U_{V,\pm}(\phi)$ and $U_{Q,\pm}(\phi)$ by iterating over ϕ and following the steps below:

1. Compute the overlap matrix $O(\phi) = U_{V,+}^\dagger(\phi)U_{V,+}(\phi + \delta\phi)$.
2. Compute the singular value decomposition $O(\phi) = U(\phi)S(\phi)V^\dagger(\phi)$.
3. Compute the gauge transformation matrix $G(\phi) = U(\phi)V(\phi)$.
4. Update the eigenvectors $U_{V,\pm}(\phi + \delta\phi) \rightarrow U_{V,\pm}(\phi + \delta\phi)G^\dagger(\phi)$.
5. Repeat for the next value of ϕ , until $\phi = 2\pi$.
6. Compute the overlap matrix $O(2\pi)$ and spread the gauge transformation uniformly over all the eigenvectors.

The last step ensures that the gauge is also 2π -periodic. Additionally, if a symmetry that maps ϕ to $-\phi$ is present, e.g. time-reversal, we further constrain the gauge by choosing symmetric eigenvectors at $\phi = 0, \pi$. By the end of this procedure, the overlap matrix $O(\phi)$ is the identity matrix in the limit $\delta\phi \rightarrow 0$, making the eigenvectors smooth functions of ϕ . We repeat the same procedure for the eigenvectors $U_{V,-}(\phi)$ and $U_{Q,\pm}(\phi)$. The code for constructing the smooth gauge is available in Ref. [54].

REFERENCES

- [1] Frank Schindler et al. “Higher-order topological insulators”. In: *Science Advances* 4.6 (2018), eaat0346. [10.1126/sciadv.aat0346](https://doi.org/10.1126/sciadv.aat0346).
- [2] Wladimir A. Benalcazar, B. Andrei Bernevig, and Taylor L. Hughes. “Electric multipole moments, topological multipole moment pumping, and chiral hinge states in crystalline insulators”. In: *Phys. Rev. B* 96 (24 2017), p. 245115. [10.1103/PhysRevB.96.245115](https://doi.org/10.1103/PhysRevB.96.245115).
- [3] Max Geier et al. “Second-order topological insulators and superconductors with an order-two crystalline symmetry”. In: *Phys. Rev. B* 97 (20 2018), p. 205135. [10.1103/PhysRevB.97.205135](https://doi.org/10.1103/PhysRevB.97.205135).
- [4] Luka Trifunovic and Piet W. Brouwer. “Higher-Order Bulk-Boundary Correspondence for Topological Crystalline Phases”. In: *Phys. Rev. X* 9 (1 2019), p. 011012. [10.1103/PhysRevX.9.011012](https://doi.org/10.1103/PhysRevX.9.011012).

- [5] Luka Trifunovic and Piet W Brouwer. “Higher-Order Topological Band Structures”. In: *Physica Status Solidi (b)* 258.1 (2021), p. 2000090. [10.1002/pssb.202000090](https://doi.org/10.1002/pssb.202000090).
- [6] Zhi-Da Song et al. “Delocalization Transition of a Disordered Axion Insulator”. In: *Phys. Rev. Lett.* 127 (1 2021), p. 016602. [10.1103/PhysRevLett.127.016602](https://doi.org/10.1103/PhysRevLett.127.016602).
- [7] Yan-Bin Yang et al. “Higher-order topological Anderson insulators”. In: *Phys. Rev. B* 103 (8 2021), p. 085408. [10.1103/PhysRevB.103.085408](https://doi.org/10.1103/PhysRevB.103.085408).
- [8] Adam Yanis Chaou et al. “Disordered topological crystalline phases”. In: *Phys. Rev. B* 112 (3 2025), p. 035167. [10.1103/PhysRevB.112.035167](https://doi.org/10.1103/PhysRevB.112.035167).
- [9] Yedi Shen et al. “Disorder-induced phase transitions in three-dimensional chiral second-order topological insulator”. In: *Phys. Rev. B* 109 (3 2024), p. 035303. [10.1103/PhysRevB.109.035303](https://doi.org/10.1103/PhysRevB.109.035303).
- [10] Chang-An Li et al. “Topological Phase Transitions in Disordered Electric Quadrupole Insulators”. In: *Phys. Rev. Lett.* 125 (16 2020), p. 166801. [10.1103/PhysRevLett.125.166801](https://doi.org/10.1103/PhysRevLett.125.166801).
- [11] Zhi-Da Song, Luis Elcoro, and B Andrei Bernevig. “Twisted bulk-boundary correspondence of fragile topology”. In: *Science* 367.6479 (2020), pp. 794–797. [10.1126/science.aaz7659](https://doi.org/10.1126/science.aaz7659).
- [12] Bitan Roy and Vladimir Juričić. “Dislocation as a bulk probe of higher-order topological insulators”. In: *Phys. Rev. Res.* 3 (3 2021), p. 033107. [10.1103/PhysRevResearch.3.033107](https://doi.org/10.1103/PhysRevResearch.3.033107).
- [13] Zhi-Kang Lin et al. “Topological Wannier cycles induced by sub-unit-cell artificial gauge flux in a sonic crystal”. In: *Nature Materials* 21.4 (2022), pp. 430–437. [10.1038/s41563-022-01200-w](https://doi.org/10.1038/s41563-022-01200-w).
- [14] Frank Schindler et al. “Topological zero-dimensional defect and flux states in three-dimensional insulators”. In: *Nature communications* 13.1 (2022), p. 5791. [10.1038/s41467-022-33471-x](https://doi.org/10.1038/s41467-022-33471-x).
- [15] Yizhi You et al. “Higher-order symmetry-protected topological states for interacting bosons and fermions”. In: *Phys. Rev. B* 98 (23 2018), p. 235102. [10.1103/PhysRevB.98.235102](https://doi.org/10.1103/PhysRevB.98.235102).
- [16] Yizhi You, Julian Bibo, and Frank Pollmann. “Higher-order entanglement and many-body invariants for higher-order topological phases”. In: *Phys. Rev. Res.* 2 (3 2020), p. 033192. [10.1103/PhysRevResearch.2.033192](https://doi.org/10.1103/PhysRevResearch.2.033192).
- [17] Ryo Takahashi, Yutaro Tanaka, and Shuichi Murakami. “Bulk-edge and bulk-hinge correspondence in inversion-symmetric insulators”. In: *Phys. Rev. Res.* 2 (1 2020), p. 013300. [10.1103/PhysRevResearch.2.013300](https://doi.org/10.1103/PhysRevResearch.2.013300).
- [18] Max Geier, Ion Cosma Fulga, and Alexander Lau. “Bulk-boundary-defect correspondence at disclinations in rotation-symmetric topological insulators and superconductors”. In: *SciPost Phys.* 10 (2021), p. 092. [10.21468/SciPostPhys.10.4.092](https://doi.org/10.21468/SciPostPhys.10.4.092).
- [19] I. C. Fulga et al. “Scattering formula for the topological quantum number of a disordered multimode wire”. In: *Phys. Rev. B* 83 (15 2011), p. 155429. [10.1103/PhysRevB.83.155429](https://doi.org/10.1103/PhysRevB.83.155429).

- [20] I. C. Fulga, F. Hassler, and A. R. Akhmerov. “Scattering theory of topological insulators and superconductors”. In: *Phys. Rev. B* 85 (16 2012), p. 165409. [10.1103/PhysRevB.85.165409](#).
- [21] Zhe Zhang, Pierre Delplace, and Romain Fleury. “Anomalous topological waves in strongly amorphous scattering networks”. In: *Science Advances* 9.12 (2023), eadg3186. [10.1126/sciadv.adg3186](#).
- [22] Xavier Waintal et al. *Computational quantum transport*. 2024. [10.48550/arXiv.2407.16257](#).
- [23] Josias Langbehn et al. “Reflection-Symmetric Second-Order Topological Insulators and Superconductors”. In: *Phys. Rev. Lett.* 119 (24 2017), p. 246401. [10.1103/PhysRevLett.119.246401](#).
- [24] Luka Trifunovic and Piet Brouwer. “Bott periodicity for the topological classification of gapped states of matter with reflection symmetry”. In: *Phys. Rev. B* 96 (19 2017), p. 195109. [10.1103/PhysRevB.96.195109](#).
- [25] Wladimir A Benalcazar, B Andrei Bernevig, and Taylor L Hughes. “Quantized electric multipole insulators”. In: *Science* 357.6346 (2017), pp. 61–66. [10.1126/science.aah6442](#).
- [26] Ling Lin and Chaohong Lee. “Probing chiral-symmetric higher-order topological insulators with multipole winding number”. In: *Commun Phys* 7 (2024). [10.1038/s42005-024-01884-3](#).
- [27] Hong Wang and Xiaoyu Zhu. “Higher-order topological superconductors characterized by Fermi level crossings”. In: *Phys. Rev. B* 108 (12 2023), p. 125426. [10.1103/PhysRevB.108.125426](#).
- [28] Alexander Cerjan, Terry A. Loring, and Hermann Schulz-Baldes. “Local Markers for Crystalline Topology”. In: *Phys. Rev. Lett.* 132 (7 2024), p. 073803. [10.1103/PhysRevLett.132.073803](#).
- [29] Lucien Jezequel and Pierre Delplace. “Mode-shell correspondence, a unifying phase space theory in topological physics - Part I: Chiral number of zero-modes”. In: *SciPost Phys.* 17 (2024), p. 060. [10.21468/SciPostPhys.17.2.060](#).
- [30] Jia-Zheng Li et al. “Exact Universal Characterization of Chiral-Symmetric Higher-Order Topological Phases”. In: *Preprint* (2024). [10.48550/arXiv.2404.19757](#).
- [31] Yang Peng, Yimu Bao, and Felix von Oppen. “Boundary Green functions of topological insulators and superconductors”. In: *Phys. Rev. B* 95 (23 2017), p. 235143. [10.1103/PhysRevB.95.235143](#).
- [32] Clara S. Weber et al. “Second-order topology and supersymmetry in two-dimensional topological insulators”. In: *Phys. Rev. B* 107 (23 2023), p. 235402. [10.1103/PhysRevB.107.235402](#).
- [33] Christoph W Groth et al. “Kwant: a software package for quantum transport”. In: *New Journal of Physics* 16.6 (2014), p. 063065. [10.1088/1367-2630/16/6/063065](#).

- [34] JT Chalker and PD Coddington. “Percolation, quantum tunnelling and the integer Hall effect”. In: *Journal of Physics C: Solid State Physics* 21.14 (1988), p. 2665. [10.1088/0022-3719/21/14/008](https://doi.org/10.1088/0022-3719/21/14/008).
- [35] B. Kramer, T. Ohtsuki, and S. Kettmann. “Random network models and quantum phase transitions in two dimensions”. In: *Physics Reports* 417.5 (2005), pp. 211–342. [10.1016/j.physrep.2005.07.001](https://doi.org/10.1016/j.physrep.2005.07.001).
- [36] Hui Liu et al. “Network model for higher-order topological phases”. In: *Phys. Rev. B* 103 (11 2021), p. 115428. [10.1103/PhysRevB.103.115428](https://doi.org/10.1103/PhysRevB.103.115428).
- [37] Weiwei Zhu, Y. D. Chong, and Jiangbin Gong. “Symmetry analysis of anomalous Floquet topological phases”. In: *Phys. Rev. B* 104 (2 2021), p. L020302. [10.1103/PhysRevB.104.L020302](https://doi.org/10.1103/PhysRevB.104.L020302).
- [38] Zhi-Hai Liu et al. “Scattering description of edge states in Aharonov-Bohm triangle chains”. In: *Phys. Rev. B* 109 (8 2024), p. L081408. [10.1103/PhysRevB.109.L081408](https://doi.org/10.1103/PhysRevB.109.L081408).
- [39] Hui Liu et al. “Network model for magnetic higher-order topological phases”. In: *Phys. Rev. Res.* 6 (4 2024), p. 043167. [10.1103/PhysRevResearch.6.043167](https://doi.org/10.1103/PhysRevResearch.6.043167).
- [40] J. Zijdeveld et al. <https://gitlab.kwant-project.org/qt/network-models>. To be published. 2024.
- [41] Heqiu Li and Kai Sun. “Pfaffian Formalism for Higher-Order Topological Insulators”. In: *Phys. Rev. Lett.* 124 (3 2020), p. 036401. [10.1103/PhysRevLett.124.036401](https://doi.org/10.1103/PhysRevLett.124.036401).
- [42] Dániel Varjas, Tómas Ö. Rosdahl, and Anton R. Akhmerov. “Qsymm: algorithmic symmetry finding and symmetric Hamiltonian generation”. In: *New Journal of Physics* 20.9 (2018), p. 093026. [10.1088/1367-2630/aadf67](https://doi.org/10.1088/1367-2630/aadf67).
- [43] Xiao-Liang Qi, Taylor L. Hughes, and Shou-Cheng Zhang. “Topological invariants for the Fermi surface of a time-reversal-invariant superconductor”. In: *Phys. Rev. B* 81 (13 2010), p. 134508. [10.1103/PhysRevB.81.134508](https://doi.org/10.1103/PhysRevB.81.134508).
- [44] Roger S. K. Mong, Andrew M. Essin, and Joel E. Moore. “Antiferromagnetic topological insulators”. In: *Phys. Rev. B* 81 (24 2010), p. 245209. [10.1103/PhysRevB.81.245209](https://doi.org/10.1103/PhysRevB.81.245209).
- [45] Fan Zhang, C. L. Kane, and E. J. Mele. “Surface State Magnetization and Chiral Edge States on Topological Insulators”. In: *Phys. Rev. Lett.* 110 (4 2013), p. 046404. [10.1103/PhysRevLett.110.046404](https://doi.org/10.1103/PhysRevLett.110.046404).
- [46] Nicodemos Varnava and David Vanderbilt. “Surfaces of axion insulators”. In: *Phys. Rev. B* 98 (24 2018), p. 245117. [10.1103/PhysRevB.98.245117](https://doi.org/10.1103/PhysRevB.98.245117).
- [47] Benjamin J. Wieder and B. Andrei Bernevig. *The Axion Insulator as a Pump of Fragile Topology*. 2018. [10.48550/arXiv.1810.02373](https://arxiv.org/abs/1810.02373).
- [48] Eslam Khalaf. “Higher-order topological insulators and superconductors protected by inversion symmetry”. In: *Phys. Rev. B* 97 (20 2018), p. 205136. [10.1103/PhysRevB.97.205136](https://doi.org/10.1103/PhysRevB.97.205136).

- [49] Ken Shiozaki, Masatoshi Sato, and Kiyonori Gomi. “Topological crystalline materials: General formulation, module structure, and wallpaper groups”. In: *Phys. Rev. B* 95 (23 2017), p. 235425. [10.1103/PhysRevB.95.235425](https://doi.org/10.1103/PhysRevB.95.235425).
- [50] I. C. Fulga et al. “Statistical topological insulators”. In: *Phys. Rev. B* 89 (15 2014), p. 155424. [10.1103/PhysRevB.89.155424](https://doi.org/10.1103/PhysRevB.89.155424).
- [51] Liang Fu and C. L. Kane. “Topology, Delocalization via Average Symmetry and the Symplectic Anderson Transition”. In: *Phys. Rev. Lett.* 109 (24 2012), p. 246605. [10.1103/PhysRevLett.109.246605](https://doi.org/10.1103/PhysRevLett.109.246605).
- [52] P. W. Brouwer. “Scattering approach to parametric pumping”. In: *Phys. Rev. B* 58 (16 1998), R10135–R10138. [10.1103/PhysRevB.58.R10135](https://doi.org/10.1103/PhysRevB.58.R10135).
- [53] Dganit Meidan, Tobias Micklitz, and Piet W. Brouwer. “Topological classification of adiabatic processes”. In: *Phys. Rev. B* 84 (19 2011), p. 195410. [10.1103/PhysRevB.84.195410](https://doi.org/10.1103/PhysRevB.84.195410).
- [54] R. Johanna Zijderveld, Isidora Araya Day, and Anton R. Akhmerov. *Scattering theory of higher order topological phases*. Dec. 2024. [10.5281/zenodo.14503341](https://doi.org/10.5281/zenodo.14503341).

5

IDENTIFYING BIASES OF THE MAJORANA SCATTERING INVARIANT

Isidora Araya Day, Antonio L. M. Manesco, M. Wimmer, and Anton R. Akhmerov

The easily accessible experimental signatures of Majorana modes are ambiguous and only probe topology indirectly: for example, quasi-Majorana states mimic most properties of Majoranas. Establishing a correspondence between an experiment and a theoretical model known to be topological resolves this ambiguity. Here we demonstrate that already theoretically determining whether a finite system is topological is by itself ambiguous. In particular, we show that the scattering topological invariant—a probe of topology most closely related to transport signatures of Majoranas—has multiple biases in finite systems. For example, we identify that quasi-Majorana states also mimic the scattering invariant of Majorana zero modes in intermediate-sized systems. We expect that the bias due to finite size effects is universal, and advocate that the analysis of topology in finite systems should be accompanied by a comparison with the thermodynamic limit. Our results are directly relevant to the applications of the topological gap protocol.

Own contribution to work: Contributed to defining the project scope, developing the simulations, producing the figures, and writing the manuscript.

Parts of this chapter have been published as *Identifying biases of the Majorana scattering invariant*, [SciPost Phys. Core 8, 047 \(2025\)](#).

5.1. INTRODUCTION

The quest to create a topological phase inevitably faces an obstacle: how to determine whether a system is in fact topological? Unlike simulations that reveal all the information about a system, experimental probes are limited and do not directly measure the signatures of topology [1, 2, 3, 4]. Furthermore, even defining what topological means in a finite system, rather than in the thermodynamic limit, is inherently ambiguous. The celebrated Pfaffian invariant $\text{sign}(\text{Pf}[iH(k=0)]\text{Pf}[iH(k=\pi)])$, for example, tells whether a sufficiently long one-dimensional superconductor hosts Majorana zero modes at its boundaries [5]. Finite size effects couple the Majorana zero modes and give them an energy splitting, which is exponentially small in the length of the superconductor. Therefore, the question of whether a finite sample is topological is as ambiguous as asking whether an exponentially small energy splitting is zero.

An approach to determine the presence of Majorana zero modes in small systems is the scattering invariant [3, 6]. To compute it, we attach a metallic lead to both ends of a Majorana nanowire and obtain the reflection matrix r that relates the incoming and outgoing wave functions from a lead. In the presence of Majorana zero modes, $\text{sign det } r = -1$, while in their absence, $\text{sign det } r = 1$ [3, 6, 7]. Because the determinant of the reflection matrix may only change sign upon the appearance of transmitting modes along the nanowire, phase transitions in the scattering invariant are directly related to a closure of the transport gap. Away from the phase transition the nontrivial scattering invariant predicts the appearance of the zero bias local conductance peak—an experimental signature of Majorana zero modes [1]. This approach has been used to compute the topological invariant in disordered nanowires [8, 9], because it does not require translational invariance and it is computationally efficient.

It is well known that in a finite superconductor the scattering invariant turns trivial if the leads are coupled weakly to the Majorana zero modes by tunnel barriers [3]. This effect vanishes as the length of the nanowire becomes larger, with the scattering invariant converging to topological in the thermodynamic limit. This bias towards the invariant being trivial complicates finding parameters that realize a topological phase. A reverse bias is much more dangerous: identifying a small system as topological while a longer one would be trivial may lead research in an incorrect direction. To mitigate this risk, we answer the following question: what are the mechanisms that lead to a biased interpretation of the scattering invariant in Majorana nanowire simulations? In particular, we investigate biases of the scattering invariant in the presence of quasi-Majorana modes—zero energy modes that are not topologically protected [10, 11, 12].

5.2. SCATTERING INVARIANT IN THE STRONGLY COUPLED LIMIT

The first step to compute a scattering invariant is to define a quantum transport setup where metallic leads are attached to a scattering region. The scattering matrix S relates the amplitudes of the incoming and outgoing modes in the leads:

$$\alpha_{\text{out}} = S\alpha_{\text{in}}, \quad (5.1)$$

where α_{in} and α_{out} are vectors with the modes amplitudes. A direct way to compute the scattering matrix is to use the Hamiltonian of the entire system and the semi-infinite leads and solve the scattering equations numerically [13], for example using the Kwant

package [14]. Alternatively, in the weak coupling limit, the Mahaux-Weidenmüller formula [15] provides an approximation of the scattering matrix:

$$S(E) = 1 - 2\pi i W \left(E - H + i\pi W^\dagger W \right)^{-1} W^\dagger, \quad (5.2)$$

where H is the low-energy Hamiltonian of the scattering region, E is the energy of the incoming modes, and W is the coupling between the lead and the low-energy states of the scattering region. Because H and W only contain low-energy degrees of freedom, the matrices are small, making the Mahaux-Weidenmüller formula especially useful to compute the scattering matrix analytically.

The single metal-superconductor interface shown in Fig. 5.1(a) is sufficient to define the scattering invariant in the thermodynamic limit. As long as the superconductor is gapped, all the sub-gap electron and hole modes that approach the superconductor reflect back into the metallic lead, such that the scattering matrix only consists of a reflection matrix, $S = r$. Because a Hermitian system conserves the total particle number, S is unitary, making $r^\dagger r = 1$. In the particle-hole basis, the reflection matrix is a 2×2 block-matrix that relates the incoming and outgoing electron and hole modes:

$$r = \begin{pmatrix} r_{ee} & r_{eh} \\ r_{he} & r_{hh} \end{pmatrix}, \quad (5.3)$$

where particle-hole symmetry constraints ensure that $r_{ee}(E) = r_{hh}^*(-E)$ and $r_{eh}(E) = r_{he}^*(-E)$. The combination of both constraints at $E = 0$ restricts

$$\mathcal{Q} = \det r, \quad (5.4)$$

to only take values $\mathcal{Q} = \pm 1$. To demonstrate that \mathcal{Q} is a topological invariant, we use the Mahaux-Weidenmüller formula in Eq. (5.2) to compute the scattering matrix with a minimal Hamiltonian in both limits. The trivial limit has no sub-gap modes, therefore $S = 1$ and $\mathcal{Q} = 1$. The topological limit has a single Majorana zero mode at the interface, so that $H = 0$ and $W = (t, t^*)^T$ where we choose the coupling to the lead t to be real. This gives $S(E = 0) = -\sigma_x$ and $\mathcal{Q} = -1$. Furthermore, the value of \mathcal{Q} may only change if the superconducting gap closes and electrons and holes transmit into the superconductor [3, 6], a feature directly related to the appearance of a peak in non-local conductance measurements [3, 4]. The gap closing points separate the trivial regions with $\mathcal{Q} = 1$ from the topological regions with $\mathcal{Q} = -1$.

Counterintuitively, a simple argument shows that making the superconductor finite always gives a trivial scattering invariant. Let us consider a metallic lead attached to a finite trivial region which we gradually tune into a topological phase. For the finite region to undergo a topological phase transition, $\det r$ must continuously change sign and thus cross zero. This is however impossible if there is only one lead attached to the system, because for r to have a zero eigenvalue a transmission into another lead must appear. As a consequence, the invariant cannot change sign and remains $\mathcal{Q} = 1$ for all parameter values. This apparent contradiction appears due to the resonant coupling between the lead and the Majorana zero mode at the terminated end of the superconductor. Therefore, to compute the scattering invariant in a finite system, we must attach two leads, as

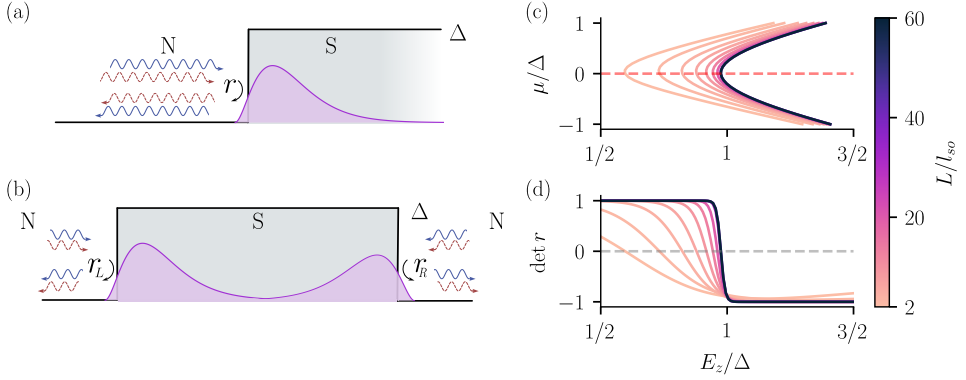


Figure 5.1: Quantum transport setup for computing the scattering invariant in a Majorana nanowire. (a) Normal metallic lead (white) attached to a superconducting nanowire (gray), a one-terminal setup. The incoming electron (blue) and hole (red) modes reflect back from the gapped superconductor. The reflection matrix r encodes the presence of Majorana zero modes (purple). (b) Two-terminal setup with a metallic lead attached to each end of the nanowire. In the thermodynamic limit, the incoming electron and hole modes from both leads reflect back from the superconductor. (c) Phase diagram for nanowires of different lengths, with $l_{\text{so}} = l/\alpha$ the spin-orbit length. The lines show the parameter values where the scattering invariant changes sign. (d) Determinant of the reflection matrix as a function of the Zeeman field across the phase transition for fixed $\mu = 0$, as shown by the red dashed line in (c). Details of the simulation are in the appendix.

shown in Fig. 5.1(b). In this case, the scattering matrix is a 2×2 block-matrix that relates the incoming and outgoing modes in the left (L) and right (R) leads:

$$S = \begin{pmatrix} r_L & t_{LR} \\ t_{RL} & r_R \end{pmatrix}, \quad (5.5)$$

where the blocks r_L and r_R are the reflection matrices for each lead, and t_{LR} and t_{RL} are the transmission matrices between the leads. Because S is unitary, r_L and r_R are sub-unitary instead, and may have zero eigenvalues, which in turn correspond to the phase transition in a finite system. In a two-terminal setup we use $\mathcal{Q} = \text{sign det } r_L = \text{sign det } r_R$. Particle conservation and particle-hole symmetry constraints ensure that the scattering invariant is the same in both leads in a two-terminal setup [3], a result we also confirmed numerically throughout this work.

To compare the scattering invariant in the thermodynamic limit and finite systems, we simulate a microscopic one-dimensional nanowire [16, 17] using the Kwant package [14]. The nanowire has a chemical potential μ , Zeeman field E_Z , spin-orbit coupling α , and superconducting pairing Δ , and the leads are modeled by setting $\Delta = 0$. Details of the simulation are in the appendix and the code for this figure and the rest of the paper are available in Ref. [18]. In the thermodynamic limit, the phase transition occurs at $E_Z = \sqrt{\mu^2 + \Delta^2}$. Figure 5.1(c) shows the phase transition of finite nanowires of different lengths, which we determine by finding the parameters for which the scattering invariant changes sign. This simulation demonstrates the first bias when interpreting the scattering invariant in finite systems: if a nanowire is not sufficiently long, the transition to a topological phase may appear to be at a smaller critical field than in the thermodynamic limit. This is a counterintuitive result, because shorter nanowires are expected to have

a larger energy splitting between the Majorana zero modes, and therefore a larger critical field. We observe that changing the chemical potential in the leads shifts the phase transition to larger Zeeman fields, indicating that the scattering invariant is sensitive to the self-energy of the leads. We thus attribute the bias to the self-energy of the leads: the finite Zeeman field splits the electron and hole modes in the leads, which has a back-action in the properties of the reflection matrix close to the phase transition. Despite the bias, Fig. 5.1(d) shows that for Zeeman fields lower than the true critical value the transmission between the two leads stays sizeable. The quantity $\det r$ is also known in the literature as the topological visibility [19, 20, 21].

5.3. SCATTERING INVARIANT IN THE TUNNELING LIMIT

The back-action of the lead on the scattering region becomes smaller if the lead is coupled through a tunnel barrier. Tunnel barriers are also useful to identify individual states through resonant tunneling and they have practical advantages for measuring non-local conductance. Because we have identified the self-energy of the leads as a source of bias, it is natural to consider tunnel barriers as a solution to this problem. In this section we show that tunnel barriers introduce their own biases too.

5.3.1. STRONG MAJORANA OVERLAP

An effective description of the finite nanowire with tunnel barriers is given by the Hamiltonian:

$$H_{\text{NW}} = \begin{pmatrix} 0 & iE_M \\ -iE_M & 0 \end{pmatrix}, \quad W = \begin{pmatrix} t_L & 0 \\ t_L^* & 0 \\ 0 & t_R \\ 0 & t_R^* \end{pmatrix} \quad (5.6)$$

where H_{NW} is the Hamiltonian in the Majorana basis and W is the coupling matrix between the Majorana zero modes and the leads. The columns of W are in the Majorana basis, while the rows are in the electron and hole mode basis of the right and left leads, $\{\psi_{L,e}, \psi_{L,h}, \psi_{R,e}, \psi_{R,h}\}$. The coupling E_M between the Majorana zero modes is exponentially small in the length of the nanowire, and the tunnel barriers determine the tunneling amplitudes t_L and t_R between the left and right leads and the Majorana zero modes, respectively. Here we disregard the coupling between the Majorana zero modes and the lead at the opposite end of the nanowire for simplicity.

To find an analytical expression for the scattering invariant, we substitute Eq. (5.6) into the Mahaux-Weidenmüller formula (5.2):

$$\det r = \frac{E_M^2 - \Gamma_L \Gamma_R}{E_M^2 + \Gamma_L \Gamma_R} = \begin{cases} < 0 & \text{if } E_M < \sqrt{\Gamma_L \Gamma_R}, \\ > 0 & \text{if } E_M > \sqrt{\Gamma_L \Gamma_R}, \end{cases} \quad (5.7)$$

where $\Gamma_i = 2\pi|t_i|^2$. This result constitutes another bias: the scattering invariant is agnostic to the presence of Majorana zero modes if the coupling to the leads is smaller than the Majoranas' energy splitting [3], $\Gamma_i \ll E_M$. We also confirm this bias beyond the weak coupling limit by solving the scattering equations numerically in a microscopic nanowire with two Gaussian-shaped tunnel barriers of height V_0 , as shown in Fig. 5.2(a). Because E_M is exponentially small in the length of the nanowire, the scattering invariant may indicate a trivial phase in a system that is topological in the thermodynamic limit.

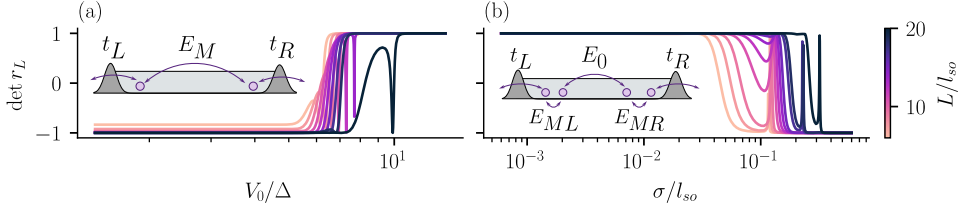


Figure 5.2: Scattering invariant of a finite nanowire with symmetric tunnel barriers. (a) Nanowire in the Majorana regime, $\mu^2 + \Delta^2 > E_Z^2$, with varying tunnel barrier amplitude V_0 . (b) Nanowire in the quasi-Majorana regime (trivial) as a function of the tunnel barrier width σ . The insets illustrate the low-energy degrees of freedom (purple circles) with their effective couplings (arrows).

5.3.2. QUASI-MAJORANA STRONG OVERLAP

That the scattering invariant is blind to modes that are weakly coupled to the leads is no surprise: in the limit where a mode is not coupled at all, it cannot be detected. The mechanism, however, raises an interesting question: are there any regimes where trivial states may be misinterpreted as topological? Generally, two trivial bound states localized at the same end of the nanowire couple to each other and gap out. However, the presence of a smooth position-dependent potential may suppress the hybridization of the bound states, making them robust to changes in the systems parameters [10, 11, 12]. Due to their stability and the similarity of their signatures to Majorana zero modes [22, 23], these states are known as quasi-Majorana modes. Distinguishing them is an open challenge in the field.

The effective Hamiltonian of a nanowire with quasi-Majorana modes is:

$$H_{\text{NW}} = \begin{pmatrix} 0 & iE_{ML} & 0 & 0 \\ -iE_{ML} & 0 & iE_0 & 0 \\ 0 & -iE_0 & 0 & iE_{MR} \\ 0 & 0 & -iE_{MR} & 0 \end{pmatrix}, \quad W = \begin{pmatrix} t_L & 0 & 0 & 0 \\ t_L^* & 0 & 0 & 0 \\ 0 & 0 & 0 & t_R \\ 0 & 0 & 0 & t_R^* \end{pmatrix}, \quad (5.8)$$

where H_{NW} and the columns of W are in the Majorana basis that label the four quasi-Majorana modes, while the rows are the same as in the previous case. E_{ML} and E_{MR} couple quasi-Majorana modes at the same end of the nanowire, while E_0 couples the quasi-Majorana modes at opposite ends. For simplicity, we only consider nearest-neighbor couplings between the quasi-Majorana modes and the leads, as shown in the inset of Fig. 5.2(b). Once again we use the Mahaux-Weidenmüller formula (5.2) to obtain an analytical expression for the scattering invariant:

$$\det r = \frac{-E_0^2 \Gamma_L \Gamma_R + E_{ML}^2 E_{MR}^2}{E_0^2 \Gamma_L \Gamma_R + E_{ML}^2 E_{MR}^2}, \quad (5.9)$$

where $\Gamma_i = 2\pi|t_i|^2$. Remarkably, in the regime where one pair of quasi-Majorana modes is strongly coupled to the leads while the other is not, $|\Gamma_L|, |\Gamma_R|, E_0 \gg E_{ML}, E_{MR}$, the scattering invariant becomes $\mathcal{Q} = -1$. This is shown in Fig. 5.2(b) for a microscopic one-dimensional nanowire with Gaussian-shaped tunnel barriers, where the width σ of the tunnel barriers controls E_{ML} , E_{MR} , Γ_L , and Γ_R . Without further analysis, one may incorrectly interpret the trivial quasi-Majorana modes as Majorana zero modes.

5.3.3. QUASIPARTICLE SINKS

That the scattering invariant may be computed from the left or right leads in a two-terminal setup is a general and robust property that holds for any 2×2 block-matrix scattering matrix. We illustrate this using random matrices and computing the determinant of the diagonal blocks. The results are shown in Fig. 5.3(a): both blocks always share the same determinant, as expected in a two-terminal setup. This property breaks in the presence of additional quasiparticle sinks or sources in the system, for example an additional lead attached to the nanowire. Any other mechanism that loses particles into the environment, like superconducting vortices or non-hermitian effects, has a similar consequence. We illustrate the breakdown of the equivalence between the scattering invariants using random matrices with a 3×3 block structure in Fig. 5.3(b), where the third block represents the quasiparticle sink. The impact of quasiparticle sinks in the scattering invariant is relevant in interpreting the results the topological gap protocol [8, 9] because the simulation results used to calibrate it [24] show in Fig. 5.3(c) a significant deviation from the two-terminal behavior. This deviation likely occurs due to the presence of a Dynes parameter mentioned in Ref. [8].

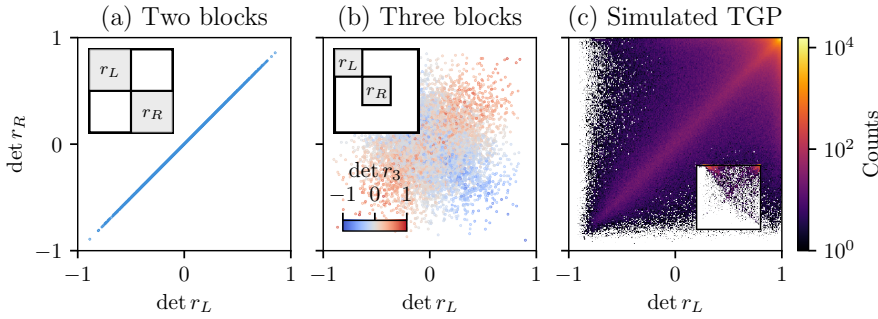


Figure 5.3: Distribution of the scattering invariant computed from the left and right leads in correct and incorrect setups. (a) Determinant of the diagonal blocks of 2×2 special orthogonal matrices sampled randomly. (b) Determinant of the diagonal blocks of 3×3 special orthogonal matrices sampled randomly. (c) Superimposed data of different experiments from the benchmarks of the topological gap protocol [9, 24]. The inset shows the data for the simulation with the largest variance of $\det r_R - \det r_L$.

We consider the specific case of a superconductor where the quasiparticles have a finite lifetime and decay into the environment. This is often modeled using an imaginary diagonal term in the superconducting Hamiltonian—the Dynes parameter—which results in a non-hermitian self-energy [19]. We study the effect of the Dynes parameter $\eta > 0$ on the scattering invariant of a nanowire with quasi-Majorana modes. We focus on the effective Hamiltonian of one end of the nanowire:

$$H_{\text{NW}} = \begin{pmatrix} -i\eta & iE_{ML} \\ -iE_{ML} & -i\eta \end{pmatrix}, \quad W = \begin{pmatrix} t_L & 0 \\ t_L^* & 0 \\ 0 & 0 \\ 0 & 0 \end{pmatrix}, \quad (5.10)$$

where H_{NW} is the Hamiltonian in the Majorana basis and W is the coupling matrix between two quasi-Majorana modes at one end of the nanowire and the corresponding

lead, as in Fig. 5.4(a). For simplicity we disregard the coupling to the other quasi-Majorana modes. Using the Mahaux-Weidenmüller formula we find the scattering invariant:

$$\det r = \frac{E_{ML}^2 + \eta^2 - \eta\Gamma_L}{E_{ML}^2 + \eta^2 + \eta\Gamma_L}, \quad (5.11)$$

where $\Gamma_L = 2\pi|t_L|^2$. Equation (5.11) shows that the scattering invariant is topologically nontrivial in the regime $\Gamma_L \gg \eta, E_M^2/\eta$, even though the quasi-Majorana modes are trivial. We confirm this result numerically in a microscopic one-dimensional nanowire with symmetric tunnel barriers, as shown in Fig. 5.4(b). Furthermore, in Fig. 5.4(c) we show that the scattering invariant computed from the left and right leads does not agree in the presence of the Dyson parameter if the coupling to the leads is also asymmetric. This is the third bias we identify, and it demonstrates that the level broadening introduced in Ref. [8, 9] may systematically make the scattering invariant topologically nontrivial in the quasi-Majorana regime, even while keeping the scattering matrix approximately unitary. Even worse than the other cases, this bias persists in the thermodynamic limit, when the two ends of the nanowire are decoupled. It therefore invalidates the topological visibility as a reliable indicator of Majoranas in a system with a single NS interface and dissipative broadening [19].

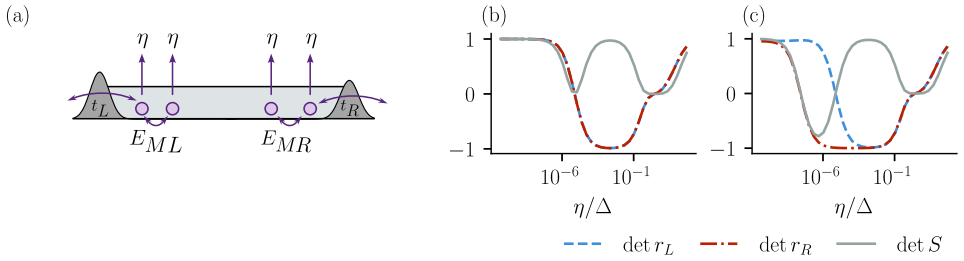


Figure 5.4: Nanowire with quasi-Majorana modes and a Dyson parameter. (a) Illustration of the low-energy degrees of freedom (purple circles) with their effective couplings (arrows). (b) Scattering invariant as a function of the Dyson parameter η for a nanowire with two symmetric tunnel barriers. (c) Scattering invariant as a function of the Dyson parameter η for a nanowire with two asymmetric tunnel barriers of different heights and widths.

5.4. DISCUSSION

We demonstrated multiple ways in which a scattering invariant of a finite system is biased compared to the thermodynamic limit:

- In the open regime, the back-action from the leads enhances Zeeman splitting and pushes the topological transition to smaller fields.
- Weak tunnel couplings to the leads allow Majoranas at the opposite ends of the system to couple, so that the system appears trivial.
- Similarly, resolving the coupling between the quasi-Majorana modes at different ends of the system makes a trivial system appear topological.

These biases diminish as the system size is increased, but they are likely to be relevant to the ongoing experimental efforts. In addition to these biases, we demonstrated that quasiparticle sinks may make quasi-Majorana states appear topological also in the thermodynamic limit.

Our analysis focused on the scattering invariant because of its relation to the transport properties, however, the finite size effects unavoidably affect other topological invariants too. We therefore propose to always combine the analysis of the finite system with a comparison to the behavior in the thermodynamic limit. In disordered systems such analysis must also include disorder averaging and confirming that the results are not influenced by insufficient averaging.

ACKNOWLEDGEMENTS

We thank Henry Legg for drawing our attention to the determinant sign mismatch in Ref. [9]. We thank Roman Lutchyn, Chetan Nayak, Dmitry Pikulin, and Andrey Antipov for useful discussions regarding the topological gap protocol. We acknowledge fruitful discussions with Kostas Vilkelis and Binayyak Bhusan Roy.

DATA AVAILABILITY

The code used to produce the reported results and the generated data are available on Zenodo [18].

Author contributions A. A. and M. W. proposed the research idea. All authors defined the project scope. I. A. D. developed the simulations with input from all authors. I. A. D. and A. M. produced the figures with input from M. W. and A. A. I. A. D, A. M. and A. A. wrote the manuscript with input from M. W.

Funding information This work was supported by the Netherlands Organization for Scientific Research (NWO/OCW) as part of the Frontiers of Nanoscience program and OCENW.GROOT.2019.004.

5.5. DETAILS OF THE TIGHT-BINDING MODEL

Throughout this work, we perform the numerical simulations using a one-dimensional model of a semiconducting nanowire proximitized by a superconductor [16, 17]. The tight-binding Hamiltonian is given by:

$$H = \sum_n \Psi_n^\dagger \mathcal{H} \Psi_n + \Psi_n^\dagger \mathcal{H}^{hop} \Psi_{n+1} + \text{h.c.}, \quad (5.12)$$

$$\mathcal{H} = (2t - \mu) \tau_z + \Delta \tau_x + E_Z \sigma_z, \quad \mathcal{H}^{hop} = \left(-t + \frac{i\alpha}{2} \sigma_y \right) \tau_z,$$

where $\Psi = (c_{n,\uparrow}, c_{n,\downarrow}, -c_{n,\downarrow}^\dagger, c_{n,\uparrow}^\dagger)^T$ is the Nambu spinor of the annihilation operators $c_{n,\sigma}$ of electrons with spin σ at site n . The Pauli matrices τ_i and σ_i act on the particle-hole and spin degrees of freedom, respectively. The hopping amplitude between nearest neighbors is t , which we set to 1, μ is the chemical potential, α is the Rashba spin-orbit

coupling strength, E_Z is the Zeeman energy parallel to the wire. The superconducting pairing potential Δ is finite in the nanowire, and absent in the normal leads.

Additionally, to demonstrate the biases in Fig. 5.2 and Fig. 5.4 we consider tunnel barriers at the ends of the nanowire, which modulate the coupling to the leads. We model the tunnel barriers as a Gaussian potential:

$$H_{\text{barrier}} = \sum_{l=L,R} \sum_n \Psi_n^\dagger \left\{ V_l \exp \left[-\frac{(x_n - x_0)^2}{2\sigma_l^2} \right] \tau_z \right\} \Psi_n, \quad (5.13)$$

where $x_{l=L,R}$ are the center positions of the tunnel barriers, $V_{l=L,R}$ are their maximal heights, and $\sigma_{l=L,R}$ are their standard deviations.

We implement the tight-binding Hamiltonian with the Kwant package [25] and use it to obtain the scattering matrix at zero energy. To ensure that the scattering matrix is real, we provide the particle-hole operator $\mathcal{P} = \sigma_y \tau_y$ to Kwant, see Ref. [18] for the code. To produce Fig. 5.1(c-d) in the main text, we set $\Delta = 0.01$ and $\alpha = 0.1$ in a nanowire with $L = 600$ sites. In Fig. 5.2(a) we use $\mu = 0.1$, $\Delta = 0.05$, $\alpha = 0.02$, $B = 0.2$, $\sigma_L = \sigma_R = 10$ to ensure the Majorana regime in a finite nanowire with $L = 1000$ sites. In Fig. 5.2(b) we use $\mu = 0.12$, $\Delta = 0.05$, $\alpha = 0.02$, $E_Z = 0.1$, and $V_L = V_R = 0.15$ to ensure the quasi-Majorana regime in a finite nanowire with $L = 1000$ sites. We define $l_{\text{so}} = t/\alpha$ as the spin-orbit length.

Finally, to demonstrate the effects of quasiparticle loss, we add a Dynes parameter η to the nanowire Hamiltonian:

$$H_{\text{loss}} = -i \sum_n \eta \Psi_n^\dagger \Psi_n. \quad (5.14)$$

This is a minimal model for a non-hermitian self-energy term in a superconducting system. Figure 5.4 is computed for $\eta \in [10^{-12}, 10]$, $\mu = 0.12$, $\Delta = 0.02$, $\alpha = 0.2$, $E_Z = 0.1$, $V_L = V_R = 0.1$, and $L = 1000$ sites. In Fig. 5.4(a) we use $\sigma_L = \sigma_R = 10$, and in Fig. 5.4(b) we use $\sigma_L = 10$ and $\sigma_R = 20$.

REFERENCES

- [1] K. T. Law, Patrick A. Lee, and T. K. Ng. “Majorana Fermion Induced Resonant Andreev Reflection”. In: *Phys. Rev. Lett.* 103 (23 2009), p. 237001. [10.1103/PhysRevLett.103.237001](https://doi.org/10.1103/PhysRevLett.103.237001).
- [2] Liang Fu and C. L. Kane. “Josephson current and noise at a superconductor/quantum-spin-Hall-insulator/superconductor junction”. In: *Phys. Rev. B* 79 (16 2009), p. 161408. [10.1103/PhysRevB.79.161408](https://doi.org/10.1103/PhysRevB.79.161408).
- [3] A. R. Akhmerov et al. “Quantized Conductance at the Majorana Phase Transition in a Disordered Superconducting Wire”. In: *Phys. Rev. Lett.* 106 (5 2011), p. 057001. [10.1103/PhysRevLett.106.057001](https://doi.org/10.1103/PhysRevLett.106.057001).
- [4] T. Ö. Rosdahl et al. “Andreev rectifier: A nonlocal conductance signature of topological phase transitions”. In: *Phys. Rev. B* 97 (4 2018), p. 045421. [10.1103/PhysRevB.97.045421](https://doi.org/10.1103/PhysRevB.97.045421).
- [5] A Yu Kitaev. “Unpaired Majorana fermions in quantum wires”. In: *Physics-Uspekhi* 44.10S (2001), p. 131. [10.1070/1063-7869/44/10S/S29](https://doi.org/10.1070/1063-7869/44/10S/S29).

- [6] I. C. Fulga et al. “Scattering formula for the topological quantum number of a disordered multimode wire”. In: *Phys. Rev. B* 83 (15 2011), p. 155429. [10 . 1103 / PhysRevB . 83 . 155429](https://doi.org/10.1103/PhysRevB.83.155429).
- [7] I. C. Fulga, F. Hassler, and A. R. Akhmerov. “Scattering theory of topological insulators and superconductors”. In: *Phys. Rev. B* 85 (16 2012), p. 165409. [10 . 1103 / PhysRevB . 85 . 165409](https://doi.org/10.1103/PhysRevB.85.165409).
- [8] Dmitry I Pikulin et al. “Protocol to identify a topological superconducting phase in a three-terminal device”. In: *Preprint* (2021). [10 . 48550 / arXiv . 2103 . 12217](https://doi.org/10.48550/arXiv.2103.12217).
- [9] Morteza Aghaee et al. “InAs-Al hybrid devices passing the topological gap protocol”. In: *Phys. Rev. B* 107 (24 2023), p. 245423. [10 . 1103 / PhysRevB . 107 . 245423](https://doi.org/10.1103/PhysRevB.107.245423).
- [10] G. Kells, D. Meidan, and P. W. Brouwer. “Near-zero-energy end states in topologically trivial spin-orbit coupled superconducting nanowires with a smooth confinement”. In: *Phys. Rev. B* 86 (10 2012), p. 100503. [10 . 1103 / PhysRevB . 86 . 100503](https://doi.org/10.1103/PhysRevB.86.100503).
- [11] Christopher Moore, Tudor D. Stanescu, and Sumanta Tewari. “Two-terminal charge tunneling: Disentangling Majorana zero modes from partially separated Andreev bound states in semiconductor-superconductor heterostructures”. In: *Phys. Rev. B* 97 (16 2018), p. 165302. [10 . 1103 / PhysRevB . 97 . 165302](https://doi.org/10.1103/PhysRevB.97.165302).
- [12] Adriaan Vuik et al. “Reproducing topological properties with quasi-Majorana states”. In: *SciPost Phys.* 7 (2019), p. 061. [10 . 21468 / SciPostPhys . 7 . 5 . 061](https://doi.org/10.21468/SciPostPhys.7.5.061).
- [13] Xavier Waintal et al. “Computational quantum transport”. In: *Preprint* (2024). [10 . 48550 / arXiv . 2407 . 16257](https://doi.org/10.48550/arXiv.2407.16257).
- [14] Christoph W Groth et al. “Kwant: a software package for quantum transport”. In: *New Journal of Physics* 16.6 (2014), p. 063065. [10 . 1088 / 1367 - 2630 / 16 / 6 / 063065](https://doi.org/10.1088/1367-2630/16/6/063065).
- [15] C. Mahaux and H.A. Weidenmüller. *Shell-model Approach to Nuclear Reactions*. North-Holland Publishing Company, 1969.
- [16] Roman M. Lutchyn, Jay D. Sau, and S. Das Sarma. “Majorana Fermions and a Topological Phase Transition in Semiconductor-Superconductor Heterostructures”. In: *Phys. Rev. Lett.* 105 (7 2010), p. 077001. [10 . 1103 / PhysRevLett . 105 . 077001](https://doi.org/10.1103/PhysRevLett.105.077001).
- [17] Yuval Oreg, Gil Refael, and Felix von Oppen. “Helical Liquids and Majorana Bound States in Quantum Wires”. In: *Phys. Rev. Lett.* 105 (17 2010), p. 177002. [10 . 1103 / PhysRevLett . 105 . 177002](https://doi.org/10.1103/PhysRevLett.105.177002).
- [18] Isidora Araya Day et al. *Identifying biases of the Majorana scattering invariant*. 2025. [10 . 5281 / zenodo . 15058838](https://doi.org/10.5281/zenodo.15058838).
- [19] S. Das Sarma, Amit Nag, and Jay D. Sau. “How to infer non-Abelian statistics and topological visibility from tunneling conductance properties of realistic Majorana nanowires”. In: *Phys. Rev. B* 94 (3 2016), p. 035143. [10 . 1103 / PhysRevB . 94 . 035143](https://doi.org/10.1103/PhysRevB.94.035143).
- [20] Sankar Das Sarma and Haining Pan. “Density of states, transport, and topology in disordered Majorana nanowires”. In: *Phys. Rev. B* 108 (8 2023), p. 085415. [10 . 1103 / PhysRevB . 108 . 085415](https://doi.org/10.1103/PhysRevB.108.085415).

- [21] Sankar Das Sarma, Jay D. Sau, and Tudor D. Stanescu. “Spectral properties, topological patches, and effective phase diagrams of finite disordered Majorana nanowires”. In: *Phys. Rev. B* 108 (8 2023), p. 085416. [10.1103/PhysRevB.108.085416](https://doi.org/10.1103/PhysRevB.108.085416).
- [22] Chun-Xiao Liu et al. “Andreev bound states versus Majorana bound states in quantum dot-nanowire-superconductor hybrid structures: Trivial versus topological zero-bias conductance peaks”. In: *Phys. Rev. B* 96 (7 2017), p. 075161. [10.1103/PhysRevB.96.075161](https://doi.org/10.1103/PhysRevB.96.075161).
- [23] Ching-Kai Chiu and S. Das Sarma. “Fractional Josephson effect with and without Majorana zero modes”. In: *Phys. Rev. B* 99 (3 2019), p. 035312. [10.1103/PhysRevB.99.035312](https://doi.org/10.1103/PhysRevB.99.035312).
- [24] Morteza Aghaee et al. *Code and data for 'InAs-Al Hybrid Devices Passing the Topological Gap Protocol'*. Version ed52b7a857. 2025.
- [25] Christoph W Groth et al. “Kwant: a software package for quantum transport”. In: *New Journal of Physics* 16.6 (2014), p. 063065. [10.1088/1367-2630/16/6/063065](https://doi.org/10.1088/1367-2630/16/6/063065).

6

CHIRAL ADIABATIC TRANSMISSION PROTECTED BY FERMI SURFACE TOPOLOGY

Isidora Araya Day, Kostas Vilkelis, Antonio L. M. Manesco, A. Mert Bozkurt,
Valla Fatemi, and Anton R. Akhmerov

We demonstrate that Andreev modes that propagate along a transparent Josephson junction have a perfect transmission at the point where three junctions meet. The chirality and the number of quantized transmission channels is determined by the topology of the Fermi surface and the vorticity of the superconducting phase differences at the trijunction. We explain this chiral adiabatic transmission (CAT) as a consequence of the adiabatic evolution of the scattering modes both in momentum and real space. The dispersion relation of the junction then separates the scattering trajectories by introducing inaccessible regions of phase space. We expect that CAT is observable in nonlocal conductance and thermal transport measurements. Furthermore, because it does not rely on particle-hole symmetry, CAT is also possible to observe directly in metamaterials.

Own contribution to work: Contributed to defining the project scope, performing the numerical simulations, preparing the figures, and writing the manuscript.

Parts of this chapter have been published as *Chiral adiabatic transmission protected by Fermi surface topology*, *SciPost Phys.* 18, 098 (2025).

6.1. INTRODUCTION

Unlike particles that follow deterministic trajectories, waves, both quantum and classical, may split and follow multiple paths. Under special conditions, however, waves follow a deterministic path, transmitting perfectly from source to target. The simplest mechanism that protects such transmission is the adiabaticity of the potential landscape: if the potential changes slowly enough, the wave functions adjust to the local changes of the potential without splitting into partial waves. In a quantum point contact [1], for example, the adiabaticity of the constriction ensures that an integer number of modes pass through, while the rest of the modes reflect. Another mechanism that protects quantized transmission is the topology of a gapped Hamiltonian, which prohibits scattering between channels due to a combination of their symmetry structure and spatial separation. For example, the chiral edge transport of a quantum Hall insulator [2] is protected because the channels propagating in opposite directions occupy different edges of the sample, and are separated by a gapped bulk.

Topological protection, however, extends beyond the bulk properties of an insulator. Specifically, the number of electron- and hole-like Fermi surfaces give rise to the quantized transmission of Andreev modes propagating in a superconductor – normal metal – superconductor (SNS) junction at a π phase difference [3]. While these modes are dispersionless within the Andreev approximation (the linearization of the Hamiltonian at the Fermi level) they acquire charge and velocity due to the nonlinearity of the normal dispersion. At positive voltage bias, the nonlocal conductance measures the number of electron-like *critical points*: Fermi surface points where the velocity is parallel to the interface between the superconductors. Likewise, negative bias conductance counts the number of hole-like critical points. The difference between electron and hole-like critical points is the Euler characteristic of the Fermi surface—a topological invariant [4].

To highlight our main result, we refer the reader to Fig. 6.1: a multiterminal short SNS junction has quantized chiral transmission of Andreev modes (see App. 6.5 and Ref. [5] for the details of numerical simulations). In this device, pairs of superconductors form waveguides for Andreev modes, which occupy an energy range below the superconducting gap and above a minimal energy determined by the phase difference across the junction. At the point where multiple junctions meet, the Andreev modes from different waveguides perfectly transmit clockwise or counterclockwise, depending on the winding of the superconducting phases.

While protected chiral transport also exists in quantum Hall systems, the modes in the SNS junction occupy the same spatial region, and therefore the mechanism is distinct. Furthermore, the different scattering trajectories are not distinguished by any quantum number, which excludes symmetry-based protection. In the following, we examine this phenomenon and explain how chiral transmission emerges from the dispersion of the Andreev states beyond the Andreev approximation and the topology of the Fermi surface. Because the scattering is protected by the adiabaticity of the wave function evolution, we name this phenomenon *chiral adiabatic transmission* (CAT).

6.2. PERTURBATIVE ANALYSIS IN A JOSEPHSON JUNCTION

To understand the origin of CAT, we consider a Josephson junction: a normal metal between two superconductors, as shown in Fig. 6.2(a). We generalize the result of Ref. [3] to

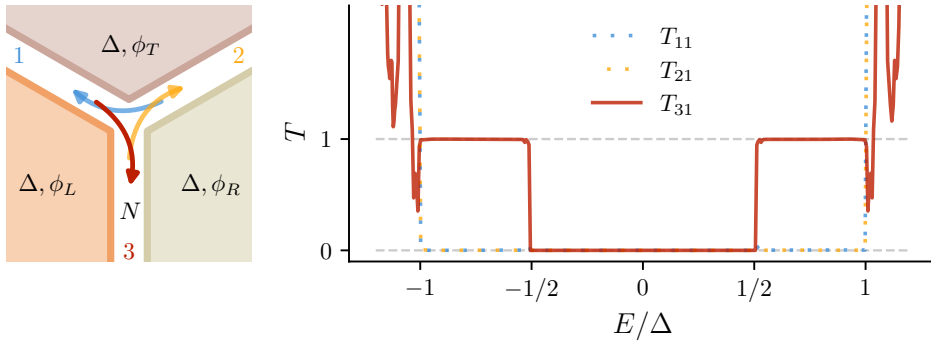


Figure 6.1: A three-terminal Josephson junction has quantized chiral transmission of Andreev modes. Left: Three superconductors with an infinitesimally narrow ballistic metal in between (N). The superconductors have the same normal Hamiltonian with chemical potential μ . The gap Δ is constant, but the superconducting phases ϕ_T , ϕ_L , and ϕ_R differ, such that all the phase differences are $2\pi/3$. Andreev modes propagate along the junctions as shown by the arrows. Right: Transmission of Andreev modes from lead 1 into itself (T_{11}), lead 2 (T_{21}), and lead 3 (T_{31}), for a Y-shaped three-fold symmetric junction. Transmissions from leads 2 and 3 are not shown, but are likewise quantized and chiral. Above the superconducting gap the scattering modes are not confined to the junctions and all transmission become enabled.

an arbitrary phase difference between the superconductors, as necessary to analyze a tri-junction. To identify the role of corrections to the Andreev approximation, we consider a parabolic dispersion in the direction y , perpendicular to the interface between the superconductors. This is a good approximation close to a critical point and still gives a qualitatively valid description of the dispersion away from the critical point. We consider two s-wave superconductors with a gap Δ and a phase difference $\delta\phi$, with an infinitesimally narrow metal between them. At a fixed momentum k_x parallel to the junction, the Bogoliubov-de Gennes Hamiltonian reads:

$$H(y) = [-a\partial_y^2 - E_x]\tau_z + \Delta \cos(\delta\phi/2)\tau_x + \text{sign}(y)\Delta \sin(\delta\phi/2)\tau_y, \quad (6.1)$$

where $\tau_{x,y,z}$ are Pauli matrices acting on the particle-hole degree of freedom, $2a$ is the inverse effective mass, and E_x is the position of the band bottom. Considering the dispersion near a critical point with $k_x = k_c + \delta k_x$ gives $E_x = -v_x \delta k_x$, and reproduces the Hamiltonian of Ref. [3] when $\delta\phi = \pi$. For a parabolic band, on the other hand, $E_x = \mu - ak_x^2$, with μ the chemical potential.

The Andreev approximation follows from linearizing the dispersion relation around the Fermi momentum $k_{y0} = \pm\sqrt{E_x/|a|}$ in the y -direction as well as using the Ansatz $|\Psi(y)\rangle = \exp(ik_{y0}y)|\psi\rangle$, where $|\psi\rangle$ is a two-component spinor that only changes slowly with y . This approximation is valid when $\Delta \ll E_x$. Applying Eq. (6.1) to $|\Psi(y)\rangle$ and neglecting $\partial_y^2|\psi\rangle$, we find that $|\psi\rangle$ is an eigenstate of the linearized Hamiltonian

$$H_{\pm}^{(0)}(y) = \mp 2iak_{y0}\partial_y\tau_z + \Delta \cos(\delta\phi/2)\tau_x + \text{sign}(y)\Delta \sin(\delta\phi/2)\tau_y. \quad (6.2)$$

This Hamiltonian has one bound state for each sign of $\pm k_{y0}$, which we use to construct

the approximate eigenstates of $H(y)$:

$$|\Psi_{\pm}^{(0)}(y)\rangle = \sqrt{\frac{\Delta \sin|\delta\phi/2|}{v_y}} \begin{pmatrix} \pm 1 \\ 1 \end{pmatrix} \exp\left[\pm i k_{y0} y - \frac{\Delta \sin|\delta\phi/2|}{v_y} |y|\right], \quad (6.3)$$

where $v_y = 2ak_{y0}$. The corresponding eigenvalues $E_{\pm}^{(0)} = \pm\Delta \cos(\delta\phi/2)$ are the result of the Andreev approximation. To go beyond the linear approximation, we project the full Hamiltonian $H(y)$ onto the basis states $|\Psi_{\pm}^{(0)}(y)\rangle$, keep only terms up to $\mathcal{O}(\Delta^2)$, and obtain the effective Hamiltonian

$$H_{\pm} = \Delta \begin{pmatrix} \cos(\delta\phi/2) & \frac{\Delta}{2E_x} \sin^2(\delta\phi/2) \\ \frac{\Delta}{2E_x} \sin^2(\delta\phi/2) & -\cos(\delta\phi/2) \end{pmatrix}. \quad (6.4)$$

This yields the dispersion of the Andreev modes

$$E_{\pm} = \pm\Delta \sqrt{(\Delta/2E_x)^2 \sin^4(\delta\phi/2) + \cos^2(\delta\phi/2)}, \quad (6.5)$$

and the corresponding eigenstates

$$N_{\pm} |\Psi_{\pm}(y)\rangle = \left(\cos(\delta\phi/2) \pm \frac{E_{\pm}}{\Delta} \right) |\Psi_{+}^{(0)}(y)\rangle + \frac{\Delta}{2E_x} \sin^2(\delta\phi/2) |\Psi_{-}^{(0)}(y)\rangle, \quad (6.6)$$

where N_{\pm} is a normalization factor. The relative weights of the momenta $\pm k_{y0}$ contributed by $|\Psi_{\pm}^{(0)}(y)\rangle$ depend on $\delta\phi$ and E_x/Δ , and are only equal at $\delta\phi = \pi$. Away from $\delta\phi = \pi$, the Andreev modes are asymmetric superpositions of the states at $\pm k_{y0}$, and the average momentum of the Andreev modes is misaligned with the junction. Figure 6.2(b) shows the orientation $\theta = \arctan(k_x/\langle k_y \rangle)$ of the average Andreev mode momentum as a function of k_x . At the lowest available energy, the momentum of the Andreev modes is perpendicular to the interface ($\theta \in \{0, \pi\}$). Modes with k_x close to the critical value have $\theta \approx \pm\pi/2$, and additionally their energy increases and eventually exceeds the superconducting gap. There are no modes with momentum parallel to the junction.

In the arms of the trijunction the average momentum of the Andreev modes is slightly misaligned with the junction's direction. Near the intersection, the momentum of the scattering states changes continuously because the superconducting pairing—the only position-dependent Hamiltonian term—is small. While some scattering processes at the trijunction may occur without aligning the momentum of the Andreev modes with the arms of the trijunction (see Fig. 6.3(left)), others necessarily require the momentum to be aligned with the arms at some point during the propagation (see Fig. 6.3(right)). We therefore observe that the dispersion of the arms of the junction forms prohibited regions in the phase space of the scattering modes. To confirm the phase space separation of different scattering trajectories, we perform the Wigner-Weyl transform of the scattering wave functions in the trijunction:

$$\Phi(\mathbf{r}, \mathbf{k}) = \int d\mathbf{r}' e^{-i\mathbf{k}\cdot\mathbf{r}'/\hbar} \psi^* \left(\mathbf{r} + \frac{\mathbf{r}'}{2} \right) \psi \left(\mathbf{r} - \frac{\mathbf{r}'}{2} \right), \quad (6.7)$$

This transform gives the Wigner quasiprobability distribution $\Phi(\mathbf{r}, \mathbf{k})$ of the wave function ψ in phase space. We use that the Wigner distribution is peaked near the Fermi surface and further simplify it by only considering $\mathbf{k} = (k_F(E) \cos\theta, k_F(E) \sin\theta)$, with $k_F(E)$

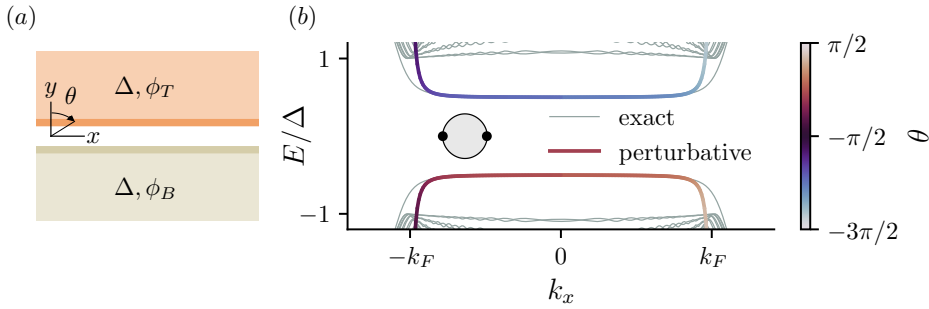


Figure 6.2: The quadratic dispersion of the Andreev modes hybridize states at opposite momenta, enabling the propagation of the Andreev modes along the junction. (a) SNS short junction with arbitrary $\phi_L - \phi_R$ phase difference. (b) Spectrum of the junction in (a) for a normal dispersion with circular Fermi surface, and $\phi_L - \phi_R = 2\pi/3$ computed numerically (gray lines). The inset shows the Fermi surface with the critical points (black dots) of the Fermi surface have $k_x = \pm k_F$, the Fermi wave vector. The perturbative dispersion of the Andreev modes (6.5) is colored according to the angle of the momentum expectation value $\theta = \arctan(k_x/\langle k_y \rangle)$.

the Fermi momentum at the energy of interest. We show in Fig. 6.4(a) the resulting Wigner distributions $\Phi_i(x, y, \theta)$ of the scattering wave functions ψ_i injected from lead i in the Y-shaped junction shown in Fig. 6.1, and confirm that Φ_i indeed do not overlap. Because the asymptotic values of θ depend on the orientation of the trijunction arms, we also expect that the semiclassical trajectories overlap if we decrease the relative angle between any two arms. We confirm this by computing the Wigner distribution of scattering modes in an arrow-shaped trijunction shown in Fig. 6.4(b), where the angle between two pairs of arms is acute. In this geometry the separation of the scattering wave functions in phase space is lost, and therefore the transmission of Andreev quasiparticles is no longer quantized, as shown in Fig. 6.4(c). The separation of modes in momentum space is reminiscent of the mechanism protecting quasi-Majorana modes: approximate zero modes appearing in topologically trivial superconductors with broken time-reversal symmetry in presence of smooth confining potentials [6, 7, 8].

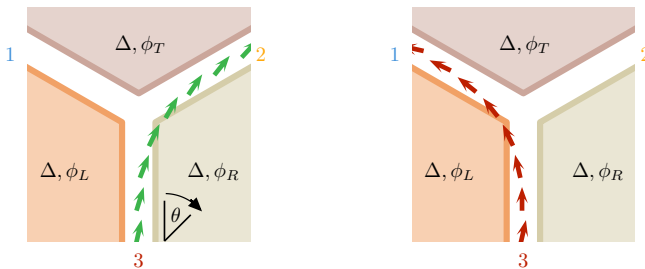


Figure 6.3: Allowed (left) and prohibited (right) scattering processes at the trijunction. The energy of a mode in each of the three metallic arms of the trijunction is as a function of its orientation θ and the phase difference $\delta\phi$. The orientation of the arrows depict the momentum of the modes at each position and at an energy that lies within the superconducting gap.

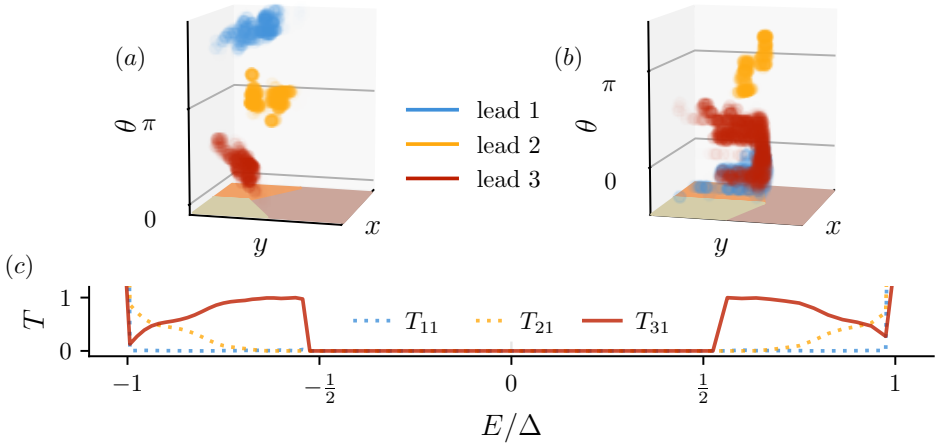


Figure 6.4: Wigner distribution of the scattering wave functions in two trijunctions with all phase differences equal to $2\pi/3$. For clarity, we only show points where the probability density is above 0.2 times the maximum value. The colors label the leads from which the scattering wave functions are injected. In a Y-shaped junction the scattering wave functions are separated in phase space (a), and their transmission is protected (shown in Fig. 6.1). In contrast, in a junction with acute angles between the arms, the Wigner distributions of the scattering wave functions overlap (b). The overlap in the phase space destroys the quantization of the transmissions T_{i1} from lead 1 (c). Transmissions from leads 2 and 3 are not shown.

6.3. CHIRAL ADIABATIC TRANSMISSION IN A TRIJUNCTION

Our arguments rely exclusively on the phase space separation of the scattering wave functions and the adiabatic evolution of the momentum. Therefore, it is natural to expect that CAT does not depend on the details of the junction, the shape of the Fermi surface, or even the presence of particle-hole symmetry. To confirm this assumption, we simulate a trijunction with the following modifications:

- The phase differences across the three junctions are unequal.
- The junction has unequal angles between its arms.
- The Fermi surface is anisotropic.
- Particle-hole symmetry is artificially broken.

The resulting transmissions are shown in Fig. 6.5 (see Appendix 6.5 for the details of the numerical simulations). Despite the modifications, the only qualitative difference from the symmetric trijunction is that the different channels are open at different energy ranges due to the different phase differences. At the energy where modes only exist in one arm, the only allowed process is a reflection of the Andreev modes. At the energy when a conduction channel opens in another arm, the Andreev modes perfectly transmit between the two arms. Finally, only when the three arms have open channels, chiral and quantized transmission is possible and realized.

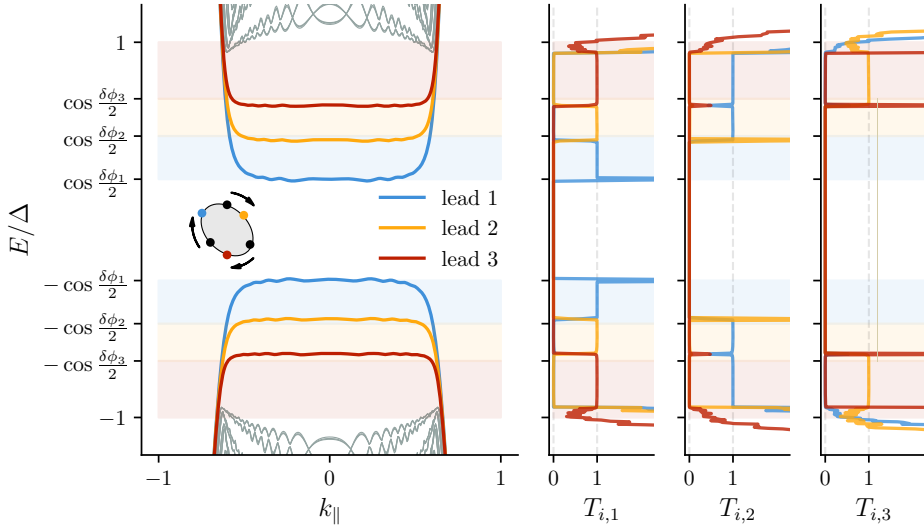


Figure 6.5: Dispersion and quantized chiral transmission of Andreev modes in an asymmetric trijunction with unequal phase differences $\delta\phi_1, \delta\phi_2, \delta\phi_3$. Left: Dispersion of each lead along the junction's direction. The dispersion of modes confined in the junction is colored according to the lead, and the bulk states' dispersion is shown in grey. The leads have the same normal Hamiltonian with an anisotropic Fermi surface (inset), but the critical points are at different momenta, schematically shown with the dots. Right: Transmission of Andreev modes from leads 1, 2, and 3, respectively, into the other leads or themselves. The colors label the outgoing leads.

To prove that CAT is protected by the topology of the Fermi surface, rather than the number of open channels, we consider a model with a next-nearest neighbor hopping in the y -direction, such that it has a peanut-shaped Fermi surface. The resulting transport simulations are shown in Fig. 6.6. The additional critical points of the Fermi surface that appear in two out of three arms of the trijunction create extra particle-like and hole-like channels [3]. At the trijunction the additional channels couple in a way that is sensitive to the junction shape and may either reflect or partially transmit. Despite that, examining the individual transmission eigenvalues—eigenvalues of $t_{ji}t_{ji}^\dagger$ with t_{ji} the transmission matrix from lead i to j —reveals that one of the eigenvalues stays quantized and chiral. This once again follows from the phase space separation of the scattering modes: at least one of the chiral scattering channels in each arm is separated from other all other modes.

So far we focused on the transmission of Andreev modes, without considering the electrical conductance. Our work differs from Ref. [3] in that we consider finite phase differences, and therefore do not rely on time-reversal symmetry. On the other hand, the electrical conductance in Ref. [3] is quantized because it is impossible to couple opposite sides of the Fermi surface in the absence of large momentum scattering. To confirm the robustness of the electrical conductance quantization at arbitrary phase differences, we simulate the interface between a Josephson junction and a normal lead, and compute the transmissions from the Andreev mode to the electron modes T_{ea} and hole modes

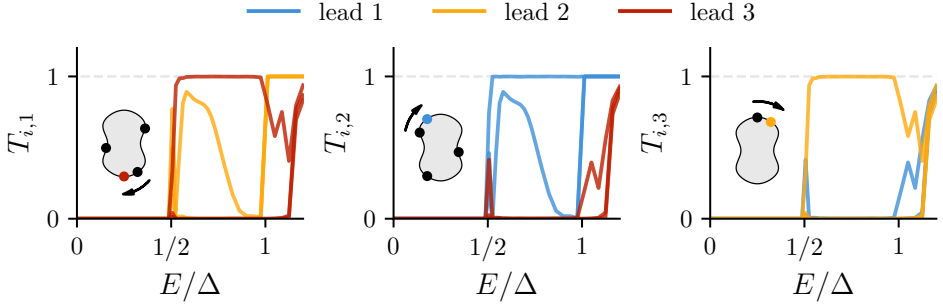


Figure 6.6: CAT in a trijunction with a peanut-shaped Fermi surface, with Euler characteristic $\chi_F = 1$ equal to that of a circular Fermi surface. The panels show the transmission eigenvalues of Andreev modes from lead 1, 2, and 3, respectively, into the other leads, while reflections are not shown. Only one of the eigenvalues per panel is quantized and chiral, process shown by the arrows from critical points in the incoming lead (black dots) to the critical points in the outgoing lead (colored dots). Unprotected transmissions are those not quantized for $\Delta/2 < E < \Delta$.

6

T_{ha} , with the result being shown in Fig. 6.7(a). The electrical conductance in a symmetric NSN geometry equals to $(e^2/h)T_{ea}(T_{ea} - T_{ha})$. We observe that similarly to Ref. [3], the Andreev mode perfectly couples to electron modes at positive bias voltage, and hole modes at negative bias voltage, despite breaking time-reversal symmetry. This generalization to arbitrary phase differences can be understood by thinking of the interface as an SNS junction whose metallic region increases in width until it becomes a normal lead, so that each Andreev mode adiabatically evolves into an electron or hole mode. The perfect injection of electrons into Andreev modes followed by chiral adiabatic transmission and perfect emission of Andreev modes into electrons, results in a quantized nonlocal electrical conductance. This enables a purely electric measurement of chiral adiabatic transmission.

The coupling between the two approximate eigenstates $|\Psi_{\pm}^{(0)}\rangle$ is $\propto \Delta^2/E_x$, and it is similar to the energy Δ^2/μ of a Caroli-de Gennes-Matricon (CdGM) bound state in a superconducting vortex [9], where μ is the distance between the band bottom and the Fermi level. This similarity is not accidental: like the Andreev modes, the momentum distribution of the CdGM states is confined to a cross-section of the Fermi surface and their wave functions possess a similar electron-hole asymmetry. In Fig. 6.7(b), we show that transmission from a CdGM mode to electrons and holes has the same quantized conductance as that of the Andreev modes. We compute the transmissions between two semi-infinite leads: one a superconductor with a vortex and the other a normal metal. Differently from Andreev modes, however, higher energy CdGM modes contribute the same conductance as the lowest energy mode, so that the total number of quantized conductance channels in a vortex is proportional to μ/Δ . The conductance quantization of CdGM modes, together with the unexplained quantization of the rectified conductance in a superconducting quantum point contact [4] hints at a more universal description of the underlying protection.

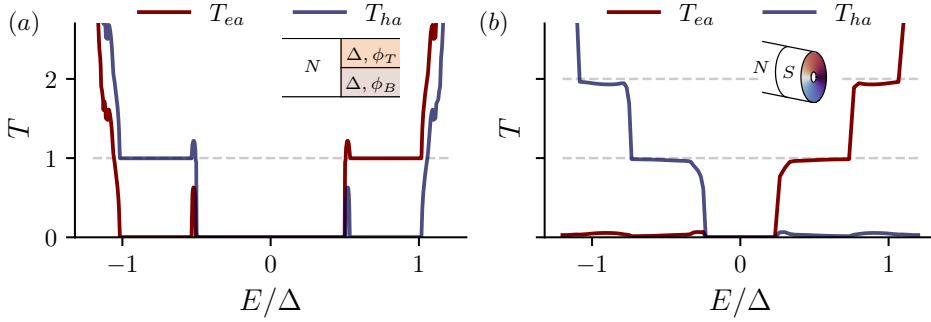


Figure 6.7: Quantization of coupling between Andreev modes and electrons and holes at a normal metal – Josephson junction interface. (a) Transmission of Andreev modes into electron (T_{ea}) and hole (T_{ha}) modes from an infinitesimally narrow Josephson junction lead into a metallic one. (b) Transmission of Andreev modes into electron (T_{ea}) and hole (T_{ha}) modes from a superconducting vortex with a finite metallic core into a metallic lead.

6.4. DISCUSSION AND CONCLUSIONS

An experimental observation of CAT requires a ballistic Josephson junction. While we considered a position-independent normal Hamiltonian, we expect that a sufficiently smooth potential landscape will not affect the transmission. Thus, candidate platforms must have high mobility and smooth normal-superconductor interfaces, potentially realizable in several platforms. Devices with these properties have been fabricated using two-dimensional electron gases [10, 11, 12] and stackings of graphene with superconducting transition metal dicalchogenides [13, 14, 15]. Alternatively, twisted bilayer graphene and Bernal bilayer graphene offer gate-defined Josephson junctions with intrinsic superconductivity tunable by electric fields [16, 17, 18, 19]. The ability to measure nonlocal electrical conductance while the superconductors are grounded poses an additional challenge to observe the imprint of the Fermi surface topology on the Andreev transport. To suppress the contribution of the supercurrent to nonlocal conductance, many experiments operate in the tunneling regime [20, 21, 22, 10], which breaks the quantization of nonlocal conductance. On the other hand, because CAT produces asymmetry of transmission rather than only quantization, it becomes easier to observe. For instance, in addition to purely 2D systems, we expect chiral transport to manifest in high quality films of crystalline superconductors such as aluminum, where the Josephson junctions are formed by narrowing the film thickness. Finally, the chiral nature of the transport makes it observable in thermal transport measurements, which are less sensitive to supercurrent.

Metamaterials offer another platform to observe CAT. Because introducing phase differences requires breaking time-reversal symmetry, single valley transport in photonic or acoustic honeycomb crystals [23, 24, 25, 26] is a promising starting point. In such a system coupling an electron-like and a hole-like band that coexist in a single valley mimics the effect of the superconducting pairing. A displacement of the valleys in momentum space then shifts the relative phase difference, implementing an analog of the

superconducting phase difference. In addition to microscopic control over the effective Hamiltonian, metamaterials naturally allow local high resolution probes and therefore make the chiral nature of the scattering modes directly observable.

In summary, we have analyzed the transport of Andreev modes in a three terminal Josephson junction. We demonstrated that the Fermi surface topology and adiabaticity enable quantized chiral transmission by separating different channels in momentum space. The chiral nature of the transport makes it observable in thermal, rather than only electrical, transport measurements. Furthermore, because the transmission only relies on the adiabaticity, rather than particle-hole symmetry, this phenomenon is also observable in metamaterials. That the same phenomenology applies to superconducting vortices suggests a more general underlying description, which we leave for future work.

ACKNOWLEDGEMENTS

We are grateful to T. Vakhstel for insightful discussions. We thank A. Bordin and A. Young for useful discussions regarding the experimental implementation of the trijunction.

DATA AVAILABILITY

The code used to produce the reported results and the generated data are available on Zenodo [5].

6

Author contributions I. A. D., K. V., A. M., and A. A. performed the numerical simulations. I. A. D., K. V., and A. A. prepared the figures. I. A. D., K. V., A. M., and A. A. wrote the manuscript with input from M. B. and V. F. All authors analyzed the results and participated in defining the project scope. A. A. oversaw the project.

Funding information This work was supported by the Netherlands Organization for Scientific Research (NWO/OCW) as part of the Frontiers of Nanoscience program, an NWO VIDI grant 016.Vidi.189.180, and OCENW.GROOT.2019.004. We also acknowledge funding from the European Research Council (ERC) under the European Union's Horizon 2020 research and innovation program grant agreement №828948 (AndQC).

6.5. APPENDIX

The content in the figures of this paper was computed simulating the following tight-binding Hamiltonian using Kwant [27]:

$$H = H_{\text{superconductor}} + H_{\text{normal}} \quad (6.8)$$

$$H_{\text{superconductor}} = \sum_{\mathbf{n}} \left(\Delta e^{i\phi_{\mathbf{n}}} c_{\mathbf{n},\uparrow}^{\dagger} c_{\mathbf{n},\downarrow}^{\dagger} + \Delta e^{-i\phi_{\mathbf{n}}} c_{\mathbf{n},\downarrow} c_{\mathbf{n},\uparrow} \right), \quad (6.9)$$

$$H_{\text{normal}} = \sum_{\sigma=\uparrow,\downarrow} \sum_{\mathbf{n}} \left[(2t_x + 2t_y - \mu) c_{\mathbf{n},\sigma}^{\dagger} c_{\mathbf{n},\sigma} - \left(t_x c_{\mathbf{n}+\mathbf{e}_x,\sigma}^{\dagger} c_{\mathbf{n},\sigma} + t_y c_{\mathbf{n}+\mathbf{e}_y,\sigma}^{\dagger} c_{\mathbf{n},\sigma} + \text{h.c.} \right) \right], \quad (6.10)$$

where $c_{\mathbf{n},\sigma}^{\dagger}$ ($c_{\mathbf{n},\sigma}$) creates (annihilates) an electron with spin σ at site $\mathbf{n} = (n_x, n_y)$ on a square lattice. The superconducting phase $\phi_{\mathbf{n}}$ is site-dependent, while the supercon-

ducting gap Δ , chemical potential $\mu \in \mathbb{R}$, and the hopping amplitudes t_x, t_y are uniform.

To compute the transmission in the three-fold symmetric trijunction of Fig. 6.1 we use a square lattice of size $L = 100$, with parameters $\mu = 0.5$, $\Delta = 0.1$, $t_x = t_y = 1$, and phases $\phi_L = 2\pi/3$, $\phi_R = -2\pi/3$, and $\phi_T = 0$ for the left, right, and top regions respectively. The system for the trijunction is shown in Fig. 6.8(a), where $\beta = 2\pi/3$ for the three-fold symmetric system. We use the same parameters to compute the band structure in Fig. 6.2 and the Wigner distribution in Fig. 6.4(a). To compute the Wigner distribution in Fig. 6.4(b) and the wavefunctions' transmissions in Fig. 6.4(c) we use the same parameters, but we change decrease the angle between the arms such that $\beta = 7\pi/6$, as shown in Fig. 6.8(b). The code used to compute the transmission is available at [5], together with the code used to generate all the other figures in this paper.

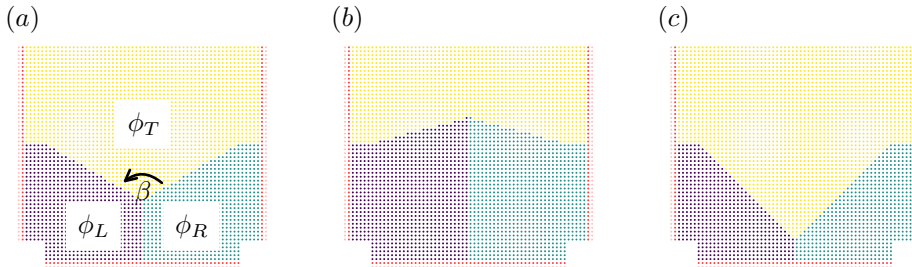


Figure 6.8: The trijunction geometry. The system is composed of three superconducting regions (left, right, and top) of superconducting phase ϕ_L , ϕ_R , and ϕ_T , respectively. The metallic region between them is not present, because it is infinitesimally thin. The left and right leads (red) are periodic in the x-direction, and the bottom lead (red) is periodic in the y-direction. The angle β between the left and right arms of the junction is $2\pi/3$ in (a), $7\pi/6$ in (b), and $\pi/2$ in (c).

In Fig. 6.5 we make Fermi surface anisotropic by adding the diagonal hoppings to the Hamiltonian:

$$H_{\text{anisotropy}} = \sum_{\sigma=\uparrow,\downarrow} \sum_{\mathbf{n}} \left[2t_{xy}c_{\mathbf{n},\sigma}^\dagger c_{\mathbf{n},\sigma} - \left(t_{xy}c_{\mathbf{n}+\mathbf{e}_x+\mathbf{e}_y,\sigma}^\dagger c_{\mathbf{n},\sigma} + \text{h.c.} \right) \right]. \quad (6.11)$$

To compute the spectrum and transmissions in Fig. 6.5, we use a square lattice of size $L = 100$, with parameters $\mu = 0.5$, $\Delta = 0.1$, $t_x = t_y = 1$, and phases $\phi_L = 2\pi/3 + 1/2$, $\phi_R = -2\pi/3$, and $\phi_T = 0$ for the left, right, and top regions respectively. Moreover, we double the electron block of the Hamiltonian $H_{ee} \rightarrow 2H_{ee}$ to artificially break particle-hole symmetry, and we change the angle between the left and right arms of the junction to $\beta = \pi/2$, as shown in Fig. 6.8(c).

In Fig. 6.6 we introduce the peanut-shaped Fermi surface by adding the next-nearest neighbor hoppings to the Hamiltonian:

$$H_{\text{peanut}} = - \sum_{\sigma=\uparrow,\downarrow} \sum_{\mathbf{n}} \left[t_{yy}c_{\mathbf{n}+2\mathbf{e}_y,\sigma}^\dagger c_{\mathbf{n},\sigma} + \text{h.c.} \right]. \quad (6.12)$$

To compute the transmissions in Fig. 6.6, we use a square lattice of size $L = 100$, with

parameters $\mu = 0.5$, $\Delta = 0.1$, $t_x = 1.2$, $t_y = 0.8$, $t_{xy} = 0$, $t_{yy} = -0.5$, and phases $\phi_L = 2\pi/3$, $\phi_R = -2\pi/3$, and $\phi_T = 0$ for the left, right, and top regions respectively.

To compute the electrical conductance between a normal region and a Josephson junction in Fig. 6.7(a) we use a square lattice of size $L = 60$, and uniform parameters $\mu = 0.5$ and $t_x = t_y = 1$ for the whole system. In the superconducting regions we use $\Delta = 0.1$ and a phase difference $\phi_L - \phi_R = \pi/3$. To compute the electrical conductance between a normal region and a superconducting vortex in Fig. 6.7(b) we set up a three-dimensional system with additional nearest-neighbor t_z hoppings in the z-direction and an onsite potential of $2t_z$. We use a lattice of size $L = 30$ and uniform parameters $\mu = 0.9$ and $t_x = t_y = t_z = 1$ for the whole system. In the superconducting region the superconducting phase forms a vortex with $\phi = \arctan(y/z)$, and the superconducting gap is position-dependent, $\Delta(y, z) = 0.25 \times \tanh(\sqrt{y^2 + z^2}/5)$.

REFERENCES

- [1] B. J. van Wees et al. “Quantized conductance of point contacts in a two-dimensional electron gas”. In: *Phys. Rev. Lett.* 60 (9 1988), pp. 848–850. [10.1103/PhysRevLett.60.848](https://doi.org/10.1103/PhysRevLett.60.848).
- [2] B. I. Halperin. “Quantized Hall conductance, current-carrying edge states, and the existence of extended states in a two-dimensional disordered potential”. In: *Phys. Rev. B* 25 (4 1982), pp. 2185–2190. [10.1103/PhysRevB.25.2185](https://doi.org/10.1103/PhysRevB.25.2185).
- [3] Pok Man Tam and Charles L. Kane. “Probing Fermi Sea Topology by Andreev State Transport”. In: *Phys. Rev. Lett.* 130 (9 2023), p. 096301. [10.1103/PhysRevLett.130.096301](https://doi.org/10.1103/PhysRevLett.130.096301).
- [4] Pok Man Tam, Christophe De Beule, and Charles L. Kane. “Topological Andreev rectification”. In: *Phys. Rev. B* 107 (24 2023), p. 245422. [10.1103/PhysRevB.107.245422](https://doi.org/10.1103/PhysRevB.107.245422).
- [5] Isidora Araya Day et al. *Chiral transmission protected by Fermi surface topology*. 2023. [10.5281/zenodo.10201069](https://doi.org/10.5281/zenodo.10201069).
- [6] G. Kells, D. Meidan, and P. W. Brouwer. “Near-zero-energy end states in topologically trivial spin-orbit coupled superconducting nanowires with a smooth confinement”. In: *Phys. Rev. B* 86 (10 2012), p. 100503. [10.1103/PhysRevB.86.100503](https://doi.org/10.1103/PhysRevB.86.100503).
- [7] Elsa Prada, Pablo San-Jose, and Ramón Aguado. “Transport spectroscopy of NS nanowire junctions with Majorana fermions”. In: *Phys. Rev. B* 86 (18 2012), p. 180503. [10.1103/PhysRevB.86.180503](https://doi.org/10.1103/PhysRevB.86.180503).
- [8] Adriaan Vuik et al. “Reproducing topological properties with quasi-Majorana states”. In: *SciPost Phys.* 7 (2019), p. 061. [10.21468/SciPostPhys.7.5.061](https://doi.org/10.21468/SciPostPhys.7.5.061).
- [9] C. Caroli, P.G. De Gennes, and J. Matricon. “Bound Fermion states on a vortex line in a type II superconductor”. In: *Physics Letters* 9.4 (1964), pp. 307–309. [10.1016/0031-9163\(64\)90375-0](https://doi.org/10.1016/0031-9163(64)90375-0).
- [10] A. Banerjee et al. “Local and Nonlocal Transport Spectroscopy in Planar Josephson Junctions”. In: *Physical Review Letters* 130.9 (Feb. 2023). [10.1103/physrevlett.130.096202](https://doi.org/10.1103/physrevlett.130.096202).

- [11] Christian M. Moehle et al. “InSbAs Two-Dimensional Electron Gases as a Platform for Topological Superconductivity”. In: *Nano Letters* 21.23 (Nov. 2021), p. 9990. [10.1021/acs.nanolett.1c03520](https://doi.org/10.1021/acs.nanolett.1c03520).
- [12] J. Shabani et al. “Two-dimensional epitaxial superconductor-semiconductor heterostructures: A platform for topological superconducting networks”. In: *Physical Review B* 93.15 (Apr. 2016). [10.1103/physrevb.93.155402](https://doi.org/10.1103/physrevb.93.155402).
- [13] Tom Dvir et al. “Planar graphene-NbSe₂ Josephson junctions in a parallel magnetic field”. In: *Physical Review B* 103.11 (Mar. 2021). [10.1103/physrevb.103.115401](https://doi.org/10.1103/physrevb.103.115401).
- [14] Minsoo Kim et al. “Strong proximity Josephson coupling in vertically stacked NbSe₂-graphene-NbSe₂ van der Waals junctions”. In: *Nano letters* 17.10 (2017), pp. 6125–6130. [10.1021/acs.nanolett.7b02707](https://doi.org/10.1021/acs.nanolett.7b02707).
- [15] Jongyun Lee et al. “Planar graphene Josephson coupling via van der Waals superconducting contacts”. In: *Current Applied Physics* 19.3 (2019), pp. 251–255. [10.1016/j.cap.2018.06.016](https://doi.org/10.1016/j.cap.2018.06.016).
- [16] Folkert K. de Vries et al. “Gate-defined Josephson junctions in magic-angle twisted bilayer graphene”. In: *Nat. Nano.* 16.7 (May 2021), pp. 760–763. [10.1038/s41565-021-00896-2](https://doi.org/10.1038/s41565-021-00896-2).
- [17] Yiran Zhang et al. “Enhanced superconductivity in spin-orbit proximitized bilayer graphene”. In: *Nature* 613.7943 (2023), pp. 268–273. [10.22002/wecmz-csm13](https://doi.org/10.22002/wecmz-csm13).
- [18] Haoxin Zhou et al. “Isospin magnetism and spin-polarized superconductivity in Bernal bilayer graphene”. In: *Science* 375.6582 (2022), pp. 774–778. [10.1126/science.abm8386](https://doi.org/10.1126/science.abm8386).
- [19] Ying-Ming Xie et al. “Gate-Defined Topological Josephson Junctions in Bernal Bilayer Graphene”. In: *Phys. Rev. Lett.* 131 (14 2023), p. 146601. [10.1103/PhysRevLett.131.146601](https://doi.org/10.1103/PhysRevLett.131.146601).
- [20] J. Schindele et al. “Nonlocal spectroscopy of Andreev bound states”. In: *Phys. Rev. B* 89 (4 2014), p. 045422. [10.1103/PhysRevB.89.045422](https://doi.org/10.1103/PhysRevB.89.045422).
- [21] D. Puglia et al. “Closing of the induced gap in a hybrid superconductor-semiconductor nanowire”. In: *Phys. Rev. B* 103 (23 2021), p. 235201. [10.1103/PhysRevB.103.235201](https://doi.org/10.1103/PhysRevB.103.235201).
- [22] Andreas Pöschl et al. “Nonlocal conductance spectroscopy of Andreev bound states in gate-defined InAs/Al nanowires”. In: *Phys. Rev. B* 106 (24 2022), p. L241301. [10.1103/PhysRevB.106.L241301](https://doi.org/10.1103/PhysRevB.106.L241301).
- [23] Xin-Tao He et al. “A silicon-on-insulator slab for topological valley transport”. In: *Nat. Commun.* 10.1 (2019), p. 872. [10.1038/s41467-019-08881-z](https://doi.org/10.1038/s41467-019-08881-z).
- [24] Yuhao Kang et al. “Pseudo-spin-valley coupled edge states in a photonic topological insulator”. In: *Nat. Commun.* 9.1 (2018), p. 3029. [10.1038/s41467-018-05408-w](https://doi.org/10.1038/s41467-018-05408-w).
- [25] Yang Chen et al. “Topologically Protected Valley-Dependent Quantum Photonic Circuits”. In: *Phys. Rev. Lett.* 126 (23 2021), p. 230503. [10.1103/PhysRevLett.126.230503](https://doi.org/10.1103/PhysRevLett.126.230503).

- [26] Ji-Qian Wang et al. “Extended topological valley-locked surface acoustic waves”. In: *Nat. Commun.* 13.1 (2022), p. 1324. [10 . 1038/s41467-022-29019-8](https://doi.org/10.1038/s41467-022-29019-8).
- [27] Christoph W Groth et al. “Kwant: a software package for quantum transport”. In: *New Journal of Physics* 16.6 (2014), p. 063065. [10 . 1088 / 1367 - 2630 / 16 / 6 / 063065](https://doi.org/10.1088/1367-2630/16/6/063065).

7

PYMABLOCK: AN ALGORITHM AND A PACKAGE FOR QUASI-DEGENERATE PERTURBATION THEORY

Isidora Araya Day, Sebastian Miles, Hugo K. Kerstens, Daniel Varjas,
Anton R. Akhmerov

A common technique in the study of complex quantum-mechanical systems is to reduce the number of degrees of freedom in the Hamiltonian by using quasi-degenerate perturbation theory. While the Schrieffer–Wolff transformation achieves this and constructs an effective Hamiltonian, its scaling is suboptimal, it is limited to two subspaces, and implementing it efficiently is both challenging and error-prone. We introduce an algorithm for constructing an equivalent effective Hamiltonian as well as a Python package, Pymablock, that implements it. Our algorithm combines an optimal asymptotic scaling and the ability to handle any number of subspaces with a range of other improvements. The package supports numerical and analytical calculations of any order and it is designed to be interoperable with any other packages for specifying the Hamiltonian. We demonstrate how the package handles constructing a $k.p$ model, analyses a superconducting qubit, and computes the low-energy spectrum of a large tight-binding model. We also compare its performance with reference calculations and demonstrate its efficiency.

Own contribution to work: Developed the algorithm, wrote the package, and wrote the paper.

Parts of this chapter have been published as *Pymablock: An algorithm and a package for quasi-degenerate perturbation theory*, *SciPost Phys. Codebases* 50 (2025).

7.1. INTRODUCTION

Effective models enable the study of complex quantum systems by reducing the dimensionality of the Hilbert space. Their construction separates the low and high-energy subspaces by block-diagonalizing a perturbed Hamiltonian

$$\mathcal{H} = \begin{pmatrix} H_0^{AA} & 0 \\ 0 & H_0^{BB} \end{pmatrix} + \mathcal{H}', \quad (7.1)$$

where H_0^{AA} and H_0^{BB} are separated by an energy gap, and \mathcal{H}' is a series in a perturbative parameter. This procedure requires finding a series of the basis transformation \mathcal{U} that is unitary and that also cancels the off-diagonal block of the transformed Hamiltonian order by order, as shown in Fig. 7.1. The low-energy effective Hamiltonian $\tilde{\mathcal{H}}^{AA}$ is then a series in the perturbative parameter, whose eigenvalues and eigenvectors are approximate solutions of the complete Hamiltonian. As a consequence, the effective model is sufficient to describe the low-energy properties of the original system while also being simpler and easier to handle.

A common approach to constructing an effective Hamiltonian is the Schrieffer–Wolff transformation [1, 2], also known as Löwdin partitioning [3], or quasi-degenerate perturbation theory. This method parameterizes the unitary transformation $\mathcal{U} = e^{-\mathcal{S}}$ and finds the series \mathcal{S} that decouples the A and B subspaces of $\tilde{\mathcal{H}} = e^{\mathcal{S}}\mathcal{H}e^{-\mathcal{S}}$. This idea enabled advances in multiple fields of quantum physics. As an example, all the k.p models are a result of treating crystalline momentum as a perturbation that only weakly mixes atomic orbitals separated in energy [4, 5, 6, 7]. More broadly, this method serves as a go-to tool in the study of superconducting circuits and quantum dots, where couplings between circuit elements and drives are treated as perturbations to reproduce the dynamics of the system [8, 9]. Applied to time-dependent Hamiltonians, the Schrieffer–Wolff transformation is an essential tool for the design of quantum gates [10, 11].

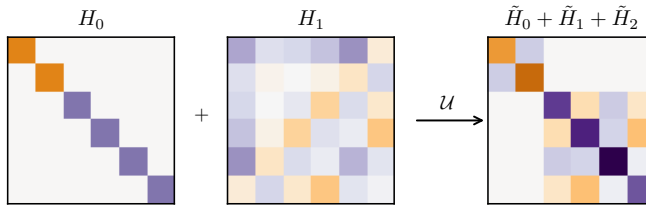


Figure 7.1: Block-diagonalization of a Hamiltonian with a first order perturbation.

Constructing effective Hamiltonians is, however, both algorithmically complex and computationally expensive. This is a consequence of the recursive equations that define the unitary transformation, which require an exponentially growing number of matrix products in each order. In particular, already a 4-th order perturbative expansion that is necessary for many applications may require hundreds of terms. While the computational complexity is only a nuisance when analysing model systems, it becomes a bottleneck whenever the Hilbert space is high-dimensional. Several other approaches improve the performance of the Schrieffer–Wolff algorithm by either using different parametrizations of the unitary transformation [12, 3, 13, 14, 15], adjusting the problem setting to

density matrix perturbation theory [16, 17], or a finding a similarity transform instead of a unitary [18]. An alternative formulation of the perturbative diagonalization uses Wegner's flow equation [19, 20] to construct a continuous unitary transformation (CUT) that depends on a fictitious flow parameter, which at infinity eliminates the undesired terms from the Hamiltonian [21, 22]. CUT is common in the study of many-body systems [23], and it relies on solving a set of differential equations to obtain the effective Hamiltonian. A more recent line of research even applies the ideas of Schrieffer–Wolff transformation to quantum algorithms for the study of many-body systems [24, 25]. Despite these advances, neither of the approaches combines an optimal scaling with the ability to construct effective Hamiltonians.

Another limitation of the Schrieffer–Wolff transformation is that it only decouples two subspaces at a time. While a straightforward generalization of the Schrieffer–Wolff transformation to multiple subspaces is to decouple one block at a time, this approach is suboptimal and depends on the order in which the blocks are decoupled. The literature on multi-block diagonalization is scarce and considers two approaches: the least action or the block-diagonality of the generator [26]. The former constructs a unitary transformation that is as close as possible to the identity, and the latter constructs a block off-diagonal unitary similar to the Schrieffer–Wolff generator. These approaches are useful to design gates for superconducting qubits [27] and to characterize nonlocal interactions in multi-qubit systems [28], both of which require the decoupling of qubit subspaces from different sets of higher energy states. Reference [26], however, showed that the two generalizations of the Schrieffer–Wolff transformation yield different effective Hamiltonians when applied to more than two subspaces. While the perturbative CUT method naturally decouples multiple subspaces [29], in general solving the differential equations inherent to the method may become a computational bottleneck. To our knowledge, there is no general algorithm that constructs effective Hamiltonians for multiple subspaces directly from the least action principle, and how to do so is an open question.

We introduce an algorithm to construct effective models with optimal scaling, thus making it possible to find high order corrections for systems with millions of degrees of freedom. This algorithm exploits the efficiency of recursive evaluations of series satisfying polynomial constraints and obtains the same effective Hamiltonian as the Schrieffer–Wolff transformation in the case of two subspaces. Our algorithm, however, deals with any number of subspaces, providing a generalization of the Schrieffer–Wolff transformation for multi-block diagonalization and selective decoupling between any two states. We make the algorithm available via the open source package Pymablock¹ (PYthon MATRIX BLOCK-diagonalization), a versatile tool for the study of numerical and symbolic models.

7.2. CONSTRUCTING AN EFFECTIVE MODEL

We illustrate the construction of effective models by considering several representative examples. The simplest application of effective models is the reduction of finite symbolic Hamiltonians, which appear in the derivation of low-energy dispersions of materials. Starting from a tight-binding model, one performs Taylor expansions of the Hamiltonian

¹The documentation and tutorials are available in <https://pymablock.readthedocs.io/>

near a k -point, and then eliminates several high-energy states [4, 6]. In the study of superconducting qubits, for example, the Hamiltonian contains several bosonic operators, so its Hilbert space is infinite-dimensional, and the coupling between bosons makes the Hamiltonian impossible to diagonalize. The effective qubit model describes the analytical dependence of qubit frequencies and couplings on the circuit parameters [30, 31, 8, 32, 33, 34]. This allows to design circuits that realize a desired qubit Hamiltonian, as well as ways to understand and predict qubit dynamics, for which computational tools are being actively developed [35, 36, 37]. Finally, mesoscopic quantum devices are described by a single particle tight-binding model with short range hoppings. This produces a numerical Hamiltonian that is both big and sparse, which allows to compute a few of its states but not the full spectrum [38]. Because only the low-energy states contribute to observable properties, deriving how they couple enables a more efficient simulation of the system's behavior.

Pymablock treats all the problems, including the ones above, using a unified approach that only requires three steps:

- Define a Hamiltonian
- Call `pymablock.block_diagonalize`
- Request the desired order of the effective Hamiltonian

The following code snippet shows how to use Pymablock to compute the fourth order correction to an effective Hamiltonian \tilde{H} :

```
# Define perturbation theory
H_tilde, *_ = block_diagonalize([H_0, H_1],
    - subspace_eigenvectors=[vecs_A, vecs_B])

# Request 4th order correction to the effective Hamiltonian
H_AA_4 = H_tilde[0, 0, 4]
```

The function `block_diagonalize` interprets the Hamiltonian $H_0 + H_1$ as a series with two terms, zeroth and first order and calls the block diagonalization routine. The subspaces to decouple are spanned by the eigenvectors `vecs_A` and `vecs_B` of H_0 . This is the main function of Pymablock, and it is the only one that the user ever needs to call. Its first output is a multivariate series whose terms are different blocks and orders of the transformed Hamiltonian. Calling `block_diagonalize` only defines the computational problem, whereas querying the elements of `H_tilde` does the actual calculation of the desired order. This interface treats arbitrary formats of Hamiltonians and system descriptions on the same footing and supports both numerical and symbolic computations.

7.2.1. K.P MODEL OF BILAYER GRAPHENE

To illustrate how to use Pymablock with analytic models, we consider two layers of graphene stacked on top of each other, as shown in Fig. 7.2. Our goal is to find the low-energy

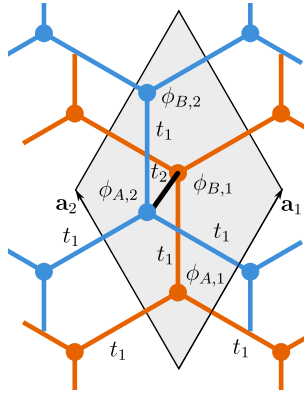


Figure 7.2: Crystal structure and hoppings of AB-stacked bilayer graphene.

model near the \mathbf{K} point [6]. To do this, we first construct the tight-binding model Hamiltonian of bilayer graphene. The main features of the model are its 4-atom unit cell spanned by vectors $\mathbf{a}_1 = (1/2, \sqrt{3}/2)$ and $\mathbf{a}_2 = (-1/2, \sqrt{3}/2)$, and with wave functions $\phi_{A,1}, \phi_{B,1}, \phi_{A,2}, \phi_{B,2}$, where A and B indices are the two sublattices, and 1, 2 are the layers. The model has hoppings t_1 and t_2 within and between the layers, respectively, as shown in Fig. 7.2. We also include a layer-dependent onsite potential $\pm m$.

We define the Bloch Hamiltonian using the Sympy package for symbolic Python [39].

```
t_1, t_2, m = sympy.symbols("t_1 t_2 m", real=True)
alpha = sympy.symbols(r"\alpha")

H = Matrix([
    [m, t_1 * alpha, 0, 0],
    [t_1 * alpha.conjugate(), m, t_2, 0],
    [0, t_2, -m, t_1 * alpha],
    [0, 0, t_1 * alpha.conjugate(), -m]
])
```

$$H = \begin{pmatrix} m & t_1 \alpha & 0 & 0 \\ t_1 \alpha^* & m & t_2 & 0 \\ 0 & t_2 & -m & t_1 \alpha \\ 0 & 0 & t_1 \alpha^* & -m \end{pmatrix}$$

where $\alpha(\mathbf{k}) = 1 + e^{i\mathbf{k}\cdot\mathbf{a}_1} + e^{i\mathbf{k}\cdot\mathbf{a}_2}$, with k the wave vector. We consider $\mathbf{K} = (4\pi/3, 0)$ the reference point in \mathbf{k} -space: $\mathbf{k} = (4\pi/3 + k_x, k_y)$ because $\alpha(\mathbf{K}) = 0$, making k_x and k_y small perturbations. Additionally, we consider $m \ll t_2$ a perturbative parameter.

To call `block_diagonalize`, we need to define the subspaces for the block diagonalization, so we compute the eigenvectors of the unperturbed Hamiltonian at the \mathbf{K} point, $H(\alpha(\mathbf{K}) = m = 0)$. Then, we substitute $\alpha(\mathbf{k})$ into the Hamiltonian, and call the block diagonalization routine using that k_x , k_y , and m are perturbative parameters via the `symbols` argument.

```

vecs = H.subs({alpha: 0, m: 0}).diagonalize(normalize=True)[0]

H_tilde, U, U_adjoint = block_diagonalize(
    H.subs({alpha: alpha_k}),
    symbols=(k_x, k_y, m),
    subspace_eigenvectors=[vecs[:, :2], vecs[:, 2:]] # AA, BB
)

```

The order of the variables in the perturbative series will be that of `symbols`. For example, requesting the term $\propto k_x^i k_y^j m^l$ from the effective Hamiltonian is done by calling `H_tilde[0, 0, i, j, l]`, where the first two indices are the block indices (AA). The series of the unitary transformation U and U^\dagger are also defined, and we may use them to transform other operators.

We collect corrections up to third order in momentum to compute the standard quadratic dispersion of bilayer graphene and trigonal warping. We query these terms from `H_tilde` and those proportional to mass to obtain the effective Hamiltonian (shown as produced by the code)²:

$$\tilde{H}_{\text{eff}} = \begin{bmatrix} m & \frac{3t_1^2}{4t_2}(-k_x^2 - 2ik_x k_y + k_y^2) \\ \frac{3t_1^2}{4t_2}(-k_x^2 + 2ik_x k_y + k_y^2) & -m \end{bmatrix} + \begin{bmatrix} \frac{3mt_1^2}{2t_2^2}(-k_x^2 - k_y^2) & \frac{\sqrt{3}t_1^2}{8t_2}(k_x^3 - 5ik_x^2 k_y + 9k_x k_y^2 + 3ik_y^3) \\ \frac{\sqrt{3}t_1^2}{8t_2}(k_x^3 + 5ik_x^2 k_y + 9k_x k_y^2 - 3ik_y^3) & \frac{3mt_1^2}{2t_2^2}(k_x^2 + k_y^2) \end{bmatrix}$$

The first term is the standard quadratic dispersion of gapped bilayer graphene. The second term contains trigonal warping and the coupling between the gap and momentum. All the terms take less than two seconds in a personal computer to compute.

7.2.2. DISPERSIVE SHIFT OF A TRANSMON QUBIT COUPLED TO A RESONATOR

The need for analytical effective Hamiltonians often arises in circuit quantum electrodynamics (cQED) problems, which we illustrate by studying a transmon qubit coupled to a resonator [8]. Specifically, we choose the standard problem of finding the frequency shift of the resonator due to its coupling to the qubit, a phenomenon used to measure the qubit's state [30]. The Hamiltonian of the system is given by

$$\mathcal{H} = -\omega_t(a_t^\dagger a_t - \frac{1}{2}) + \frac{\alpha}{2} a_t^\dagger a_t^\dagger a_t a_t + \omega_r(a_r^\dagger a_r + \frac{1}{2}) - g(a_t^\dagger - a_t)(a_r^\dagger - a_r), \quad (7.2)$$

where a_t and a_r are bosonic annihilation operators of the transmon and resonator, respectively, and ω_t and ω_r are their frequencies. The transmon has an anharmonicity α , so that its energy levels are not equally spaced. In presence of both the coupling g between the transmon and the resonator and the anharmonicity, this Hamiltonian admits no analytical solution. We therefore treat g as a perturbative parameter.

²The full code is available at https://pymablock.readthedocs.io/en/latest/tutorial/bilayer_graphene.html.

To deal with the infinite dimensional Hilbert space, we observe that the perturbation only changes the occupation numbers of the transmon and the resonator by ± 1 . Therefore computing n -th order corrections to the n_0 -th state allows to disregard states with any occupation numbers larger than $n_0 + n/2$. We want to compute the second order correction to the levels with occupation numbers of either the transmon or the resonator being 0 and 1. We accordingly truncate the Hilbert space to the lowest 3 levels of the transmon and the resonator. The resulting Hamiltonian is a 9×9 matrix that we construct using Sympy [39].

Finally, to compute the energy corrections of the lowest levels, we call the function `block_diagonalize` for each state separately, replicating a regular perturbation theory calculation for single wavefunctions. To do this, we observe that H_0 is diagonal, and use `subspace_indices` to assign the elements of its eigenbasis to the 4 subspaces of interest and the rest. This corresponds to a multi-block diagonalization problem with 5 blocks. For example, to find the qubit-dependent frequency shift of the resonator, χ , we start by computing the second order correction to $|0_t 0_r\rangle$:

```
indices = [0, 1, 2, 3, 4, 4, 4, 4, 4] # 00 is the first state in the
    - basis
H_tilde, *_ = block_diagonalize(H, subspace_indices=indices,
    - symbols=[g])
H_tilde[0, 0, 2][0, 0] # 2nd order correction to 00
```

$$E_{00}^{(2)} = \frac{g^2}{-\omega_r + \omega_t}. \quad (7.3)$$

Repeating this process for the states $|1_t 0_r\rangle$, $|0_t 1_r\rangle$, and $|1_t 1_r\rangle$ requires also requesting `H_tilde[1, 1, 2][0, 0]`, `H_tilde[2, 2, 2][0, 0]`, and `H_tilde[3, 3, 2][0, 0]`. Combining all terms yields the desired resonator frequency shift:

$$\begin{aligned} \chi &= (E_{11}^{(2)} - E_{10}^{(2)}) - (E_{01}^{(2)} - E_{00}^{(2)}) \\ &= -\frac{2g^2}{\alpha + \omega_r - \omega_t} + \frac{2g^2}{-\alpha + \omega_r + \omega_t} - \frac{2g^2}{\omega_r + \omega_t} + \frac{2g^2}{\omega_r - \omega_t} \\ &= -\frac{4\alpha g^2 (\alpha \omega_t - \omega_r^2 - \omega_t^2)}{(\omega_r - \omega_t)(\omega_r + \omega_t)(-\alpha + \omega_r + \omega_t)(\alpha + \omega_r - \omega_t)}. \end{aligned} \quad (7.4)$$

In this example, we have not used the rotating wave approximation, including the frequently omitted counter-rotating terms $\sim a_r a_t$ to illustrate the extensibility of Pymablock. Computing higher order corrections to the qubit frequency only requires increasing the size of the truncated Hilbert space and requesting `H_tilde[0, 0, n]` to any order n .

7.2.3. INDUCED GAP IN A DOUBLE QUANTUM DOT

Large systems pose an additional challenge due to the cubic scaling of linear algebra routines with matrix size. To overcome this, Pymablock is equipped with an implicit method, which utilizes the sparsity of the input and avoids the construction of the full transformed Hamiltonian. We illustrate the efficiency of this method by applying it to a system of two quantum dots coupled to a superconductor between them, shown in

Fig. 7.3, and described by the Bogoliubov-de Gennes Hamiltonian:

$$H_{BdG} = \begin{cases} (\mathbf{k}^2/2m - \mu_{sc})\sigma_z + \Delta\sigma_x & \text{for } L/3 \leq x \leq 2L/3, \\ (\mathbf{k}^2/2m - \mu_n)\sigma_z & \text{otherwise,} \end{cases} \quad (7.5)$$

where the Pauli matrices σ_z and σ_x act in the electron-hole space, \mathbf{k} is the 2D wave vector, m is the effective mass, and Δ the superconducting gap.

We use the Kwant package [40] to build the Hamiltonian of the system³, which we define over a square lattice of $L \times W = 200 \times 40$ sites. On top of this, we consider two perturbations: the barrier strength between the quantum dots and the superconductor, t_b , and an asymmetry of the dots' potentials, $\delta\mu$.

The system is large: it is a sparse array of size 63042×63042 , with 333680 non-zero elements, so even storing all the eigenvectors would take 60 GB of memory. The perturbations are also sparse, with 632, and 126084 non-zero elements for the barrier strength and the potential asymmetry, respectively. The sparsity structure of the Hamiltonian and the perturbations is shown in the left panel of Fig. 7.3, where we use a smaller system of $L \times W = 8 \times 2$ for visualization. Therefore, we use sparse diagonalization [41] and compute only four eigenvectors of the unperturbed Hamiltonian closest to zero energy, which are the Andreev states of the quantum dots.

```
vals, vecs = scipy.sparse.linalg.eigsh(h_0, k=4, sigma=0)
vecs, _ = scipy.linalg.qr(vecs, mode="economic") # orthogonalize the
↳ vectors
```

We now call the block diagonalization routine and provide the computed eigenvectors.

```
H_tilde, *_ = block_diagonalize([h_0, barrier, dmu],
↳ subspace_eigenvectors=[vecs])
```

Because we only provide the low-energy subspace, Pymablock uses the implicit method. Calling `block_diagonalize` is now the most time-consuming step because it requires pre-computing several decompositions of the full Hamiltonian. It is, however, manageable and it only produces a constant overhead of less than three seconds.

To compute the spectrum, we collect the lowest three orders in each parameter in an appropriately sized tensor.

```
h_tilde = np.array(np.ma.filled(H_tilde[0, 0, :3, :3],
↳ fill_value).tolist())
```

This takes two more seconds to run, and we can now compute the low-energy spectrum after rescaling the perturbative corrections by the magnitude of each perturbation.

³The full code is available at https://pymablock.readthedocs.io/en/latest/tutorial/induced_gap.html.

```
def effective_energies(h_tilde, barrier, dmu):
    barrier_powers = barrier ** np.arange(3).reshape(-1, 1, 1, 1)
    dmu_powers = dmu ** np.arange(3).reshape(1, -1, 1, 1)
    return scipy.linalg.eigvalsh(
        np.sum(h_tilde * barrier_powers * dmu_powers, axis=(0, 1))
    )
```

Finally, we plot the spectrum of the 2 Andreev states in Fig. 7.3. As expected, the crossing

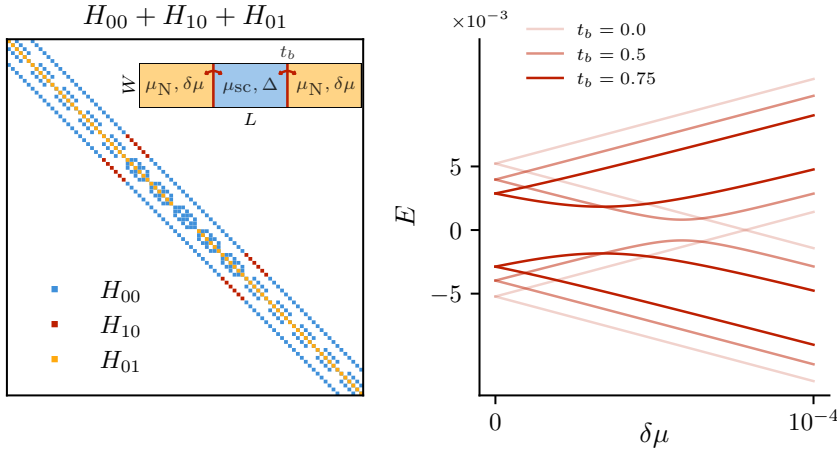


Figure 7.3: Hamiltonian (left) and Andreev levels (right) of two quantum dots coupled to a superconductor (inset). The barrier t_b between the dots and the superconductor, H_{10} , and the asymmetry $\delta\mu$ between the dots' potential, H_{01} , are perturbations.

at $E = 0$ due to the dot asymmetry is lifted when the dots are coupled to the superconductor. In addition, we observe how the proximity gap of the dots increases with the coupling strength.

Computing the spectrum of the system for 3 points in parameter space would require the same time as the total runtime of Pymablock in this example. This demonstrates the speed of the implicit method and the efficiency of Pymablock's algorithm.

7.2.4. SELECTIVE DIAGONALIZATION

Lastly, we demonstrate the generality of Pymablock's algorithm by applying it to decouple arbitrary states in a generic Hamiltonian. This is an alternative to separating a Hamiltonian into blocks, and it requires that the states to decouple are different in energy. To illustrate this, we consider a 16×16 Hamiltonian $\mathcal{H} = H_0 + H_1$ with H_0 a diagonal matrix and H_1 a random Hermitian perturbation. Our goal is to construct an effective Hamiltonian whose only matrix elements are those in a binary mask, which, without loss of generality, we choose to be a smiley face.

We apply the mask to the Hamiltonian by providing it as the `fully_diagonalize`

argument to `block_diagonalize`⁴.

```
H_tilde, *_ = block_diagonalize([H_0, H_1], fully_diagonalize={0:
    - mask})
```

The argument `fully_diagonalize` is a dictionary where the keys label the blocks of the Hamiltonian, and the values are the masks that select the terms to keep in that block. We only used one block in this example: the entire Hamiltonian. Finally, the effective Hamiltonian only contains the terms in the mask, as shown in Fig. 7.4.

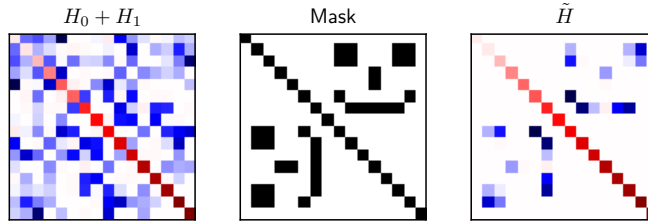


Figure 7.4: Selective diagonalization of a Hamiltonian with a random perturbation.

7.3. PERTURBATIVE BLOCK-DIAGONALIZATION ALGORITHM

7.3.1. PROBLEM STATEMENT

Pymablock finds a series of the unitary transformation \mathcal{U} (we use calligraphic letters to denote series) that eliminates the off-diagonal components of the Hamiltonian

$$\mathcal{H} = H_0 + \mathcal{H}', \quad (7.6)$$

with $\mathcal{H}' = \mathcal{H}'_S + \mathcal{H}'_R$ containing an arbitrary number and orders of perturbations with block-diagonal and block-offdiagonal components, respectively. Here and later we use the subscript S to denote the selected part and R to denote remaining components of a series, with the goal of the perturbation theory to obtain a Hamiltonian with only the selected part. In other words, we aim to find a unitary transformation \mathcal{U} that cancels the remaining part of the Hamiltonian. In different settings, selected and remaining parts may mean different things. In quasi-degenerate perturbation theory, the Hilbert space is subdivided into A and B subspaces, which makes H_0 a block-diagonal matrix

$$H_0 = \begin{pmatrix} H_0^{AA} & 0 \\ 0 & H_0^{BB} \end{pmatrix}, \quad (7.7)$$

and the goal of the perturbation theory is to eliminate the offdiagonal AB and BA blocks of \mathcal{H} . In this case the selected part is the block-diagonal part, and the remaining part is the block-offdiagonal part. Differently, in the context of Rayleigh-Schrödinger perturbation theory, H_0 is a diagonal matrix so that the selected part is the diagonal, and the remaining part of an operator are all its matrix elements that are not on the diagonal.

⁴The full code is available at https://pymablock.readthedocs.io/en/latest/tutorial/getting_started.html#selective-diagonalization.

To consider the problem in the most general setting, we only require the selected and remaining parts of an operator to satisfy the following constraints:

1. The selected and remaining parts of an operator add to identity: $\mathcal{A} = \mathcal{A}_S + \mathcal{A}_R$.
2. Taking either part of an operator is idempotent: $(\mathcal{A}_S)_S = \mathcal{A}_S$.
3. Taking either part commutes with Hermitian conjugation: $(\mathcal{A}_S)^\dagger = (\mathcal{A}^\dagger)_S$.
4. The remaining part of any operator has no matrix elements within eigensubspaces of H_0 . This is required to ensure that the perturbation theory is well-defined.

The separation of an operator into selected and remaining parts is a generalization of taking block-diagonal and block-offdiagonal parts. In particular, the separation allows to choose any subset of the offdiagonal matrix elements as remaining, as long as none of the matrix elements belong to an eigensubspace of H_0 . That none of the matrix elements belong to a same eigensubspace of H_0 becomes evident in the textbook quasi-degenerate perturbation theory, where the corrections to energies and wavefunctions contain differences between energy of the states from different subspaces. The main difference between our generalization and the standard separation into block-diagonal and block-offdiagonal is that the product of a selected part and remaining part of two operators may have a non-zero selected part: $(\mathcal{A}_S \mathcal{B}_R)_S \neq 0$, while $(\mathcal{A}^{AA} \mathcal{B}^{AB})^{AA} = 0$. The generality of the selected and remaining parts allows to consider all perturbation theory methods with the same algorithm, including multi-block diagonalization, selective diagonalization, and the Schrieffer–Wolff transformation. Several expressions simplify if the selected part corresponds to a block-diagonal operator and simplify further if there are only two subspaces. We keep track of these simplifications.

All the series we consider may be multivariate, and they represent sums of the form

$$\mathcal{A} = \sum_{n_1=0}^{\infty} \sum_{n_2=0}^{\infty} \cdots \sum_{n_k=0}^{\infty} \lambda_1^{n_1} \lambda_2^{n_2} \cdots \lambda_k^{n_k} A_{n_1, n_2, \dots, n_k}, \quad (7.8)$$

where λ_i are the perturbation parameters and A_{n_1, n_2, \dots, n_k} are linear operators. The problem statement, therefore, is finding \mathcal{U} and $\tilde{\mathcal{H}}$ such that

$$\tilde{\mathcal{H}} = \mathcal{U}^\dagger \mathcal{H} \mathcal{U}, \quad \tilde{\mathcal{H}}_R = 0, \quad \mathcal{U}^\dagger \mathcal{U} = 1, \quad (7.9)$$

which is schematically shown in Fig. 7.1 for the case of two subspaces, where the selected parts are AA and BB , and the remaining parts are AB and BA . Series multiply according to the Cauchy product:

$$\mathcal{C} = \mathcal{A}\mathcal{B} \Leftrightarrow C_{\mathbf{n}} = \sum_{\mathbf{m}+\mathbf{p}=\mathbf{n}} A_{\mathbf{m}} B_{\mathbf{p}}.$$

The Cauchy product is the most expensive operation in perturbation theory, because it involves a large number of multiplications between potentially large matrices. For example, evaluating \mathbf{n} -th order of \mathcal{C} requires $\sim \prod_i n_i \equiv N$ multiplications of the series elements.⁵ A direct computation of all the possible index combinations in a product

⁵If both \mathcal{A} and \mathcal{B} are known in advance, fast Fourier transform-based algorithms can reduce this cost to $\sim N \log N$. In our problem, however, the series are constructed recursively and therefore this optimization is impossible.

between three series ABC would have a higher cost $\sim N^2$, however, if we use associativity of the product and compute this as $(AB)C$, then the scaling of the cost stays $\sim N$.

There are many ways to solve the problem (7.9) that give identical expressions for \mathcal{U} and $\tilde{\mathcal{H}}$. We are searching for a procedure that satisfies two additional constraints:

- It has the same complexity scaling as a Cauchy product, and therefore $\sim N$ multiplications per additional order.
- It does not require multiplications by H_0 .
- It requires only one Cauchy product by \mathcal{H}_S , the selected part of \mathcal{H} .

The first requirement is that the algorithm scaling is optimal: the desired expression at least contains a Cauchy product of \mathcal{U} and \mathcal{H} . Therefore the complexity scaling of the complete algorithm may not become lower than the complexity of a Cauchy product and we aim to reach this lower bound. The second requirement is because in perturbation theory, n -th order corrections to $\tilde{\mathcal{H}}$ carry n energy denominators $1/(E_i - E_j)$, where E_i and E_j are the eigenvalues of H_0 belonging to different subspaces. Therefore, any additional multiplications by H_0 must cancel with additional energy denominators. Multiplying by H_0 is therefore unnecessary work, and it gives longer intermediate expressions. The third requirement we impose by considering a case in which $\mathcal{H}_R = 0$, where \mathcal{H}_S must at least enter $\tilde{\mathcal{H}}$ as an added term, without any products. Moreover, because \mathcal{U} depends on the entire Hamiltonian, there must be at least one Cauchy product by \mathcal{H}'_S . The goal of our algorithm is thus to be efficient and to produce compact results that do not require further simplifications.

7

7.3.2. EXISTING SOLUTIONS

A common approach to constructing effective Hamiltonians in the 2×2 block case is to use the Schrieffer–Wolff transformation [1]:

$$\begin{aligned} \tilde{\mathcal{H}} &= e^{\mathcal{S}} \mathcal{H} e^{-\mathcal{S}}, \\ e^{\mathcal{S}} &= 1 + \mathcal{S} + \frac{1}{2!} \mathcal{S} \mathcal{S} + \frac{1}{3!} \mathcal{S} \mathcal{S} \mathcal{S} + \dots, \end{aligned} \quad (7.10)$$

where $\mathcal{S} = \sum_n S_n$ is an antihermitian polynomial series in the perturbative parameter, making $e^{\mathcal{S}}$ a unitary transformation. Requiring that $\tilde{\mathcal{H}}^{AB} = 0$ gives a recursive equation for S_n , whose terms are nested commutators between the series of \mathcal{S} and \mathcal{H} . Similarly, the transformed Hamiltonian is given by a series of nested commutators

$$\tilde{\mathcal{H}} = \sum_{j=0}^{\infty} \frac{1}{j!} \left[\mathcal{H}, \sum_{n=0}^{\infty} S_n \right]^{(j)}, \quad (7.11)$$

where the superscript (j) denotes the j -th nested commutator $[A, B]^{(j)} = [[A, B]^{(j-1)}, B]$, with $[A, B]^{(0)} = A$ and $[A, B]^{(1)} = AB - BA$. Regardless of the specific implementation, this expression does not meet either of our two requirements:

- The direct computation of the series elements requires $\sim \exp N$ multiplications, and even an optimized one has a $\sim N^2$ scaling.

- Evaluating Eq. (7.11) contains multiplications by H_0 .

Additionally, while in the 2×2 block case the Schrieffer–Wolff transformation produces a minimal unitary transformation, i.e. as close to identity as possible, this is not the case in the multi-block case [26]. The generalization of this approach to multiple subspaces is an open question [26].

Alternative parametrizations of the unitary transformation \mathcal{U} require solving unitarity and block diagonalization conditions too, but give rise to a different recursive procedure for the series elements. For example, using hyperbolic functions

$$\mathcal{U} = \cosh \mathcal{G} + \sinh \mathcal{G}, \quad \mathcal{G} = \sum_{i=0}^{\infty} G_i, \quad (7.12)$$

leads to different recursive expressions for G_i [13], but does not change the algorithm's complexity. On the other hand, using a polynomial series directly

$$\mathcal{U} = \sum_{i=0}^{\infty} U_i, \quad (7.13)$$

gives rise to another recursive equation for U_i [12, 3, 14, 15]. Still, this choice results in an expression for $\tilde{\mathcal{H}}$ whose terms include products by H_0 , and therefore requires additional simplifications.

Another approach uses Wegner's flow equation [19, 20] to construct a continuous unitary transformation (CUT) that depends smoothly on a fictitious parameter l , $\mathcal{U}(l)$. The goal is to define a generator $\eta(l)$ such that $\mathcal{H}(l) = \mathcal{U}^\dagger(l)\mathcal{H}(0)\mathcal{U}(l)$ flows towards the desired effective Hamiltonian:

$$\frac{d\mathcal{H}(l)}{dl} = [\eta(l), \mathcal{H}(l)], \quad (7.14)$$

where $\mathcal{U}(l)$, $\mathcal{H}(l)$, and $\eta(l)$ are once again series in the perturbative parameters. At $l = \infty$, the transformed Hamiltonian does not contain the undesired terms, $\mathcal{H}(\infty) = \tilde{\mathcal{H}}$. Finding the unitary amounts to solving a set of differential equations

$$\frac{d\mathcal{U}(l)}{dl} = \eta(l)\mathcal{U}(l). \quad (7.15)$$

Together with the Eq. (7.14) and an appropriate choice of η , this gives a set of coupled differential equations, that become linear if solved order by order. The convergence and stability of flow equations depends on the parameterization of the flow generator η , and multiple strategies for this choice are known [23, 42]. The CUT method is common in the study of many-body systems, where one needs to either decompose the Hamiltonian into sets of quasiparticle creation and annihilation operators, or choose a different operator basis together with a set of commutation rules. Despite the numerical complication of solving differential equations, CUT extends beyond the perturbative regime [22, 20, 23].

The following three algorithms satisfy both of our requirements while solving a related problem. First, density matrix perturbation theory [16, 43, 17] constructs the density matrix ρ of a perturbed system as a power series with respect to a perturbative parameter:

$$\rho = \sum_{i=0}^{\infty} \rho_i. \quad (7.16)$$

The elements of the series are found by solving two recursive conditions, $\rho^2 = \rho$ and $[\mathcal{H}, \rho] = 0$, which avoid multiplications by H_0 and require a single Cauchy product each. This approach, however, deals with the entire Hilbert space, rather than the low-energy subspace, and does not provide an effective Hamiltonian. Second, the perturbative similarity transform by C. Bloch [18, 2] constructs the Hamiltonian in a non-orthogonal basis, which preserves the Hamiltonian spectrum while breaking its hermiticity. Third, the recursive Schrieffer–Wolff algorithm [37] applies the Schrieffer–Wolff transformation to the output of lower-order iterations, and calculates the effective Hamiltonian at a fixed perturbation strength, rather than as a series. Finally, none of these linear scaling algorithms above handles more than two subspaces. We thus identify the following open question: can we construct an effective Hamiltonian with a linear scaling algorithm that produces compact expressions?

7.3.3. PYMABLOCK'S ALGORITHM

The first idea that Pymablock exploits is the recursive evaluation of the operator series, which we illustrate by considering the unitarity condition. Let us separate the transformation \mathcal{U} into an identity and $\mathcal{U}' = \mathcal{W} + \mathcal{V}$:

$$\mathcal{U} = 1 + \mathcal{U}' = 1 + \mathcal{W} + \mathcal{V}, \quad \mathcal{W}^\dagger = \mathcal{W}, \quad \mathcal{V}^\dagger = -\mathcal{V}. \quad (7.17)$$

We use the unitarity condition $\mathcal{U}^\dagger \mathcal{U} = 1$ by substituting \mathcal{U}' into it:

$$1 = (1 + \mathcal{U}'^\dagger)(1 + \mathcal{U}') = 1 + \mathcal{U}'^\dagger + \mathcal{U}' + \mathcal{U}'^\dagger \mathcal{U}'. \quad (7.18)$$

This immediately yields

$$\mathcal{W} = \frac{1}{2}(\mathcal{U}'^\dagger + \mathcal{U}') = -\frac{1}{2}\mathcal{U}'^\dagger \mathcal{U}'. \quad (7.19)$$

Because \mathcal{U}' has no 0-th order term, $(\mathcal{U}'^\dagger \mathcal{U}')_{\mathbf{n}}$ does not depend on the \mathbf{n} -th order of \mathcal{U}' nor \mathcal{W} , and therefore Eq. (7.19) allows to compute \mathcal{W} using the already available lower orders of \mathcal{U}' . Alternatively, using Eq. (7.17) we could define \mathcal{W} as a Taylor series in \mathcal{V} :

$$\mathcal{W} = \sqrt{1 + \mathcal{V}^2} - 1 \equiv f(\mathcal{V}) \equiv \sum_n a_n \mathcal{V}^{2n}.$$

A direct computation of all possible products of terms in this expression requires $\sim \exp N$ multiplications. A more efficient approach for evaluating this expression introduces each term in the sum as a new series $\mathcal{A}^{n+1} = \mathcal{A}\mathcal{A}^n$ and reuses the previously computed results. This optimization brings the exponential cost down to $\sim N^2$. However, we see that the Taylor expansion approach is both more complicated and more computationally expensive than the recurrent definition in Eq. (7.19). Therefore, we use Eq. (7.19) to efficiently compute \mathcal{W} . More generally, a Cauchy product $\mathcal{A}\mathcal{B}$ where \mathcal{A} and \mathcal{B} have no 0-th order terms depends on $\mathcal{A}_1, \dots, \mathcal{A}_{n-1}$ and $\mathcal{B}_1, \dots, \mathcal{B}_{n-1}$. This makes it possible to use $\mathcal{A}\mathcal{B}$ in a recurrence relation, a property that we exploit throughout the algorithm.

To compute \mathcal{U}' we also need to find \mathcal{V} , which is defined by the requirement $\tilde{\mathcal{H}}_R = 0$. Additionally, we constrain \mathcal{V} to have no selected part: $\mathcal{V}_S = 0$, a choice we make to minimize the norm of \mathcal{U}' , and satisfy the least action principle [44]. That $\mathcal{V}_S = 0$ minimizes the norm of \mathcal{U}' follows from the following statements:

1. The norm of a series is minimal, when each of the subsequent terms is chosen to be minimal order by order.
2. The Hermitian part of U' , W_n , is determined by the unitarity condition (7.19) at each order from lower orders of U' .
3. The norm of $W_n + V_n$ is minimal, when the norm of V_n is minimal because of Hermiticity properties of \mathcal{W} and \mathcal{V} .
4. Finally, because \mathcal{V}_R is fixed by the requirement $\tilde{\mathcal{H}}_R = 0$, $\mathcal{V}_S = 0$ provides the minimal norm of U' .

In the 2×2 block case, this choice makes \mathcal{W} block-diagonal and ensures that the resulting unitary transformation is equivalent to the Schrieffer–Wolff transformation (see section 7.3.4). In general, however, $\mathcal{W}_R \neq 0$.

The remaining condition for finding a recurrent relation for U' is that the transformed Hamiltonian

$$\tilde{\mathcal{H}} = U^\dagger \mathcal{H} U = \mathcal{H}_S + U'^{\dagger} \mathcal{H}_S + \mathcal{H}_S U' + U'^{\dagger} \mathcal{H}_S U' + U^\dagger \mathcal{H}'_R U, \quad (7.20)$$

has only the selected part $\tilde{\mathcal{H}}_R = 0$, a condition that determines \mathcal{V} . Here we used $U = 1 + U'$ and $\mathcal{H} = \mathcal{H}_S + \mathcal{H}'_R$, since H_0 has no remaining part by definition. Because we want to avoid products by \mathcal{H}_S , we need to get rid of the terms that contain it by replacing them with an alternative expression. Our strategy is to define an auxiliary operator \mathcal{X} that we can compute without ever multiplying by \mathcal{H}_S . Like U' , \mathcal{X} needs to be defined via a recurrence relation, which we determine later. Because Eq. (7.20) contains \mathcal{H}_S multiplied by U' from the left and from the right, eliminating \mathcal{H}_S requires moving it to the same side. To achieve this, we choose $\mathcal{X} = \mathcal{Y} + \mathcal{Z}$ to be the commutator between U' and \mathcal{H}_S :

$$\mathcal{X} \equiv [U', \mathcal{H}_S] = \mathcal{Y} + \mathcal{Z}, \quad \mathcal{Y} \equiv [\mathcal{V}, \mathcal{H}_S] = \mathcal{Y}^\dagger, \quad \mathcal{Z} \equiv [\mathcal{W}, \mathcal{H}_S] = -\mathcal{Z}^\dagger. \quad (7.21)$$

If the selected part \mathcal{A}_S corresponds to a block-diagonal operator, \mathcal{Y} is block off-diagonal. Additionally, in the 2×2 block case \mathcal{Z} is block-diagonal. We use $\mathcal{H}_S U' = U' \mathcal{H}_S - \mathcal{X}$ to move \mathcal{H}_S through to the right and find

$$\begin{aligned} \tilde{\mathcal{H}} &= \mathcal{H}_S + U'^{\dagger} \mathcal{H}_S + (\mathcal{H}_S U') + U'^{\dagger} \mathcal{H}_S U' + U^\dagger (\mathcal{H}'_R U) \\ &= \mathcal{H}_S + U'^{\dagger} \mathcal{H}_S + U' \mathcal{H}_S - \mathcal{X} + U'^{\dagger} (U' \mathcal{H}_S - \mathcal{X}) + U^\dagger \mathcal{H}'_R U \\ &= \mathcal{H}_S + (U'^{\dagger} + U' + U'^{\dagger} U') \mathcal{H}_S - \mathcal{X} - U'^{\dagger} \mathcal{X} + U^\dagger \mathcal{H}'_R U \\ &= \mathcal{H}_S - \mathcal{X} - U'^{\dagger} \mathcal{X} + U^\dagger \mathcal{H}'_R U, \end{aligned} \quad (7.22)$$

where the terms multiplied by \mathcal{H}_S cancel according to Eq. (7.18). The transformed Hamiltonian does not contain multiplications by \mathcal{H}_S anymore, but it does depend on \mathcal{X} , an auxiliary operator whose recurrent definition we do not know yet. To find it, we first focus on its anti-Hermitian part, \mathcal{Z} . Since recurrence relations are expressions whose right-hand side contains Cauchy products between series, we need to find a way to make

a product appear. We do so by using the unitarity condition $\mathcal{U}^\dagger + \mathcal{U}' = -\mathcal{U}'^\dagger \mathcal{U}'$ to obtain the recursive definition of \mathcal{Z} :

$$\begin{aligned}\mathcal{Z} &= \frac{1}{2}(\mathcal{X} - \mathcal{X}^\dagger) \\ &= \frac{1}{2}\left[(\mathcal{U}' + \mathcal{U}'^\dagger)\mathcal{H}_S - \mathcal{H}_S(\mathcal{U}' + \mathcal{U}'^\dagger)\right] \\ &= \frac{1}{2}\left[-\mathcal{U}'^\dagger(\mathcal{U}'\mathcal{H}_S - \mathcal{H}_S\mathcal{U}') + (\mathcal{U}'\mathcal{H}_S - \mathcal{H}_S\mathcal{U}')^\dagger\mathcal{U}'\right] \\ &= \frac{1}{2}(-\mathcal{U}'^\dagger\mathcal{X} + \mathcal{X}^\dagger\mathcal{U}').\end{aligned}\tag{7.23}$$

Similar to computing $W_{\mathbf{n}}$, computing $Z_{\mathbf{n}}$ requires lower-orders of \mathcal{X} and \mathcal{U}' . Then, we compute the Hermitian part of \mathcal{X} by requiring that $\tilde{\mathcal{H}}_R = 0$ in the Eq. (7.22) and find

$$\mathcal{Y}_R = (\mathcal{U}'^\dagger \mathcal{H}'_R \mathcal{U} - \mathcal{U}'^\dagger \mathcal{X} - \mathcal{Z})_R.\tag{7.24}$$

Once again, despite \mathcal{X} enters the right hand side, because all the terms lack 0th order, this defines a recursive relation \mathcal{Y} . To fix \mathcal{Y}_S , we use its definition (7.21), which gives

$$[\mathcal{V}, H_0] = \mathcal{Y} - [\mathcal{V}, \mathcal{H}'_S],\tag{7.25}$$

which is a continuous-time Lyapunov equation for \mathcal{V} . In order for this equation to be satisfiable, the selected part of the right hand side must vanish, since the left hand side has no selected part. Therefore we find:

$$\mathcal{Y}_S = [\mathcal{V}, \mathcal{H}'_S]_S,\tag{7.26}$$

and it vanishes if the selected part corresponds to a block-diagonal matrix.

The final part is straightforward. Finding \mathcal{V} from \mathcal{Y} amounts to solving a Sylvester's equation, Eq. (7.26), which we only need to solve once for every new order. This is the only step in the algorithm that requires a direct multiplication by \mathcal{H}'_S . In the eigenbasis of H_0 , the solution of Sylvester's equation is $V_{\mathbf{n},ij} = (\mathcal{Y}_R - [\mathcal{V}, \mathcal{H}'_S]_R)_{\mathbf{n},ij} / (E_i - E_j)$, where E_i are the eigenvalues of H_0 . However, even if the eigenbasis of H_0 is not available, there are efficient numerical algorithms to solve Sylvester's equation (see Sec. 7.4.2). An alternative is to decompose the Hamiltonian into its eigenoperator basis. This approach avoids specifying the eigenbasis of H_0 , and therefore it is better suited for second-quantized Hamiltonians [45, 46].

We now have the complete algorithm:

1. Define series \mathcal{U}' and \mathcal{X} and make use of their block structure and Hermiticity.
2. To define the hermitian part of \mathcal{U}' , use $\mathcal{W} = -\mathcal{U}'^\dagger \mathcal{U}' / 2$.
3. To find the antihermitian part of \mathcal{U}' , solve Sylvester's equation $[\mathcal{V}, H_0] = (\mathcal{Y} - [\mathcal{V}, \mathcal{H}'_S])_R$. This requires \mathcal{X} .
4. To find the antihermitian part of \mathcal{X} , define $\mathcal{Z} = (-\mathcal{U}'^\dagger \mathcal{X} + \mathcal{X}^\dagger \mathcal{U}') / 2$.
5. For the Hermitian part of \mathcal{X} , use $\mathcal{Y} = (-\mathcal{U}'^\dagger \mathcal{X} + \mathcal{U}'^\dagger \mathcal{H}' \mathcal{U})_R + [\mathcal{V}, \mathcal{H}'_S]_S$.
6. Compute the effective Hamiltonian as $\tilde{\mathcal{H}} \equiv \tilde{\mathcal{H}}_S = \mathcal{H}_S - \mathcal{X} - \mathcal{U}'^\dagger \mathcal{X} + \mathcal{U}'^\dagger \mathcal{H}'_R \mathcal{U}$.

7.3.4. EQUIVALENCE TO SCHRIEFFER–WOLFF TRANSFORMATION

Pymblock's algorithm applied to 2×2 block-diagonalization and the Schrieffer–Wolff transformation both find a unitary transformation \mathcal{U} such that $\tilde{\mathcal{H}}_R = \tilde{\mathcal{H}}^{AB} = 0$. They are therefore equivalent up to a gauge choice in each subspace, A and B . We establish the equivalence between the two by demonstrating that this gauge choice is the same for both algorithms. The Schrieffer–Wolff transformation uses $\mathcal{U} = \exp \mathcal{S}$, where $\mathcal{S} = -\mathcal{S}^\dagger$ and $\mathcal{S}^{AA} = \mathcal{S}^{BB} = 0$, this restriction makes the result unique [2]. On the other hand, our algorithm produces the unique block-diagonalizing transformation with a block structure $\mathcal{U}^{AA} = \mathcal{U}^{AA^\dagger}$, $\mathcal{U}^{BB} = \mathcal{U}^{BB^\dagger}$ and $\mathcal{U}^{AB} = -\mathcal{U}_{BA}^\dagger$. The uniqueness is a consequence of the construction of the algorithm, where calculating every order gives a unique solution satisfying these conditions. To see that the two solutions are identical, we expand $\exp \mathcal{S}$ into Taylor series. In the resulting series every term containing a product of an even number of terms of \mathcal{S} is a Hermitian, block-diagonal matrix, while every term containing a product of an odd number of terms of \mathcal{S} is an anti-Hermitian block off-diagonal matrix. Therefore $\exp \mathcal{S}$ has the same structure as \mathcal{U} above. Because both series are fixed by the hermiticity constraints on their block structure, we conclude that $\exp \mathcal{S}$ from conventional Schrieffer–Wolff transformation is identical to \mathcal{U} found by our algorithm.

7.3.5. EXTRA OPTIMIZATION: COMMON SUBEXPRESSION ELIMINATION

While the algorithm of Sec. 7.3.3 satisfies our requirements, we improve it further by reusing products that are needed in several places, such that the total number of matrix multiplications is reduced. Firstly, we rewrite the expressions for \mathcal{Z} in Eq. (7.23) and $\tilde{\mathcal{H}}$ in Eq. (7.22) by utilizing the Hermitian conjugate of $\mathcal{U}^\dagger \mathcal{X}$ without recomputing it:

$$\mathcal{Z} = \frac{1}{2} \left[(-\mathcal{U}^\dagger \mathcal{X}) - \text{h.c.} \right],$$

$$\tilde{\mathcal{H}} = \mathcal{H}_S + \mathcal{U}^\dagger \mathcal{H}'_R \mathcal{U} - (\mathcal{U}^\dagger \mathcal{X} + \text{h.c.})/2 - \mathcal{Y}_S,$$

where h.c. is the Hermitian conjugate, and \mathcal{Z} drops out from $\tilde{\mathcal{H}}$ because it is antihermitian. Additionally, we reuse the repeated $\mathcal{A} \equiv \mathcal{H}'_R \mathcal{U}'$ in

$$\mathcal{U}^\dagger \mathcal{H}'_R \mathcal{U} = \mathcal{H}'_R + \mathcal{A} + \mathcal{A}^\dagger + \mathcal{U}^\dagger \mathcal{A}. \quad (7.27)$$

Next, we observe that some products from the $\mathcal{U}^\dagger \mathcal{H}'_R \mathcal{U}$ term appear both in \mathcal{X} in Eq. (7.24) and in $\tilde{\mathcal{H}}$ (7.22). To avoid recomputing these products, we introduce $\mathcal{B} = \mathcal{X} - \mathcal{H}'_R - \mathcal{A}$ and define the recursive algorithm using \mathcal{B} instead of \mathcal{X} . With this definition, we compute the remaining part of \mathcal{B} as:

$$\begin{aligned} \mathcal{B}_R &= [\mathcal{Y} + \mathcal{Z} - \mathcal{H}'_R - \mathcal{A}]_R \\ &= [\mathcal{A}^\dagger + \mathcal{U}^\dagger \mathcal{A} - \mathcal{U}^\dagger \mathcal{X}]_R \\ &= [\mathcal{U}^\dagger \mathcal{H}'_R + \mathcal{U}^\dagger \mathcal{A} - \mathcal{U}^\dagger \mathcal{X}]_R \\ &= -(\mathcal{U}^\dagger \mathcal{B})_R, \end{aligned} \quad (7.28)$$

where we also used Eq. (7.24) and the definition of \mathcal{A} . The selected part of \mathcal{B} , on the other hand, is given by

$$\begin{aligned} \mathcal{B}_S &= [\mathcal{X} - \mathcal{H}'_R - \mathcal{A}]_S \\ &= \left[\frac{1}{2} [(-\mathcal{U}'^\dagger \mathcal{X}) - \text{h.c.}] + \mathcal{Y} - \mathcal{A} \right]_S \\ &= \left[\frac{1}{2} [(-\mathcal{U}'^\dagger [\mathcal{X} - \mathcal{H}'_R - \mathcal{A}]) - \text{h.c.}] + \mathcal{Y} - \frac{1}{2} [\mathcal{A}^\dagger + \mathcal{A}] + \frac{1}{2} [(-\mathcal{U}'^\dagger \mathcal{A}) - \text{h.c.}] \right]_S, \\ &= \left[\frac{1}{2} [(-\mathcal{U}'^\dagger \mathcal{B}) - \text{h.c.}] + [\mathcal{V} \mathcal{H}'_S + \text{h.c.}] - \frac{1}{2} [\mathcal{A}^\dagger + \text{h.c.}] \right]_S, \end{aligned} \quad (7.29)$$

where we used Eq. (7.23) and that $\mathcal{U}'^\dagger \mathcal{A}$ is Hermitian. Using \mathcal{B} changes the relation for \mathcal{V} in Eq. (7.26) to

$$[\mathcal{V}, H_0] = (\mathcal{B} - \mathcal{H}' - \mathcal{A} - [\mathcal{V}, \mathcal{H}'_S])_R. \quad (7.30)$$

Finally, we combine Eq. (7.22), Eq. (7.27), Eq. (7.29) and Eq. (7.28) to obtain the final expression for the effective Hamiltonian:

$$\tilde{\mathcal{H}}_S = \mathcal{H}_S + \frac{1}{2} \left[\mathcal{A} - \mathcal{U}'^\dagger \mathcal{B} + 2\mathcal{V} \mathcal{H}'_S + \text{h.c.} \right]_S. \quad (7.31)$$

Together with the series \mathcal{U}' in Eqs. ((7.19),(7.30)), $\mathcal{A} = \mathcal{H}'_R \mathcal{U}'$, and \mathcal{B} in Eqs. ((7.29),(7.28)), this equation defines the optimized algorithm.

7.4. IMPLEMENTATION

7.4.1. THE DATA STRUCTURE FOR BLOCK OPERATOR SERIES

The optimized algorithm from the previous section requires constructing 14 operator series, whose elements are computed using a collection of recurrence relations. This warrants defining a specialized data structure suitable for this task that represents a multidimensional series of operators. Because the recurrent relations are block-wise, the data structure needs to keep track of separate blocks. In order to support varied use cases, the actual representation of the operators needs to be flexible: the block may be dense arrays, sparse matrices, symbolic expressions, or more generally any object that defines addition and multiplication. Finally, the series needs to be queryable by order and block, so that it supports a block-wise multivariate Cauchy product—the main operation in the algorithm.

The most straightforward way to implement a perturbation theory calculation is to write a function that has the desired order as an argument, computes the series up to that order, and returns the result. This makes it hard to reuse already computed terms for a new computation, and becomes complicated to implement in the multidimensional case when different orders in different perturbations are needed. We find that a recursive approach addresses these issues: within this paradigm, each series needs to define how its entries depend on lower-order terms.

To address these requirements, we define a `BlockSeries` Python class and use it to represent the series of \mathcal{U} , \mathcal{H} , and $\tilde{\mathcal{H}}$, as well as the intermediate series used to define the algorithm. The objects of this class are equipped with a function to compute their

elements and it stores the already computed results in a dictionary. Storing the results for reuse is necessary to optimize the evaluation of higher order terms and it allows to request additional orders without restarting the computation. For example, the definition of the `BlockSeries` for \tilde{H} has the following form:

```
H_tilde = BlockSeries(
    shape=(2, 2), # 2x2 block matrix
    n_infinite=n, # number of perturbative parameters
    eval=compute_H_tilde, # function to compute the elements
    name="H_tilde",
    dimension_names=("lambda", ...), # parameter names
)
```

Here `compute_H_tilde` is a function implementing Eq. (7.31) by querying other series objects. Calling `H_tilde[0, 0, 2]`, the second order perturbation $\sim \lambda^2$ of the AA block, then does the following:

1. Evaluates `compute_H_tilde(0, 0, 2)` if it is not already computed.
2. Stores the evaluation result in a dictionary.
3. Returns the result.

To conveniently access multiple orders at once, we implement NumPy array indexing so that `H_tilde[0, 0, :3]` returns a NumPy masked array with the orders $\sim \lambda^0$, $\sim \lambda^1$, and $\sim \lambda^2$ of the AA block. The masking allows to support a common use case where some orders of a series are zero, so that they are omitted from the computations. We expect that the `BlockSeries` data structure is suitable to represent a broad class of perturbative calculations, and we plan to extend it to support more advanced features in the future.

We utilize `BlockSeries` to implement multiple other optimizations. For example, we exploit Hermiticity when computing the Cauchy product of $U'^{\dagger}U'$ in Eq. (7.19), by only evaluating half of the matrix products, and then complex conjugate the result to obtain the rest. Similarly, for Hermitian and anti-Hermitian series, like the off-diagonal blocks of U' , we only compute the AB blocks, and use the conjugate transpose to obtain the BA blocks. This approach should also allow us to implement efficient handling of symmetry-constrained Hamiltonians, where some blocks either vanish or are equal to other blocks due to a symmetry. Moreover, using `BlockSeries` with custom objects yields additional information about the algorithm and accommodates its further development. Specifically, we have used a custom object with a counter to measure the algorithm complexity (see also Sec. 7.5) and to determine which results are only used once so that they can be immediately discarded from storage.

7.4.2. THE IMPLICIT METHOD FOR LARGE SPARSE HAMILTONIANS

A distinguishing feature of Pymablock is its ability to handle large sparse Hamiltonians, that are too costly to diagonalize, as illustrated in Sec. 7.2.3. Specifically, we consider the

situations when the size N_E of the subspace of interest—explicit subspace—is small compared to the entire Hilbert space, so that obtaining the basis Ψ_E of the explicit subspace is feasible using sparse diagonalization. The projector on this subspace $P_E = \Psi_E^\dagger \Psi_E$ is then a low-rank matrix, a property that we exploit to avoid constructing the matrix representation of operators in the other, implicit, subspace.

The key tool to solve this problem is the projector approach introduced in Ref. [47], which introduces an equivalent extended Hamiltonian using the projector $P_I = 1 - P_A$ onto the implicit subspace:

$$\tilde{\mathcal{H}} = \begin{pmatrix} \Psi_E^\dagger \mathcal{H} \Psi_E & \Psi_E^\dagger \mathcal{H} P_I \\ P_I \mathcal{H} \Psi_E & P_I \mathcal{H} P_I \end{pmatrix}. \quad (7.32)$$

In other words, the explicit subspace is written in the basis of Ψ_E , while the basis of the implicit subspace is the same as the original complete basis of \mathcal{H} to preserve its sparsity. The extended Hamiltonian projects out the E -degrees of freedom from the implicit subspace to avoid duplicate solutions in $\tilde{\mathcal{H}}$, which introduces N_E eigenvectors with zero eigenvalues. Introducing $\tilde{\mathcal{H}}$ allows to multiply by operators of a form $P_I H_{\mathbf{n}} P_I$ efficiently by using the low-rank structure of P_E . In the code we represent the operators of the implicit subspace as `LinearOperator` objects from the SciPy package [41], enabled by the ability of the `BlockSeries` to store arbitrary objects. Storing the remaining blocks of $\tilde{\mathcal{H}}$ as dense matrices—efficient because these are small and dense—finishes the implementation of the Hamiltonian.

To solve the Sylvester's equation we write it for every row of $V_{\mathbf{n}}^{EI}$ separately:

$$V_{\mathbf{n},ij}^{EI} (E_i - H_0) = Y_{\mathbf{n},j}^{EI} \quad (7.33)$$

This equation has a solution despite $E_i - H_0$ not being invertible because $Y_{\mathbf{n}}^{EI} P_A = 0$. We solve this equation using the MUMPS sparse solver [48, 49], which prepares an efficient sparse LU-decomposition of $E_i - H_0$, or the KPM approximation of the Green's function [50]. Both methods work on sparse Hamiltonians with millions of degrees of freedom.

7.4.3. CODE GENERATION

An efficient computation of a perturbative block-diagonalization requires a significant amount of repeated optimizations. These include keeping track of the Hermiticity of involved series, applying the simplifications due to block-diagonalization and the presence of only two blocks, or deletion of series terms that are only used once. To separate the conceptual definition of the algorithm from these optimizations, we designed the code generation system that accepts a high-level description of the algorithm written in a domain-specific language and outputs the optimized Python code using the Python parser and the manipulation of the Python abstract syntax tree. For example, the definition of the series \mathcal{B} from Eqs. ((7.29),(7.28)) is written as:

```
with "B":
    start = 0
    if diagonal:
```

```

    ("U' @ B" - "U' @ B".adj + "H'_offdiag @ U'" + "H'_offdiag @
    - U'".adj) / -2
  if diagonal:
    zero if commuting_blocks[index[0]] else "V @ H'_diag" + "V @
    - H'_diag".adj
  if offdiagonal:
    -"U' @ B"

```

The corresponding compiled function for evaluating the terms of \mathcal{B} begins with

```

def series_eval(*index):
    which = linear_operator_series if use_linear_operator[index[:2]]
    - else series
    result = zero
    if index[0] == index[1]:
        result = _zero_sum(
            result,
            diag(
                _safe_divide(
                    _zero_sum(
                        which["U' @ B"][index], -Dagger(which["U' @
                        - B"][index]),
                        which["H'_offdiag @ U'"][index],
                        Dagger(which["H'_offdiag @ U'"][index]),
                    ), -2,
                ), index,
            ),
        )
    ...

```

7

Here we only show the beginning of the generated function to illustrate the correspondence between the high-level description and the generated code.

The code generation system has accommodated multiple rewrites of the algorithm during the development. We anticipate that it will enable treating different types of perturbative computations or other related algorithms, such as the derivative removal by adiabatic gate (DRAG) algorithm [51, 52]. Contrary to the perturbation theory setting, DRAG requires that the time-dependent Hamiltonian is block-diagonal in the rotating frame, and it achieves this goal by adding a series of corrections to the original Hamiltonian. Its overall setting, however, is similar to time-dependent perturbation theory in that it amounts to solving a system of recurrent algebraic equations. Our preliminary research already demonstrates that our code generation framework allows for a generalization of our work to the time-dependent perturbation theory, and we are confident that it applies to the DRAG algorithm as well.

7.5. BENCHMARK

To the best of our knowledge, there are no other packages implementing arbitrary order quasi-degenerate perturbation theory. Literature references provide explicit expressions

for the 2×2 effective Hamiltonian up to fourth order, together with the procedure for obtaining higher order expressions [5]. Because the full reference expressions are lengthy⁶, we do not provide them, but for example at 4-th order the effective Hamiltonian is a sum of several expressions of the form:

$$\sum_{m''m'''l} \frac{H'_{mm''} H'_{m''m'''} H'_{m'''l} H'_{lm'}}{(E_{m''} - E_l)(E_{m'''} - E_l)(E_m - E_l)}, \quad (7.34)$$

where the m -indices label states from the A -subspace and l -indices label the states from the B -subspace. More generally, at n -th order each term is a product of n matrix elements of the Hamiltonian and $n - 1$ energy denominators. Directly carrying out the summation over all the states requires $\mathcal{O}(N_A^2 N_B^{n-1})$ operations, where N_A and N_B are the number of states in the two subspaces. In other words, the direct computation scales worse than a matrix product with the problem size. Formulating Eq. (7.34) as $n - 1$ matrix products combined with $n - 1$ solutions of Sylvester's equation, brings this complexity down to $\mathcal{O}((n - 1) \times N_A N_B^2)$. This optimization, together with the hermiticity of the sum, allows us to evaluate the reference expressions for the effective Hamiltonian for 2-nd, 3-rd, and 4-th order using 1, 4, and 27 matrix products, respectively. Pymablock's algorithm yields the following expressions for the first four orders of the effective Hamiltonian:⁷

$$\begin{aligned} Y_{1,AB} &= H_{1,AB}, \\ \tilde{H}_{2,AA} &= H_{1,AB} V_1^\dagger / 2 + \text{h.c.}, \\ Y_{2,AB} &= V_1 H_{1,BB} - H_{1,AA}^\dagger V_1, \\ \tilde{H}_{3,AA} &= H_{1,AB} V_2^\dagger + \text{h.c.}, \\ Y_{3,AB} &= -\frac{V_1 V_1^\dagger H_{1,BA}^\dagger}{2} + V_2 H_{1,BB} - \frac{(H_{1,AB} V_1^\dagger + V_1 H_{1,AB}^\dagger) V_1}{2} - H_{1,AA}^\dagger V_2, \\ \tilde{H}_{4,AA} &= \frac{H_{1,AB} V_3^\dagger}{2} + \frac{V_1 V_1^\dagger (H_{1,AB} V_1^\dagger + V_1 H_{1,AB}^\dagger)}{8} + \text{h.c.}, \end{aligned} \quad (7.35)$$

where V_n are the solutions of Sylvester's equation with $Y_{n,AB}$ as the right-hand side. These expressions utilize 1, 3, and 11, matrix products to obtain the same orders of the effective Hamiltonian. The advantage of the Pymablock algorithm becomes even more pronounced at higher orders or with multiple perturbative parameters due to the exponential growth of the number of terms in the reference expressions. While finding the optimized implementation from the reference expressions is possible for the 3-rd order, we expect it to be extremely challenging for the 4-th order, and essentially impossible to do manually for higher orders. Moreover, because the `BlockSeries` class tracks absent terms, in practice the number of matrix products depends on the sparsity of the block structure of the perturbation, as shown in Fig. 7.5.

The efficiency of Pymablock becomes especially apparent when applied to sparse numerical problems, similar to Sec. 7.2.3. We demonstrate the performance of the im-

⁶The full expression takes almost a page of text.

⁷The output is generated by the algorithm, with manual modifications only done for formatting.

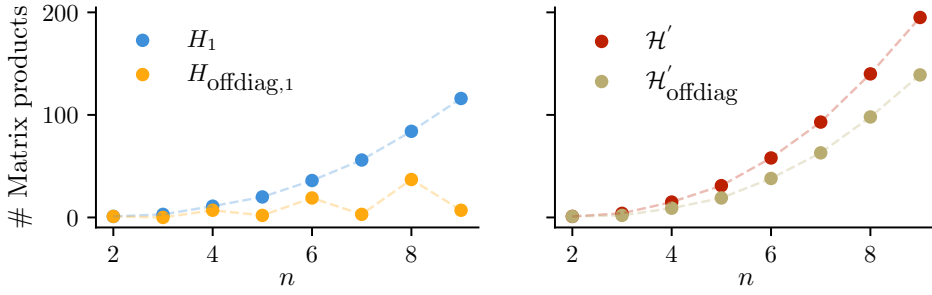


Figure 7.5: Matrix products required to compute \tilde{H}_n^{AA} for a dense and block off-diagonal first-order perturbation (left) and a dense and block off-diagonal perturbative series with terms of all orders present (right).

PLICIT method by using it to compute the low-energy spectrum of a large tight-binding model, and comparing Pymablock's time cost to that of sparse diagonalization. We define a 2D square lattice of 52×52 sites with nearest-neighbor hopping and a random on-site potential $\mu(\mathbf{r})$. The perturbation $\delta\mu(\mathbf{r})$ interpolates between two different disorder realizations. For the sake of an illustration, we choose the system's parameters such that the dispersion of the lowest few levels with $\delta\mu$ features avoided crossings and an overall nonlinear shape, whose details are not relevant. Similar to Sec. 7.2.3, constructing the effective Hamiltonian involves three steps. First, we compute the 10 lowest states of the unperturbed Hamiltonian using sparse diagonalization. Second, `block_diagonalize` computes a sparse LU decomposition of the Hamiltonian at each of the 10 eigenenergies. Third, we compute corrections \tilde{H}_1 , \tilde{H}_2 , and \tilde{H}_3 to the effective Hamiltonian, each being a 10×10 matrix. Each of these steps is a one-time cost, see Fig. 7.6. Finally, to compare the perturbative calculation to sparse diagonalization, we construct the effective Hamiltonian $\tilde{H} = H_0 + \delta\mu\tilde{H}_1 + \delta\mu^2\tilde{H}_2 + \delta\mu^3\tilde{H}_3$ and diagonalize it to obtain the low-energy spectrum for a range of $\delta\mu$. This has a negligible cost compared to constructing the series. The comparison is shown in Fig. 7.6. We observe that while the second order results are already very close to the exact spectrum, the third order corrections fully reproduce the sparse diagonalization. At the same time, the entire cost of computing the perturbative band structure for a range of $\delta\mu$ is lower than computing a single additional sparse diagonalization.

7.6. CONCLUSION

We developed an algorithm for constructing an effective Hamiltonian that combines advantages of different perturbative expansions. The main building block of our approach is a set of recurrence relations that define several series that depend on each other and combine into the effective Hamiltonian. Our algorithm constructs the same effective Hamiltonians as the Schrieffer–Wolff transformation [1] in the case of 2 subspaces, while keeping the linear scaling per extra order similar to the density matrix perturbation theory [16, 17] or the non-orthogonal perturbation theory [18]. Its expressions minimize the number of matrix multiplications per order, making it appealing both for symbolic and numerical computations. Pymablock's algorithm performs multi-block diagonalization

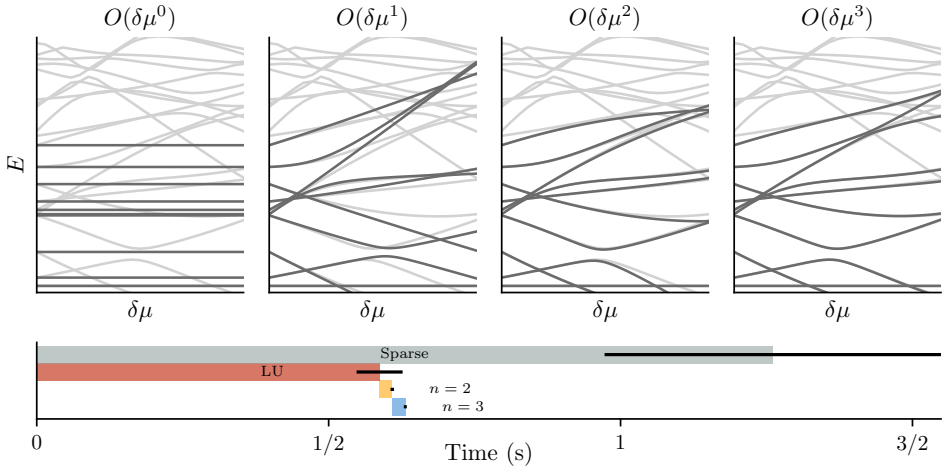


Figure 7.6: Top panels: band structure of the perturbative effective Hamiltonian (black) of a tight-binding model compared to exact sparse diagonalization (gray). Bottom panel: a comparison of the Pymablock's time cost with sparse diagonalization. Most of the time is spent in the LU decomposition of the Hamiltonian (red). The entire cost of the implicit method is lower than a single sparse diagonalization (gray). The operations of negligible cost are not shown. The bars length corresponds to the average time cost over 40 runs, and the error bars show the standard deviation.

and selective diagonalization with a single optimized algorithm.

We provide a Python implementation of the algorithm in the Pymablock package [53]. The package is thoroughly tested (95% test coverage as of version 2.1), becoming a reliable tool for constructing effective Hamiltonians that combine multiple perturbations to high orders. The core of the Pymablock interface is the `BlockSeries` class that handles arbitrary objects as long as they support algebraic operations. This enables Pymablock's construction of effective models for large tight-binding models using its implicit method as well as for second quantized Hamiltonians. As of version 2.1, applying Pymablock to second quantized Hamiltonians requires the user to provide a custom solver of the Lyapunov equation, which we plan to streamline in future versions. It also allows Pymablock to solve both symbolic and numerical problems in diverse physical settings, and potentially to incorporate it into existing packages, such as `scqubits` [35], `QuTiP` [54, 55], or `dft2kp` [56].

Beyond the Schrieffer–Wolff transformation, the Pymablock package provides a foundation for defining other perturbative expansions. We anticipate extending it to time-dependent problems, where the different regimes of the time-dependent drive modify the recurrence relations that need to be solved [57, 10]. Applying the same framework to problems with weak position dependence would allow to construct a nonlinear response theory of quantum materials. These two extensions are active areas of research [51, 52, 7, 58, 59, 46]. Finally, we expect that in the many-particle context the same framework supports implementing different flavors of diagrammatic expansions.

ACKNOWLEDGEMENTS

We thank Valla Fatemi and Antonio Manesco for feedback on the manuscript. We also thank David P. DiVincenzo for motivating and helpful discussions regarding the multi-block diagonalization algorithm.

DATA AVAILABILITY

The code used to produce the reported results is available on Zenodo [53].

Author contributions A. R. A. had the initial idea and oversaw the project. All authors developed the algorithm. I. A. D., S. M., H. K. K, and A. R. A. wrote the package. I. A. D. and A. R. A. wrote the paper.

Funding information This research was supported by the Netherlands Organization for Scientific Research (NWO/OCW) as part of the Frontiers of Nanoscience program, a NWO VIDI grant 016.Vidi.189.180, and OCENW.GROOT.2019.004. D.V. acknowledges funding from the Deutsche Forschungsgemeinschaft (DFG, German Research Foundation) under Germanys Excellence Strategy through the Würzburg-Dresden Cluster of Excellence on Complexity and Topology in Quantum Matter ct.qmat (EXC 2147, project-ids 390858490 and 392019).

REFERENCES

- [1] J. R. Schrieffer and P. A. Wolff. “Relation between the Anderson and Kondo Hamiltonians”. In: *Phys. Rev.* 149 (2 1966), pp. 491–492. [10.1103/PhysRev.149.491](https://doi.org/10.1103/PhysRev.149.491).
- [2] Sergey Bravyi, David P. DiVincenzo, and Daniel Loss. “SchriefferWolff transformation for quantum many-body systems”. In: *Annals of Physics* 326.10 (2011), pp. 2793–2826. [10.1016/j.aop.2011.06.004](https://doi.org/10.1016/j.aop.2011.06.004).
- [3] PerOlov Löwdin. “Studies in Perturbation Theory. IV. Solution of Eigenvalue Problem by Projection Operator Formalism”. In: *Journal of Mathematical Physics* 3.5 (Sept. 1962), pp. 969–982. [10.1063/1.1724312](https://doi.org/10.1063/1.1724312).
- [4] J. M. Luttinger and W. Kohn. “Motion of Electrons and Holes in Perturbed Periodic Fields”. In: *Phys. Rev.* 97 (4 1955), pp. 869–883. [10.1103/PhysRev.97.869](https://doi.org/10.1103/PhysRev.97.869).
- [5] Winkler Roland. “Spin-orbit coupling effects in two-dimensional electron and hole systems”. In: *Springer Tracts in Modern Physics: Springer, Berlin, Heidelberg* 191 (2003). [10.1007/b13586](https://doi.org/10.1007/b13586).
- [6] Edward McCann and Mikito Koshino. “The electronic properties of bilayer graphene”. In: *Reports on Progress in Physics* 76.5 (2013), p. 056503. [10.1088/0034-4885/76/5/056503](https://doi.org/10.1088/0034-4885/76/5/056503).
- [7] B. Andrei Bernevig et al. “Twisted bilayer graphene. I. Matrix elements, approximations, perturbation theory, and a $k \cdot p$ two-band model”. In: *Phys. Rev. B* 103 (20 2021), p. 205411. [10.1103/PhysRevB.103.205411](https://doi.org/10.1103/PhysRevB.103.205411).
- [8] Philip Krantz et al. “A quantum engineer’s guide to superconducting qubits”. In: *Applied physics reviews* 6.2 (2019). [10.1063/1.5089550](https://doi.org/10.1063/1.5089550).

- [9] Judit Romhányi, Guido Burkard, and András Pályi. “Subharmonic transitions and Bloch–Siegert shift in electrically driven spin resonance”. In: *Phys. Rev. B* 92 (5 2015), p. 054422. [10.1103/PhysRevB.92.054422](https://doi.org/10.1103/PhysRevB.92.054422).
- [10] Moein Malekakhlagh, Easwar Magesan, and David C. McKay. “First-principles analysis of cross-resonance gate operation”. In: *Physical Review A* 102.4 (2020). [10.1103/physreva.102.042605](https://doi.org/10.1103/physreva.102.042605).
- [11] Alexandru Petrescu et al. “Accurate Methods for the Analysis of Strong-Drive Effects in Parametric Gates”. In: *Physical Review Applied* 19.4 (2023). [10.1103/physrevapplied.19.044003](https://doi.org/10.1103/physrevapplied.19.044003).
- [12] J. H. Van Vleck. “On σ -Type Doubling and Electron Spin in the Spectra of Diatomic Molecules”. In: *Phys. Rev.* 33 (4 1929), pp. 467–506. [10.1103/PhysRev.33.467](https://doi.org/10.1103/PhysRev.33.467).
- [13] Isaiah Shavitt and Lynn T. Redmon. “Quasidegenerate perturbation theories. A canonical van Vleck formalism and its relationship to other approaches”. In: *The Journal of Chemical Physics* 73.11 (Dec. 1980), pp. 5711–5717. [10.1063/1.440050](https://doi.org/10.1063/1.440050).
- [14] D. J. Klein. “Degenerate perturbation theory”. In: *The Journal of Chemical Physics* 61.3 (Aug. 1974), pp. 786–798. [10.1063/1.1682018](https://doi.org/10.1063/1.1682018).
- [15] Kenji Suzuki and Ryoji Okamoto. “Degenerate Perturbation Theory in Quantum Mechanics”. In: *Progress of Theoretical Physics* 70.2 (Aug. 1983), pp. 439–451. [10.1143/PTP.70.439](https://doi.org/10.1143/PTP.70.439).
- [16] R. McWeeny. “Perturbation Theory for the Fock–Dirac Density Matrix”. In: *Phys. Rev.* 126 (3 1962), pp. 1028–1034. [10.1103/PhysRev.126.1028](https://doi.org/10.1103/PhysRev.126.1028).
- [17] Lionel A. Truflandier, Rivo M. Dianzinga, and David R. Bowler. “Notes on density matrix perturbation theory”. In: *The Journal of Chemical Physics* 153.16 (Oct. 2020), p. 164105. [10.1063/5.0022244](https://doi.org/10.1063/5.0022244).
- [18] Claude Bloch. “Sur la théorie des perturbations des états liés”. In: *Nuclear Physics* 6 (1958), pp. 329–347. [10.1016/0029-5582\(58\)90116-0](https://doi.org/10.1016/0029-5582(58)90116-0).
- [19] Franz Wegner. “Flow-equations for Hamiltonians”. In: *Annalen der physik* 506.2 (1994), pp. 77–91.
- [20] Stefan Kehrein. *The flow equation approach to many-particle systems*. Vol. 217. Springer, 2007.
- [21] Christian Knetter and Goetz S Uhrig. “Perturbation theory by flow equations: dimerized and frustrated S=1/2 chain”. In: *The European Physical Journal B-Condensed Matter and Complex Systems* 13 (2000), pp. 209–225. [10.1007/s100510050026](https://doi.org/10.1007/s100510050026).
- [22] Jaan Oitmaa, Chris Hamer, and Weihong Zheng. *Series expansion methods for strongly interacting lattice models*. Cambridge University Press, 2006.
- [23] H. Krull, N. A. Drescher, and G. S. Uhrig. “Enhanced perturbative continuous unitary transformations”. In: *Phys. Rev. B* 86 (12 2012), p. 125113. [10.1103/PhysRevB.86.125113](https://doi.org/10.1103/PhysRevB.86.125113).
- [24] Jonathan Wurtz, Pieter W. Claeys, and Anatoli Polkovnikov. “Variational Schrieffer–Wolff transformations for quantum many-body dynamics”. In: *Phys. Rev. B* 101 (1 2020), p. 014302. [10.1103/PhysRevB.101.014302](https://doi.org/10.1103/PhysRevB.101.014302).

- [25] Zongkang Zhang et al. “Quantum algorithms for Schrieffer–Wolff transformation”. In: *Phys. Rev. Res.* 4 (4 2022), p. 043023. [10.1103/PhysRevResearch.4.043023](https://doi.org/10.1103/PhysRevResearch.4.043023).
- [26] Ishan N. H. Mankodi and David P. DiVincenzo. “Perturbative power series for block diagonalisation of Hermitian matrices”. In: *Preprint* (2024). [10.48550/arXiv.2408.14637](https://arxiv.org/abs/2408.14637).
- [27] Easwar Magesan and Jay M. Gambetta. “Effective Hamiltonian models of the cross-resonance gate”. In: *Phys. Rev. A* 101 (5 2020), p. 052308. [10.1103/PhysRevA.101.052308](https://doi.org/10.1103/PhysRevA.101.052308).
- [28] Xuexin Xu et al. “Lattice Hamiltonians and stray interactions within quantum processors”. In: *Phys. Rev. Appl.* 22 (6 2024), p. 064030. [10.1103/PhysRevApplied.22.064030](https://doi.org/10.1103/PhysRevApplied.22.064030).
- [29] Christian Knetter, Kai P Schmidt, and Götz S Uhrig. “The structure of operators in effective particle-conserving models”. In: *Journal of Physics A: Mathematical and General* 36.29 (2003), p. 7889. [10.1088/0305-4470/36/29/302](https://doi.org/10.1088/0305-4470/36/29/302).
- [30] Alexandre Blais et al. “Cavity quantum electrodynamics for superconducting electrical circuits: An architecture for quantum computation”. In: *Phys. Rev. A* 69 (6 2004), p. 062320. [10.1103/PhysRevA.69.062320](https://doi.org/10.1103/PhysRevA.69.062320).
- [31] Guanyu Zhu et al. “Circuit QED with fluxonium qubits: Theory of the dispersive regime”. In: *Phys. Rev. B* 87 (2 2013), p. 024510. [10.1103/PhysRevB.87.024510](https://doi.org/10.1103/PhysRevB.87.024510).
- [32] X. Li et al. “Tunable Coupler for Realizing a Controlled-Phase Gate with Dynamically Decoupled Regime in a Superconducting Circuit”. In: *Phys. Rev. Appl.* 14 (2 2020), p. 024070. [10.1103/PhysRevApplied.14.024070](https://doi.org/10.1103/PhysRevApplied.14.024070).
- [33] Alexandre Blais et al. “Circuit quantum electrodynamics”. In: *Rev. Mod. Phys.* 93 (2 2021), p. 025005. [10.1103/RevModPhys.93.025005](https://doi.org/10.1103/RevModPhys.93.025005).
- [34] Eyob A. Sete et al. “Floating Tunable Coupler for Scalable Quantum Computing Architectures”. In: *Phys. Rev. Appl.* 15 (6 2021), p. 064063. [10.1103/PhysRevApplied.15.064063](https://doi.org/10.1103/PhysRevApplied.15.064063).
- [35] Peter Groszkowski and Jens Koch. “Scqubits: a Python package for superconducting qubits”. In: *Quantum* 5 (2021), p. 583. [10.22331/q-2021-11-17-583](https://arxiv.org/abs/2021.11.17-583).
- [36] Sai Pavan Chitta et al. “Computer-aided quantization and numerical analysis of superconducting circuits”. In: *New Journal of Physics* 24.10 (2022), p. 103020. [10.1088/1367-2630/ac94f2](https://doi.org/10.1088/1367-2630/ac94f2).
- [37] Boxi Li, Tommaso Calarco, and Felix Motzoi. “Nonperturbative Analytical Diagonalization of Hamiltonians with Application to Circuit QED”. In: *PRX Quantum* 3 (3 2022), p. 030313. [10.1103/PRXQuantum.3.030313](https://doi.org/10.1103/PRXQuantum.3.030313).
- [38] André Melo, Tanko Tanev, and Anton R. Akhmerov. “Greedy optimization of the geometry of Majorana Josephson junctions”. In: *SciPost Phys.* 14 (2023), p. 047. [10.21468/SciPostPhys.14.3.047](https://doi.org/10.21468/SciPostPhys.14.3.047).
- [39] Aaron Meurer et al. “SymPy: symbolic computing in Python”. In: *PeerJ Computer Science* 3 (2017), e103. [10.7717/peerj-cs.103](https://doi.org/10.7717/peerj-cs.103).

- [40] Christoph W Groth et al. “Kwant: a software package for quantum transport”. In: *New Journal of Physics* 16.6 (2014), p. 063065. [10.1088/1367-2630/16/6/063065](https://doi.org/10.1088/1367-2630/16/6/063065).
- [41] Pauli Virtanen et al. “SciPy 1.0: fundamental algorithms for scientific computing in Python”. In: *Nature methods* 17.3 (2020), pp. 261–272. [10.1038/s41592-019-0686-2](https://doi.org/10.1038/s41592-019-0686-2).
- [42] Samuel Savitz and Gil Refael. “Stable unitary integrators for the numerical implementation of continuous unitary transformations”. In: *Phys. Rev. B* 96 (11 2017), p. 115129. [10.1103/PhysRevB.96.115129](https://doi.org/10.1103/PhysRevB.96.115129).
- [43] R. McWeeny. “Self-consistent perturbation theory”. In: *Chemical Physics Letters* 1.12 (1968), pp. 567–568. [10.1016/0009-2614\(68\)85047-X](https://doi.org/10.1016/0009-2614(68)85047-X).
- [44] L S Cederbaum, J Schirmer, and H D Meyer. “Block diagonalisation of Hermitian matrices”. In: *J. Phys. A* 22.13 (1989), p. 2427. [10.1088/0305-4470/22/13/035](https://doi.org/10.1088/0305-4470/22/13/035).
- [45] Gabriel T. Landi. “Eigenoperator approach to Schrieffer–Wolff perturbation theory and dispersive interactions”. In: *Preprint* (2024). [10.48550/arXiv.2409.10656](https://doi.org/10.48550/arXiv.2409.10656).
- [46] Leander Reascos, Giovanni Francesco Diotallevi, and Mónica Benito. “Universal solution to the Schrieffer–Wolff Transformation Generator”. In: *Preprint* (2024). [10.48550/arXiv.2411.11535](https://doi.org/10.48550/arXiv.2411.11535).
- [47] Muhammad Irfan et al. “Hybrid kernel polynomial method”. In: *Preprint* (2019). [10.48550/arXiv.1909.09649](https://doi.org/10.48550/arXiv.1909.09649).
- [48] Patrick R. Amestoy et al. “A Fully Asynchronous Multifrontal Solver Using Distributed Dynamic Scheduling”. In: *SIAM Journal on Matrix Analysis and Applications* 23.1 (2001), pp. 15–41. [10.1137/S0895479899358194](https://doi.org/10.1137/S0895479899358194).
- [49] Patrick R. Amestoy et al. “Hybrid scheduling for the parallel solution of linear systems”. In: *Parallel Computing* 32.2 (2006). Parallel Matrix Algorithms and Applications (PMAA04), pp. 136–156. [10.1016/j.parco.2005.07.004](https://doi.org/10.1016/j.parco.2005.07.004).
- [50] Alexander Weiße et al. “The kernel polynomial method”. In: *Rev. Mod. Phys.* 78 (1 2006), pp. 275–306. [10.1103/RevModPhys.78.275](https://doi.org/10.1103/RevModPhys.78.275).
- [51] F. Motzoi et al. “Simple Pulses for Elimination of Leakage in Weakly Nonlinear Qubits”. In: *Phys. Rev. Lett.* 103 (11 2009), p. 110501. [10.1103/PhysRevLett.103.110501](https://doi.org/10.1103/PhysRevLett.103.110501).
- [52] L. S. Theis et al. “Counteracting systems of diabaticities using DRAG controls: The status after 10 years”. In: *Europhys. Lett.* 123.6 (2018), p. 60001. [10.1209/0295-5075/123/60001](https://doi.org/10.1209/0295-5075/123/60001).
- [53] Isidora Araya Day et al. *Pymablock*. Version 2.0. 2024. [10.5281/zenodo.14188554](https://doi.org/10.5281/zenodo.14188554).
- [54] J.R. Johansson, P.D. Nation, and Franco Nori. “QuTiP: An open-source Python framework for the dynamics of open quantum systems”. In: *Computer Physics Communications* 183.8 (2012), pp. 1760–1772. [10.1016/j.cpc.2012.02.021](https://doi.org/10.1016/j.cpc.2012.02.021).
- [55] J.R. Johansson, P.D. Nation, and Franco Nori. “QuTiP 2: A Python framework for the dynamics of open quantum systems”. In: *Computer Physics Communications* 184.4 (2013), pp. 1234–1240. [10.1016/j.cpc.2012.11.019](https://doi.org/10.1016/j.cpc.2012.11.019).

- [56] João Victor V. Cassiano et al. “DFT2kp: Effective kp models from ab-initio data”. In: *SciPost Phys. Codebases* (2024), p. 25. [10.21468/SciPostPhysCodeb.25](https://doi.org/10.21468/SciPostPhysCodeb.25).
- [57] M Rodriguez-Vega, Meghan Lentz, and Babak Seradjeh. “Floquet perturbation theory: formalism and application to low-frequency limit”. In: *New Journal of Physics* 20.9 (2018), p. 093022. [10.1088/1367-2630/aade37](https://doi.org/10.1088/1367-2630/aade37).
- [58] Jayameenakshi Venkatraman et al. “Static Effective Hamiltonian of a Rapidly Driven Nonlinear System”. In: *Phys. Rev. Lett.* 129 (10 2022), p. 100601. [10.1103/PhysRevLett.129.100601](https://doi.org/10.1103/PhysRevLett.129.100601).
- [59] Yingdan Xu and Lingzhen Guo. “Perturbative framework for engineering arbitrary Floquet Hamiltonian”. In: *Reports on Progress in Physics* 88.3 (2025), p. 037602. [10.1088/1361-6633/adb072](https://doi.org/10.1088/1361-6633/adb072).

8

CONCLUSION

In this thesis, we focused on the study of two types of topological phenomena: bulk phases protected by crystalline symmetries, and quantized transport in hybrid superconducting devices. The former is revealed by its response to magnetic flux, while the latter is enabled by it. We summarize our main findings and discuss further research directions below.

First, we developed a scattering theory that captures the topology of intrinsic higher-order topological insulators. Our main insight is that these phases exhibit a nontrivial spectral flow of their protected states as a function of flux, which resembles the spectral flow of edge states in the quantum Hall effect. An advantage of this theory over approaches that use reciprocal space is that it does not rely on translational symmetry, and therefore it may be applied to study delocalization transitions in disordered higher-order topological insulators. It is also the only existing approach that we know of that computes the topological invariant of crystalline topological phases using real space instead of momentum space. We identify two possible generalizations for future research: extensions to multi-terminal setups and interacting topological phases. Existing approaches to diagnose interacting crystalline topological phases so far focus on symmetry indicators [1, 2], and therefore it is interesting to consider whether spectral flow and adiabatic pumping extend beyond single-particle systems.

Second, we identified a mechanism for quantized transport that does not rely on bulk topology, but on the separation between counter-propagating modes in phase space—a space that combines position and momentum. This mechanism arises naturally in multi-terminal superconducting junctions whose terminals are separated by narrow normal regions. Specifically, we found that a superconducting tri-junction hosts Andreev bound states that propagate in a chiral fashion between the normal terminals, without any backscattering. The physics of this superconducting chiral waveguide is determined by the topology of the Fermi sea in the normal regions, and therefore the number of chiral modes per junction may be controlled by tuning the chemical potential. Observing this phenomenon experimentally is challenging, because it relies on extremely narrow

junctions and the absence of normal reflection.

Finally, we also developed Pymablock, a Python package to efficiently perform quasi-degenerate perturbation theory. The algorithm is consistent with the Schrieffer-Wolff transformation and Löwdin perturbation theory, but it applies to any number of perturbations, perturbative order, and quasi-degenerate subspaces. Recently, we also extended the package to support second-quantized operators and Floquet perturbation theory. Pymablock has so far been used to study microscopic superconductivity [3], Andreev supercurrents [4], nonlinearities of Josephson junctions [5], and semiconducting k,p models [6]. Because perturbation theory is a foundational tool in condensed matter and quantum physics, we expect this package to be useful for a variety of applications, from the design of robust superconducting qubits to the numerical study of strongly interacting systems.

REFERENCES

- [1] Martina O Soldini et al. “Interacting topological quantum chemistry of Mott atomic limits”. In: *Physical Review B* 107.24 (2023), p. 245145. [10.1103/PhysRevB.107.245145](https://doi.org/10.1103/PhysRevB.107.245145).
- [2] Martina O Soldini, Ömer M Aksoy, and Titus Neupert. “Interacting crystalline topological insulators in two-dimensions with time-reversal symmetry”. In: *Physical Review Research* 6.3 (2024), p. 033205. [10.1103/PhysRevB.107.245145](https://doi.org/10.1103/PhysRevB.107.245145).
- [3] Martina O. Soldini, Mark H. Fischer, and Titus Neupert. “Charge- $4e$ superconductivity in a Hubbard model”. In: *Phys. Rev. B* 109 (21 2024), p. 214509. [10.1103/PhysRevB.109.214509](https://doi.org/10.1103/PhysRevB.109.214509).
- [4] Alberto Bordin et al. “Impact of Andreev Bound States within the Leads of a Quantum Dot Josephson Junction”. In: *Phys. Rev. X* 15 (1 2025), p. 011046. [10.1103/PhysRevX.15.011046](https://doi.org/10.1103/PhysRevX.15.011046).
- [5] Valla Fatemi et al. “Nonlinearity of transparent SNS weak links decreases sharply with length”. In: *SciPost Phys.* 18 (2025), p. 091. [10.21468/SciPostPhys.18.3.091](https://doi.org/10.21468/SciPostPhys.18.3.091).
- [6] Sebastian Miles et al. “Effective Hamiltonians for Ge/Si core/shell nanowires from higher order perturbation theory”. In: *Preprint* (2025). [10.48550/arXiv.2511.11809](https://doi.org/10.48550/arXiv.2511.11809).

ACKNOWLEDGEMENTS

First, I thank Anton and Michael for leading such a fun and collaborative research environment. I admire how you carefully think about the ethical aspects of belonging to a scientific community, and how you are always open to feedback and suggestions. Anton, I am immensely grateful for your support and encouragement throughout my PhD; it was a pleasure to learn and work with you. There is a careful balance between having thoughtful and witty discussions, and I look forward to continuing to having them.

Collaborating with people during these past years has been a great source of joy for me; from joint coding to writing sessions, I considered it a privilege to learn directly from my colleagues. The discussions were often challenging, and I am thankful for the open and respectful way in which we worked together. I thank Daniel for welcoming me into the group during my first years in Delft; most of what I know about topology I learned from you. Kostas, I really enjoyed our daily interactions; it was inspiring to constantly see you pushing your coding skills, it motivated me to try as well. Johanna, thank you for your support and having so much patience with me. I appreciate how you make sure everyone gets a chance to celebrate their achievements. Antonio, you are a great friend and collaborator; I value your insights about mesoscopic physics and I wish to continue working together in the future. Adam, I am really happy we are collaborating, your perspective is often refreshing, I have a lot to learn from you. Valla, thank you for welcoming me in Ithaca and motivating me to learn about circuit QED, working with you was a scientifically enriching experience. I would also like to thank Juan, Sebastian, Hugo, Rik, Mert, Chunxiao for all the interesting and diverse discussions we had, I benefited a lot from them. I am extremely grateful for the opportunity to have studied and worked in such a stimulating environment, and I would like to thank QuTech and Nanofront for the fellowship programs that made all of this possible in the first place.

I spent most of my free time bouldering, a wonderful sport that I highly recommend to everyone. Maria, I am thankful for your friendship, I found your advice very helpful throughout my PhD. I also thank Tess and Marti for their friendship, which we built over encouraging ourselves to climb more and better. Lukas, we shared really fun adventures, but I am especially thankful that you pushed me to want to understand experimental setups better. Last year I was injured and could not climb; I thank Anna and Marilia for enthusiastically motivating me to go dancing and cheer me up while I was recovering.

Finally, I would like to thank my family and friends in Chile for always being there for me. I thank my dad for being so stubborn and home-schooling me; thanks to you I learned that curiosity is a fun pursuit and that with enough effort I can learn anything. Mom, thank you for supporting me in everything I have wanted to do and for constantly encouraging me to try new things.

CURRICULUM VITÆ

Isidora Melania ARAYA DAY

26-06-1996 Born in Santiago, Chile

EDUCATION

2015–2018 BSc. Physics
Universidad de Chile, Santiago, Chile

2019–2021 MSc. Applied Physics
Delft University of Technology, Delft, Netherlands

Thesis: Topological defects in a double-mirror quadrupole
insulator displace diverging charge

Supervisor: Anton R. Akhmerov

Cosupervisor: Dániel Varjas

2021–2026 PhD. Condensed Matter Physics
Delft University of Technology, Delft, Netherlands

Thesis: Revealing Topology with Flux: Manifestations of Broken Reciprocity

Promotor: Anton R. Akhmerov

Promotor: Michael T. Wimmer

LIST OF PUBLICATIONS

1. B. Pradenas, **I. Araya Day**, M. G. Clerc, C. Falcón, P. Gandhi, E. Knobloch, *Slanted snaking of localized Faraday waves*, [Phys. Rev. Fluids 2, 064401 \(2017\)](#)
2. **I. Araya Day**, A. R. Akhmerov, D. Varjas, *Topological defects in a double-mirror quadrupole insulator displace diverging charge*, [SciPost Phys. Core 5, 053 \(2022\)](#)
3. **I. Araya Day**, A Varentcova, D Varjas, A. R. Akhmerov, *Pfaffian invariant identifies magnetic obstructed atomic insulators*, [SciPost Physics 15 \(3\), 114 \(2023\)](#)
4. **I. Araya Day**, S. Miles, H. Kerstens, D. Varjas, A.R. Akhmerov, *Pymablock: An algorithm and a package for quasi-degenerate perturbation theory*, [SciPost Phys. Codebases 50 \(2025\)](#)
5. **I. Araya Day**, K. Vilkelis, A. L. R. Manesco, A. M. Bozkurt, V. Fatemi, A. R. Akhmerov, *Chiral adiabatic transmission protected by Fermi surface topology*, [SciPost Phys. 18, 098 \(2025\)](#)
6. **I. Araya Day**, A. L. R. Manesco, M. Wimmer, A. R. Akhmerov, *Identifying biases of the Majorana scattering invariant*, [SciPost Phys. Core 8, 047 \(2025\)](#)
7. R. J. Zijderveld, **I. Araya Day**, A. R. Akhmerov, *Scattering theory of higher order topological phases*, [SciPost Phys. 19, 058 \(2025\)](#)
8. H. Lu, **I. Araya Day**, A. R. Akhmerov, B. van Heck, V. Fatemi, *Kramers-protected hardware-efficient error correction with Andreev spin qubits*, [Phys. Rev. Lett. 135, 210602 \(2025\)](#)
9. R. J. Zijderveld, A. Y. Chaou, **I. Araya Day**, A. R. Akhmerov, *Symmetric approximant formalism for statistical topological matter*, [arXiv:2601.00784 \(2026\)](#)

